UCLouvain

École polytechnique de Louvain

Magnetic and thermomagnetic characterization of Co_2MnGa thin films

Author: **Savì Apicella**
Supervisors: **Pascal Gehring, Benoit Hackens**
Reader: **Bernard Nysten**
Academic year 2022–2023
Master [120] in Physical Engineering

Contents

List of Figures

List of Tables

Abstract

The study of materials with non-trivial topological phase boomed in the recent years, with many effects that are peculiar to these phases, and record-breaking magnitudes, which are intimately connected to the complex physics underlying. Examples can be found concerning the Anomalous Hall Effect, the Spin Hall Effect, or the emergence of superconductivity as well. However, one aspect has remained unexplored up to date, which is the charge-to-heat conversion, which could lead to remarkable applications for quantum computers or photon detectors, both having to operate at cryogenic temperatures.

Magnetic Weyl semimetals are one of the newest topological phases, discovered only in 2015 in TaAs, with the key signature being the chirality-resolved cones, composed of the valence and conduction bands dispersing linearly and touching at the Weyl point. At this peculiar point, the gap between the bands closes, and the Berry phase becomes singular. For this reason, it has been predicted theoretically that the charge-to-heat and heat-to-charge conversion effects should be significantly large. In Co_2MnGa, a full-Heusler compound, this has been repeatedly proven for the Nernst Effect, which entails a heat-to-charge conversion, but not at all for its counterpart, the Ettingshausen Effect, describing an electric current converted into a temperature gradient.

In this thesis work, I study indeed the presence of the Ettingshausen Effect in Co_2MnGa, trying to relate it with its magnetic structure, in the same way it has been done many times for the Nernst Effect. The samples I received came from Simon Granville's group in Welington, New Zealand, and were composed of 50 nm thin films of Co_2MnGa grown on a substrate of MgO. In particular, one set of film was uncapped, and another was coated with a Ta capping layer: they have been successively patterned into a Hall bar by collaborators at imec and characterized by Rikkie Joris and Lino da Costa Pereira at KU Leuven.

I firstly performed MFM on the samples, to gain insight on the domain structure. They have been magnetized at negative field, and then progressively saturated with positive magnetic field. A peculiar square domain structure has been observed for the uncapped Hall bar, whereas the maps obtained on the capped film and Hall bar were featureless. Successively, SThM was employed to study the Ettingshausen Effect, by injecting an electric current into the devices, applying an external magnetic field, and scanning the tip to observe the induced temperature difference. The signal was demodulated at the frequency of the current to separate the effect of interest from the Joule effect.

Line features in the thermal maps have been observed: their interpretation is not straightforward, even if calculations performed reveal that the effect should be large enough to be detected by the setup. The experimental work has been complemented with COMSOL simulation to help in the interpretation of the data, and estimate the magnitude of the effects of interest. The results presented in the work are promising, even if other experimental proofs are required to confirm to have observed the effect in Co_2MnGa.

Introduction

The following work aims at analysing the magnetic structure of Co_2MnGa (CMG) via Magnetic Force Microscopy (MFM) and investigating the Ettingshausen Effect employing Scanning Thermal Microscopy (SThM). To this end, 50 nm thick films of CMG have been provided by Simon Granville's group at Victoria University of Wellington: successively, Hall bars were patterned at imec to carry out the experiments. In order to be able to inject a current in the bars, then, they were mounted on PCBs (Printed Circuit Boards) and wire bonded. All the experiments have been performed with a Bruker Atomic Force Microscopy, equipped with a suitable probe and software to perform MFM or SThM. This experimental work was supported with simulations using COMSOL to gain deeper insight into the behaviour of the sample when probed thermally or magnetically.

This work is part of the project CONNECT (CaloritrOnics iN magNetiC Weyl semimeTals) funded from the FWO and F.R.S.-FNRS under the Excellence Of Science (EOS) program. This project aims indeed at investigating caloritronics, in particular Nernst and Ettingshausen Effect, in magnetic Weyl semimetals. The work has been carried on at Gehring Lab, a research lab within the department NAPS (NAnoscopic PhySics) at UCLouvain, one of the four partners of the project CONNECT. The patterning of the Hall bars has been done by collaborators at imec, and the structural characterization by collaborators at KU Leuven.

The thesis is structured as follows:

- **Chapter 1** will provide a theoretical review about the main features discussed in this thesis. The first point will be discussing the main properties of CMG, starting from the literature, and the topological features which make it so interesting. The next points will be short reviews about the magnetic domains behaviour during hysteresis and about the Ettingshausen Effect.
- **Chapter 2** will be focused on the experimental techniques employed in this work, namely MFM and SThM: the working principle and the setup employed during the experiments will be explained.
- **Chapter 3** will open the section devoted to the experimental results obtained with MFM and SThM, discussing the features observed.
- **Chapter 4** will be devoted to the simulations performed, either for the MFM and the SThM setup.

Finally, in the Appendix, a preliminary experiment conducted on a different sample., and with a different setup with respect to the previous ones, will be described, and the results analysed.

Chapter 1

Theoretical review

In this chapter the theoretical basis at the foundation of this work will be presented. In particular, the starting point will be a literature review of CMG, describing its atomic arrangement, the band structure, the magnetic and thermoelectric properties which have been extensively studied in the literature. In section 1.2 it will be possible to understand why CMG is so peculiar and important for these caloritronics experiments, introducing the concept of topology: this will be closely linked to its thermoelectric behaviour. Section 1.3 will serve as an introduction about magnetic domains and how they behave when sweeping through the hysteresis curve: this will allow to interpret correctly the MFM maps. Finally, in section 1.4 the Ettingshausen Effect will be presented.

1.1 CMG

1.1.1 Atomic arrangement

CMG is a full Heusler compound, meaning that the first two elements (Co and Mn) are transition metals, and the third one (Ga) belongs to the p-block, so its valence electrons are in the p orbital. It belongs to the $Fm\bar{3}m$ space group, and it displays three possible atomic arrangements, showed in Figure 1.1a. The $L2_1$ arrangement is fully ordered, with four interpenetrating fcc lattices, composed of A, B, C, and D sites, and a lattice constant of $a = 5.77$Å [23]. In this arrangement, these four sites correspond to Wickoff positions of (0, 0, 0), (1/4, 1/4, 1/4), (1/2, 1/2, 1/2) and (3/4, 3/4, 3/4), respectively: the A and C sites are occupied by Co, the B site by Mn and the D one by Ga [1]. This ordered arrangement can be transformed into the partially disordered B2 by raising the substrate temperature during deposition. The usual method of deposition is indeed magnetron sputtering on a substrate of MgO: when the temperature of the substrate is raised, the chemical disorder of the CMG films can be tuned (see Figure 1.1b). Indeed, the B2 structure is partially disordered, since the Mn and Ga atoms (therefore the B and D sites) cannot be recognized anymore, and the long-range ordering for these atoms disappears, transitioning toward an amorphous state. This can be clearly recognized in the X-Ray Diffraction (XRD) map, which, by diffraction of photons impinging on the surface, allows to reconstruct the main directions of crystalline orientation, namely the angles for which more diffracted photons are collected. For $T = 300$ C° and 550 C° the (002) and (004) peaks are presents, whereas they disappear for room temperature deposition, signaling the passage to a completely amorphous state, the A2 atomic arrangement. Also the peaks belonging to the MgO substrate are showed to be able to distinguish the feature characteristic of CMG. Further analyzing the (111) peak (not shown here) it was possible to determine that deposition at 550 C° yielded an $L2_1$

ordered arrangement, whereas deposition at 300 C° a B2 arrangement.

1.1.2 Band structure

Being CMG an Heusler alloy, it displays half-metallicity, meaning that the Density of States (DoS) is spin-dependent: in particular, for one spin orientation there will be a gap, therefore an insulating behaviour, the other one will show a metallic behaviour, with the Fermi energy cutting through the valence band. This can be confirmed checking the spin DoS and performing Spin ARPES (Angle Resolved PhotoEmission Spectroscopy) which allows to map the spin resolved band structure close to the Fermi energy for different directions in the Brillouine Zone (BZ). These are displayed in Figure 1.2: on the left the DoS has been calculated from first principles for CMG, along an interval of 8 eV across the Fermi energy. Looking at the inset, which is a zoom-in on the Fermi energy, only DoS positive values, correspondent to majority spin electrons, are present, indicating indeed a different transport behaviour between the two spin channels. In the right panel (Figure 1.2b) the calculated band structure along the cut Γ-K-X has been calculated and confronted with Spin-ARPES measurements. Looking at the K-X direction, it can be seen that, across the Fermi energy, only states with positive spin polarization (red lines in the left panel, and red areas in the right one) are present. Also the presence of a Weyl cone is highlighted: this will be further discussed in section 1.2.

However, CMG is also a semimetal, so the valence and conduction band overlap, creating a pocket of holes and electrons which both act as charge carriers, giving both their contributes to physical quantities like the electrical conductivity and the mobility. This can be verified calculating from first principles the band structure or performing ARPES, retrieving the experimental band structure close to the Fermi energy. In Figure 1.3 both of these approaches are showed: on the left the calculated band structure, showing very clearly that, at the Fermi energy, a pocket of holes is present at the Γ point, together with many conduction bands, relative to majority spin electrons. On the right, in Figure 1.3b, the experimental results from ARPES along the cut Γ-K with $E = 80\,eV$ photons are displayed. It is important to pay attention to the fact that the two images do not have the same scale, the left one ranging from 0.4 eV above E_F to 0.4 eV below, the second one going from E_F to 1 eV below the Fermi energy. However, one can anyway distinguish the pocket of hole in correspondence of the Γ point, flagged by the darker features in the map. ARPES is indeed based on collecting electrons at different angles thanks to the photoelectric effect, therefore the low darker regions correspond to the presence of holes.

1.1.3 Magnetic properties

Another fundamental feature of CMG resides in its ferromagnetism, with the Curie temperature being substantially above room temperature (694 C° [4]). The origin of ferromagnetism in Heusler alloy has been debated for long, and for alloys like CMG, in which the first element is magnetic, the mechanism responsible for it was thought to be the direct exchange coupling between Mn and Co rather than the Mn-Mn interaction between neighboring atoms [24]. However, recent studied on off-stochiometric CMG-like alloys [25] revealed that the exchange interaction between the first nearest neighbour Mn-Mn atom pair is stronger than the one of the first Co-Mn nearest neighbour atom pair, confirming that, also in these alloys, the interaction of the Mn atoms is the prominent mechanism to explain their ferromagnetism. Also, depending on whether the unoccupied Mn 3d states lie close to the Fermi level or above it, the dominant mechanism will be an antiferromagnetic superexchange or an RKKY-type ferromagnetic interaction [24].

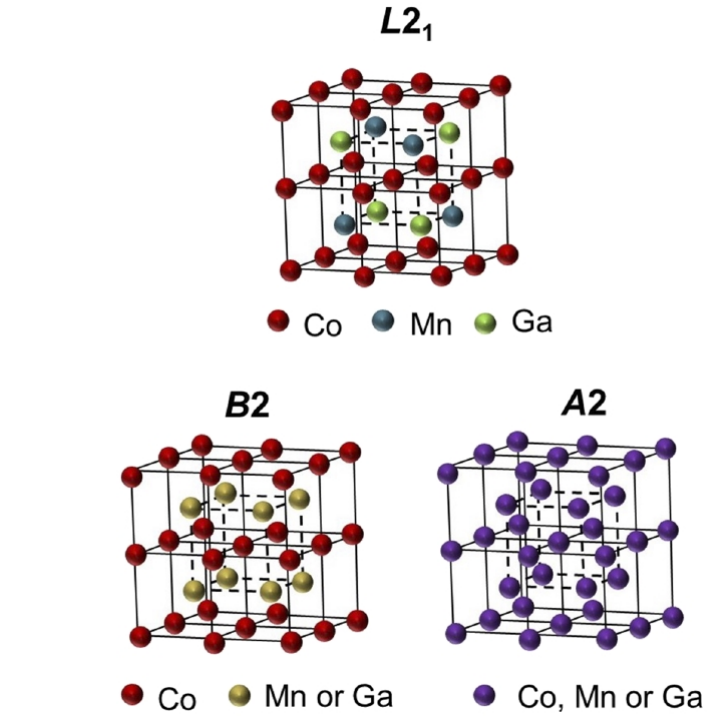

(a)

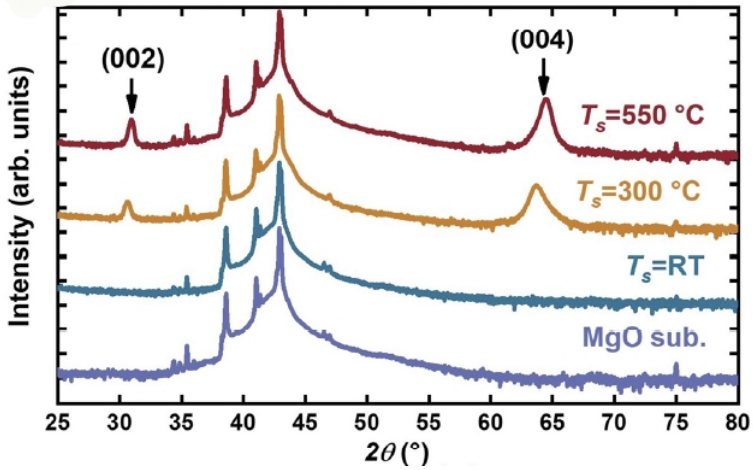

(b)

Figure 1.1: a): The three possible atomic arrangements of CMG. b): Out-of-plane XRD map for the MgO substrate and three films of CMG deposited with different substrate temperatures: (20 C°), 300 C° and 550 C° [1].

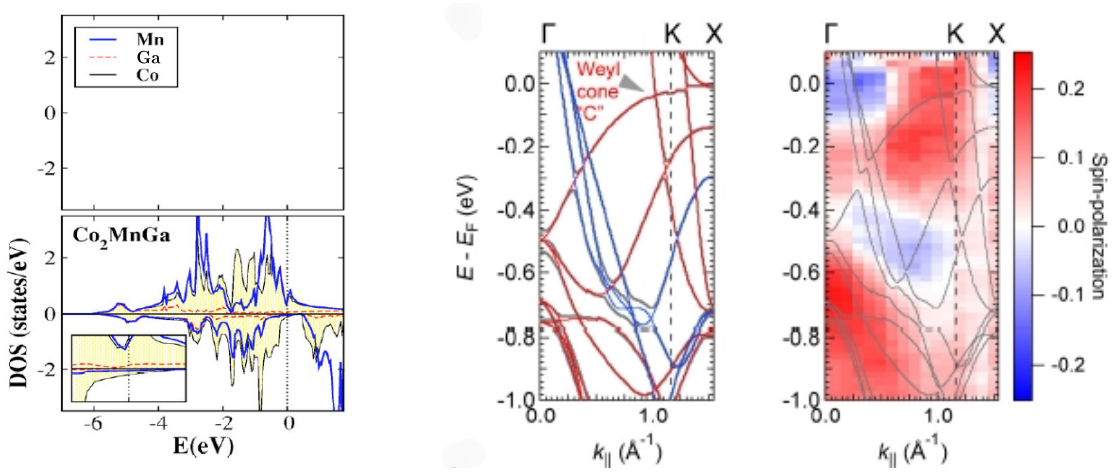

(a) (b)

Figure 1.2: a): Calculated DoS for CMG: in blue the Mn contribution, in dotted red the Ga one, and in black the Co one. Positive values refer to majority spin electrons and negative values to minority spin electrons. The inset is a zoom-in on the Fermi energy [2]. b): Left: Calculated spin resolved bandstructure, along the Γ-X cut: in red the majority spin electrons, in blue the minority spin ones. Right: Spin-ARPES on 50-nm thick CMG, along the same cut as the left panel. The calculated bandstructure is overlapped [3].

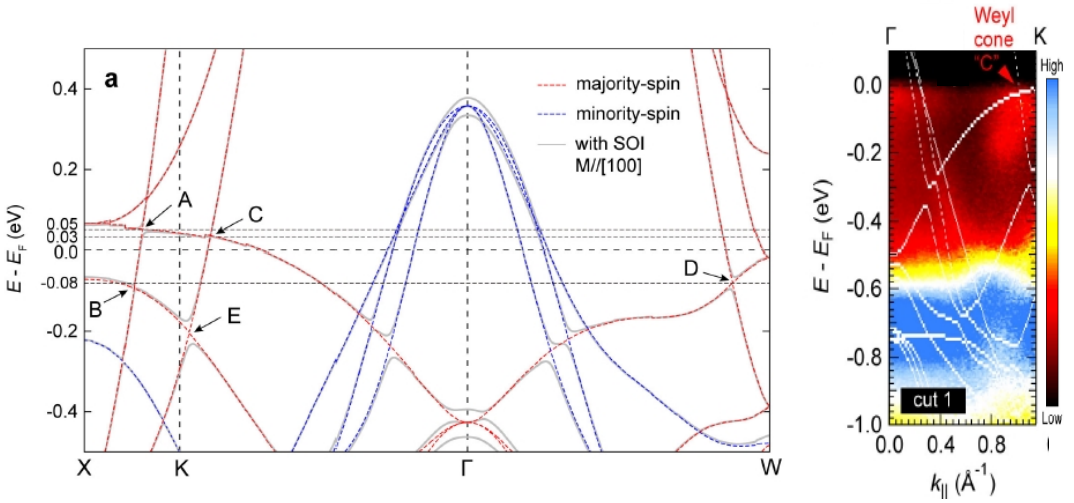

(a) (b)

Figure 1.3: a): Calculated spin-resolved bandstructure for CMG along the line X-K-Γ-W. In red the majority spin electrons, in blue the minority spin ones, in grey the corrections brought by the application of Spin-Orbit Interaction (SOI) and the magnetization along [100]. The Weyl cones are highlighted and labelled from A to E. b): ARPES performed on 50-nm thick CMG with 80 eV photons, along the cut Γ-K. In white the calculated bandstructure [3].

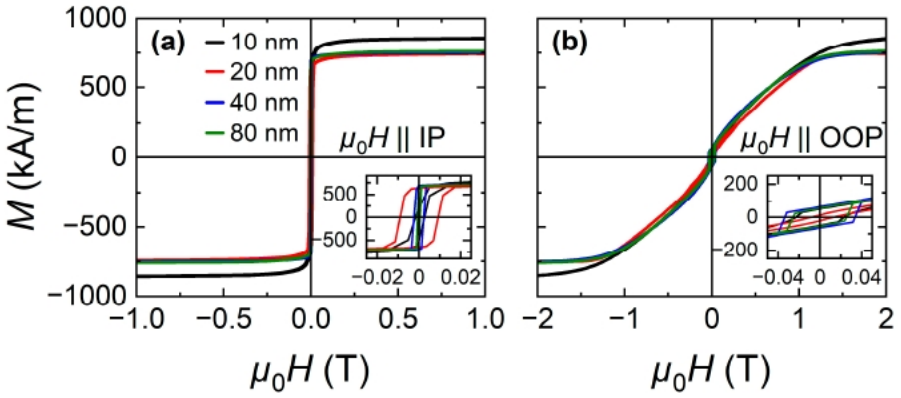

Figure 1.4: Hysteresis curves for CMG samples of different thicknesses (10, 20, 40 and 80 nm) for in-plane (IP) applied field (left) and out-of-plane (OOP) applied field (right). The insets show a zoom-in close to zero field [4].

One of the most important points for the setup of the experiments is the hysteresis curve of the material. In Figure 1.4 two curves are displayed, with the magnetic field being applied in-plane (IP) or out-of-plane (OOP): these correspond respectively to the [110] and equivalent directions, and to the (001) axis. It is evident that in both directions the material behaves as a soft ferromagnet, with high magnetization and low coercitivity. In particular, the IP orientation is the easy plane, with a field required to saturate the sample of circa 20 mT (inset on the left of Figure 1.4). The OOP direction constitutes instead the hard axis, with a saturation field of roughly 1 T. In both cases the coercive field is quite small, ranging from 20 to 40 mT depending on the thickness of the sample and on the field direction.

It is worth remarking that the magnetic properties can be tuned with the thickness of the sample. Indeed, the decreasing thickness brings about a strain-induced tetragonal distortion of the unit cell, which lowers the perpendicular lattice constant c and increase the in-plane lattice constant a, increasing the difference between the two and moving away from the cubic bulk value [4]. The misfit strain developing and the consequent distortion also affect the anisotropy of the films, as summarised in Table 1.1. The constant $K_{u,[001]}$ is the uniaxial anisotropy constant in the OOP direction: the relationship with the magnetic energy density is $E/V = K_{u,[001]} sin^2\theta$, with θ being the angle between the OOP direction and the field direction, along the plane perpendicular to the film. If $K_{u,[001]} < 0$, like in this case, the minimum of energy (correspondent to the easy plane) will be for $\theta = 90°$, so IP, confirming what was discussed above. The expression relating the cubic anisotropy constant K_c to the energy is similar, but involves not only one angle, but the projection of the magnetization along all the three axis. The concept and the origin of the magnetocrystalline anisotropy will be anyway reviewed in section 1.3. With decreasing thickness, therefore, the cubic anisotropy in plane increases and the uniaxial OOP decreases, rendering more and more energetically costly the OOP alignment of the magnetization, in agreement with the shape anisotropy contribution.

1.1.4 Thermomagnetic properties

The last important set of properties to discuss in CMG for the basis of this work are thermomagnetic properties. With respect to usual thermoelectric phenomena, namely

t [nm]	$\mathbf{K_{u,[001]}}$ [$\mathbf{J/m^3}$]	$\mathbf{K_c}$ [$\mathbf{J/m^3}$]
10	-95	7.0
20	-67	3.4
40	-75	3.7
80	-59	1.9

Table 1.1: OOP uniaxial anisotropy constant ($K_{u,[001]}$) and cubic anisotropy constant (K_c) for CMG samples with different thicknesses , determined from simulations [4].

the Seebeck and the Peltier effect, the thermomagnetic are similar in the setup, with the fundamental addition of the magnetic field. The thermomagnetic counterparts of the Seebeck and Peltier effects, are the Nernst Effect (NE) and the Ettingshausen Effect (EE). The output of the NE is a voltage $V_{NE,y}$, which is orthogonal to the applied difference of temperature ΔT_x and magnetic field B_z, according to the equation:

$$\mathbf{V_{NE,y}} = N_{NE}\mathbf{B_z} \times \mathbf{\Delta T_x}, \tag{1.1}$$

with N_{NE} $[V/TK]$ Nernst coefficient. The opposite of this effect is the EE, providing as output an heat current, therefore a temperature gradient $\nabla T_{EE,y}$ perpendicular to the applied magnetic field B_z and the injected current J_x, according to the equation:

$$\nabla \mathbf{T_{EE,y}} = P_{EE}\mathbf{J_x} \times \mathbf{B_z}, \tag{1.2}$$

where P_{EE} is the Ettingshausen coefficient, with unit of measure $[Km/TA]$. Now, if the materials in question are ferromagnets, the possibility of obtaining a transverse voltage for the NE or a heat current for the EE without applying an external field arises, employing the remnant magnetization of this type of material (see Figure 1.6a). This two phenomena are again NE or EE, but they are Anomalous, since an output can be obtained even without field, giving rise to the Anomalous Nernst Effect (ANE) and the Anomalous Ettingshausen Effect (AEE). Two examples of setups to investigate these effects are provided in Figure 1.5. The equations are similar to Equation 1.1 and 1.2, but in this case the key quantity is the magnetization of the system:

$$\mathbf{V_{ANE,y}} = N_{ANE}(\mu_0\mathbf{M_z} \times \mathbf{\Delta T_x}) = S_{ANE}\mathbf{\hat{m}_z} \times \mathbf{\Delta T_x}, \tag{1.3}$$

$$\nabla \mathbf{T_{AEE,y}} = P_{AEE}(\mathbf{J_x} \times \mu_0\mathbf{M_z}). \tag{1.4}$$

In this case a difference is to be made between the ANE thermopower S_{ANE}, which is usually the one reported in literature, whose unit of measures are $[V/K]$, like the Seebeck coefficient, and the anomalous Nernst coefficient in $[V/TK]$.

Whereas no literature is available about AEE in CMG, the ANE has been extensively studied in various configurations, reaching giant values ([5, 8, 7, 21, 26, 27]). In Figure 1.6a it is evident the action of the ANE: since, from Equation 1.3, the magnetization of the system is one of the key quantities for the generation of the transverse voltage, the trend of N_{ANE} follows exactly the hysteresis curve of the material, resulting in a non-zero signal even at zero field, thanks to the remnant magnetization. It has to be remarked that, in this image, the Nernst coefficient N_{ANE} is defined such that it has the same units of measures of the Nernst thermopower S_{ANE}, following a different convention. In Figure 1.6b the amplitude of the ANE in CMG is confronted with other materials, plotting it against the magnetization in the system. Not only the magnitude of the Anomalous Nernst thermopower (defined as above) is way larger in CMG than in the other conventional (trivial)

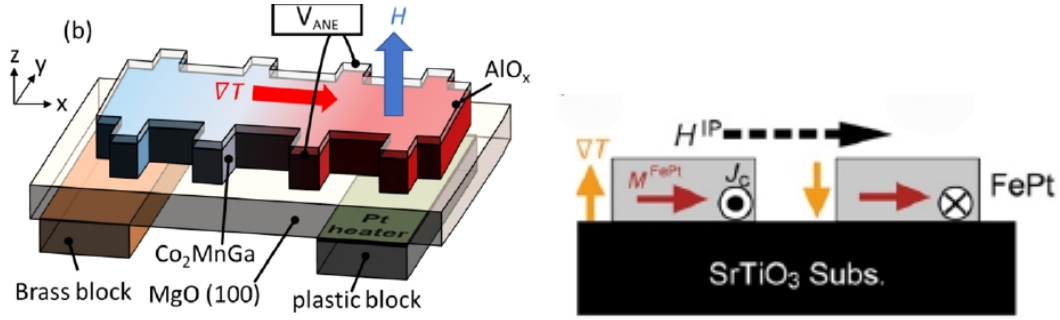

(a) (b)

Figure 1.5: Example of setups for a) ANE from [5] and b) AEE (cross-section view) from [6].

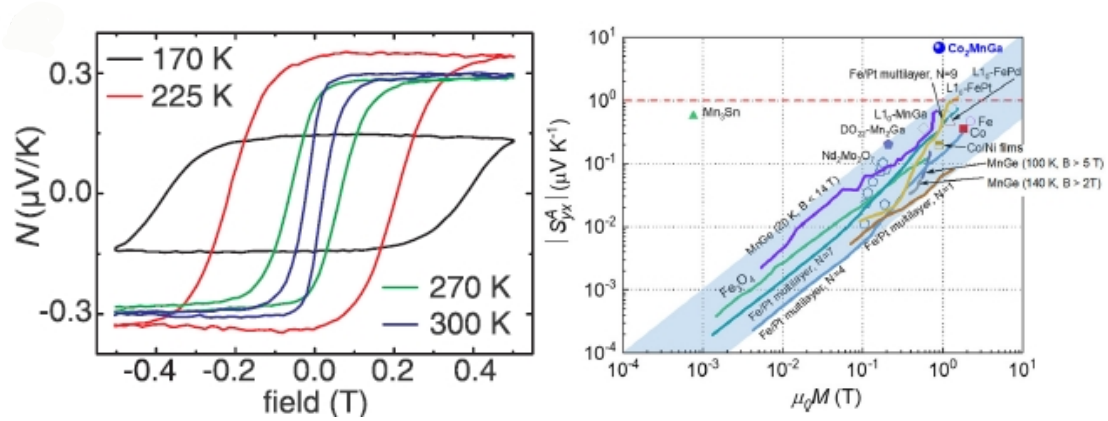

(a) (b)

Figure 1.6: a): Anomalous Nernst coefficient N_{ANE} (defined in $[V/K]$) in CMG against the applied field, at different temperatures [7]. b): Anomalous Nernst thermopower S_{ANE} (defined as in the text) against the magnetization of the system for different materials: the red dotted line is the largest thermopower value measured in conventional ferromagnets, the blue shaded area represents the linear relationship $S_{ANE} = N_{ANE}\mu_0 M$, with N_{ANE} ranging from 0.05 $\mu V/KT$ to 1 $\mu V/KT$ [8].

ferromagnets ($S_{ANE} = 7\mu V/K$ [8]), but it does not even follow the linear trend between the magnetization and the thermopower. Indeed, again from Equation 1.3, the relationship between S_{ANE} and N_{ANE} should be $S_{ANE} = N_{ANE}\,\mu_0 M$, which is the blue shaded area in Figure 1.6b. CMG escapes this trend, showing an ANE which is 7 times larger than predicted: the reason for this discrepancy resides in the topology of the material, which will be addressed in the next section.

As a final note, it should be remarked that CMG displays also Anomalous Hall Effect [26, 7, 8, 21], which, follows the same trend as the ANE, coinciding with the hysteresis curve: the origin of the two effects is indeed the same [21]. Recently, also the Spin Hall Effect (SHE) and the Inverse Spin Hall Effect (ISHE) have been investigated in CMG, resulting in a giant Spin Hall angle [28], which is the ratio between the charge current detected by the ISHE and the spin current generated by the SHE.

1.2 Magnetic Weyl Semimetals

Last section has been devoted to an overview about the physical and structural properties of CMG: it is now time to understand why some properties like the ANE are unexpectedly large, and to address the topology of the material. CMG is indeed classified as a magnetic Weyl semimetal (mWSM): the magnetism and the semimetallic features have already been dealt with, in this section the focus will be on the topology, investigating what Weyl semimetal means, and where this definition comes from.

1.2.1 Topology and Berry phase

The concept of topology stems from the intent of classifying all the materials depending on whether or not they were charge conductors: this is the usual classification in metals and insulators. The first set of material has no gap in between the valence and conduction bands, the latter ones do have it. It can be shown that, via a smooth deformation of the Hamiltonian, an insulating gap can be tuned to an arbitrarily small (but not zero) or large value, without closing it: therefore, all the insulators are connected by an equivalence relation, and they are all trivial insulators [10]. This theory was extremely simple and powerful, accommodating all the materials in just two classes: metals or insulators. However, topology came into play when the first example of an insulator fundamentally different from vacuum was discovered: the Integer Quantum Hall State (IQHS).

The IQHS manifests itself when electrons confined to two dimensions (a 2D electron gas, 2DEG) are placed in a strong magnetic field. In this case, the quantization of the usual cyclotron frequency ω_c leads to a different energy spectrum, made of quantized Landau Levels (LLs) $E_m = \hbar\omega_c(m + 1/2)$ (see Figure 1.7b). If the Fermi energy is in between two LLs, the system could resemble an insulator, with occupied and unoccupied states separated by a gap. However, in this case, the conductivity is finite and proportional to the number of occupied LLs N: $\sigma_{xy} = Ne^2/h$, and the quantization of this quantity has been measured with an accuracy of 1 part in 10^9, irrespective of the material.

The reason for this accuracy and robustness lies in the fact that the IQHS belongs to a different topological class with respect to the trivial insulator: one can indeed define a topological invariant $n \in \mathbb{Z}$, called Chern invariant (or Chern number) which takes on different values in these two states, $n = 1$ (or more) in the IQHS, and $n = 0$ in the trivial insulating state. This concept of topological invariant is similar to the concept of genus g in geometry. The genus could be roughly considered as the number of holes in a three-dimensional objects, and there is no way one could smoothly deform an object with $g = 0$ (a sphere, like in Figure 1.7a) into an object with genus $g = 1$ (a doughnut, like in Figure 1.7b). In the same way, n cannot change via smooth deformation of the Hamiltonian, and it is invariant, provided that the gap between occupied and empty bands remains finite (which is the same as requiring a smooth change in the Hamiltonian).

The Chern number anyway is intimately connected to the very Bloch wavefunctions: considering indeed a Bloch wavefunction in a 2D BZ $u(k_x, k_y)$, one could wonder what would be the form of this wavefunction after a closed loop C in the BZ, performed adiabatically, which is varying k_x from 0 to 2π. Berry [29] showed that, beside the usual term $exp(-i \int E(\mathbf{k}(t))dt)$, with E eigenstate of the Hamiltonian, there was an extra term:

$$u(k_x + 2\pi, k_y) = k_x, k_y \; exp(i\gamma k_x) \; exp\Big(-i \int E(\mathbf{k}(t))dt\Big), \tag{1.5}$$

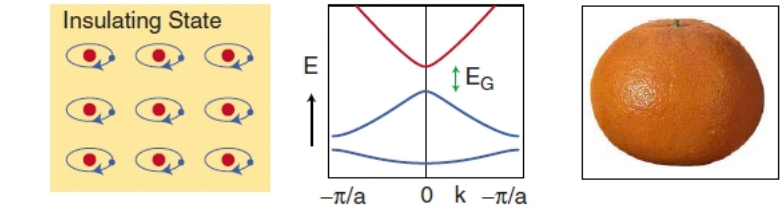

(a)

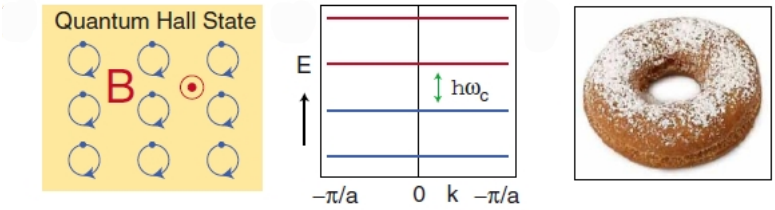

(b)

Figure 1.7: a): Left: sketch of the electron behaviour in a trivial insulating state. Center: energy spectrum in an insulating state. Right: example of an object with genus $g = 0$. b): Left: sketch of electron behaviour in a IQHS. Center: energy spectrum with LLs in a IQHS. Right: example of an object with genus $g = 1$ [9].

with γ Berry phase being:

$$\gamma(C) = \oint_C \mathbf{A}(\mathbf{k}) \cdot \mathbf{dk}. \tag{1.6}$$

$\mathbf{A}(\mathbf{k})$ is defined as the Berry connection, and it is directly linked to the Bloch wavefunctions, being defined as $\mathbf{A}(\mathbf{k}) = iu(\mathbf{k})\nabla_{\mathbf{k}}u(\mathbf{k})$. This Berry connection has the same property of the vector potential $\mathbf{A}(\mathbf{r})$ in electromagnetism: in particular, they both transform like $\mathbf{A}(\mathbf{k}) \longrightarrow \mathbf{A}(\mathbf{k}) + \nabla_{\mathbf{k}}\lambda$, with λ a phase, under gauge transformation. One could therefore think of taking the curl of the Berry connection, to obtain a quantity analogous to the magnetic field $\mathbf{B}(\mathbf{r}) = \nabla_{\mathbf{r}} \times \mathbf{A}(\mathbf{r})$. What is obtained is the Berry curvature $\mathbf{\Omega}(\mathbf{k})$:

$$\mathbf{\Omega}(\mathbf{k}) = \nabla_{\mathbf{k}} \times \mathbf{A}(\mathbf{k}). \tag{1.7}$$

Therefore, the Berry curvature is just like a magnetic field in the k-space. Integrating this over the whole BZ one gets the link with the Chern number:

$$n = \frac{1}{2\pi} \int_{BZ} \mathbf{\Omega}(\mathbf{k}) \cdot \mathbf{dS} \tag{1.8}$$

Coming back to the IQHS, it has been proven [30] that the number of occupied LLs N is exactly the difference between the Chern numbers across the interface between a trivial insulator and an IQHS: $N = \Delta n$, which goes under the name of "bulk-boundary correspondence". If there is just one occupied LL ($N = 1$), then, as discussed above, the Hamiltonian cannot change smoothly across the interface: this is the same as requiring that the gap must close. And this is exactly what happens (Figure 1.8): a one dimensional dispersion band develops in the bulk gap, giving rise to the chiral edge states which characterize the IQHE. The number of edge states is the number of occupied LLs, which is the Chern number in the system (since $n = 0$ for a trivial insulator).

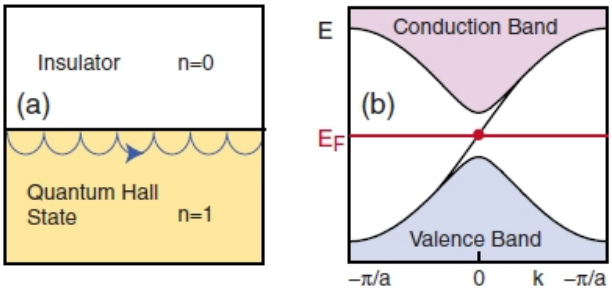

Figure 1.8: Left: Sketch of the interface between a trivial insulator and the IQHS, with the chiral edge states forming. Right: Band structure for a IQHS, with the edge state connecting valence and conduction bands [9].

1.2.2 Weyl points

To understand what a Weyl semimetal is, however, the discussion has to be pushed further into the world of topology, analysing other topological invariants and the role of time reversal symmetry $\mathcal{T}$. Indeed the next discovery of a non trivial topological state was the 2D Quantum Spin Hall state, in which $\mathcal{T}$ is preserved by the absence of an external magnetic field, and the edge states are spin separated, therefore they are at least two. In this case, $n_\uparrow = -n_\downarrow$, therefore the total Chern number is always zero, and a different topological invariant is needed, ν.

Looking at how the $\mathcal{T}$ symmetry acts on spin-$\frac{1}{2}$ particles, one obtains that, when this symmetry is present, all the eigenstates of a spin-$\frac{1}{2}$ system are twofold degenerate (Kramers' theorem). In a Bloch wavefunction this means that Kramers doublets are located at points k and $-k$. In a solid, however the SOI will lift the degeneracy, except in the points $k = 0$, and $k = \pi$, where any edge state residing in the bulk bandgap will be doubly degenerate. This gives rise to the situation depicted in Figure 1.9: either the Fermi level will cross the edge state an even number of times, and this means that, by shifting it, or smoothly deforming the Hamiltonian, one can push them out of the gap, and bring the crossing points to zero. The other possibility is that the crossing points are odd: in this case, whatever the tuning of the Fermi energy, there will be at least one crossing point. The former situation gives rise to trivial insulating state, and $\nu = 0$, the latter to topologically protected metallic boundary states, with $\nu = 1$. Since ν can only be 0 or 1, and satisfies the group operation of a $\mathbb{Z}_2$ group, it has been named $\mathbb{Z}_2$ topological invariant [9].

The 3D counterpart of the 2D Quantum Spin Hall state was soon predicted theoretically, and named 3D Topological Insulator (TI). They possess $\mathcal{T}$ symmetry and have topologically protected surface states which cross the Fermi energy. In this case four $\mathbb{Z}_2$ indices are used to describe them: the first one, ν_0 is the strong topological index and can be 0 or 1, ν_1, ν_2, ν_3 are the weak ones. The focus will be directly on the strong TIs for which $\nu_0 = 1$. In such a system, the dynamics of carriers on the surface is described by a Dirac-type effective Hamiltonian $H_s(k_x, k_y) = -\hbar v_F \hat{z} \times \boldsymbol{\sigma} \cdot \mathbf{k}$ [10], where v_F is the Fermi velocity, and σ the Pauli spinor. This means that the edge states disperse linearly in the bulk gap, with the spin always perpendicular to the momentum. There is still a bulk gap, though. If this gap is brought to zero, with the valence and conduction bands touching, the Hamiltonian of the system follows exactly the same form which describes Dirac massless fermions:

$$i\frac{d\psi}{dt} = \hat{H}\psi = \hbar v_F \begin{pmatrix} \boldsymbol{\sigma} \cdot \mathbf{k} & 0 \\ 0 & -\boldsymbol{\sigma} \cdot \mathbf{k} \end{pmatrix} \psi. \tag{1.9}$$

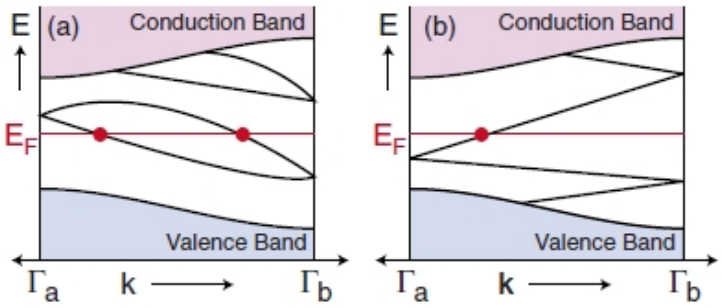

Figure 1.9: Even (left) and odd (right) number of crossing points between the gapless edge states and the Fermi energy. The points Γ_a and Γ_b represent $k = 0$ and $k = \pi$ in the text [9].

Within this Hamiltonian, the bands disperse linearly in all the three directions (k_x, k_y, k_z), unlike in strong TIs, forming a Dirac cone, with the bands touching each other at the Dirac point. In Figure 1.10 the passage from a trivial insulator to a topological one to a Dirac semimetal is represented: the bandgap closes for a Dirac semimetal and reopens for a TI, with the two states swapping their orbital character at the symmetry point. Up to now, the $\mathcal{T}$ symmetry has been retained: however, if a a Dirac semimetal is a ferromagnet, it will automatically break this symmetry, due to the generation of a magnetic field. This means that the four components Equation 1.9 can be decomposed in a two-components equation, which describes massless Weyl fermions:

$$i\frac{d\psi}{dt} = \hat{H}\psi = \pm\hbar v_F \boldsymbol{\sigma} \cdot \boldsymbol{k}. \tag{1.10}$$

The material whose bandstructure is described by this kind of Hamiltonian are Weyl semimetals (WSM). They can be obtained from Dirac semimetals breaking inversion symmetry or time reversal symmetry: if this is done by a mechanism of ferromagnetism, the material is a mWSM. Equation 1.10 introduces two kind of Dirac cones: a positive chirality one, in which $\boldsymbol{\sigma}//\boldsymbol{k}$, and a negative chirality one, in which they are antiparallel, as displayed in Figure 1.11a. The consequence of two distinct cones having different chirality is an open Fermi surface, with an arc (the Fermi arc) that connects the two Weyl points. This kind of feature can be revealed with ARPES and constitutes the hallmark of a WSM, as showed in Figure 1.11b. A further distinction can be introduced, depending on whether or not the cones are straight, defining respectively type I and II WSM (Figure 1.12). This implicates that in type II WSM there will always be an hole and electron pocket whatever the tuning of the Fermi energy. Moreover, these kind of WSMs are expected to show very different properties from type I [11].

1.2.3 Thermomagnetic coefficients

At the beginning of the section two goals were defined: understanding the definition of Weyl magnetic semimetal and why it gives rise to such large ANE. The first point has been addressed in the previous pages, now the latter one will be discussed.

It has been showed by Xiao in [31] that, even for transport driven by a statistical force, like a temperature or a chemical potential gradient, the expression of the transport current j involves a term proportional to the Berry curvature. In particular, if one starts from the local current J, obtained from the Boltzmann transport equation, the transport current is

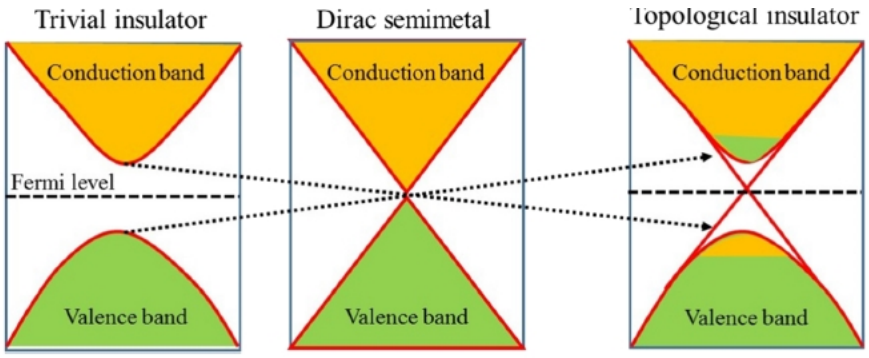

Figure 1.10: Sketch of a the bandstructure of a trivial insulator, a Dirac semimetal and a topological insulator [10].

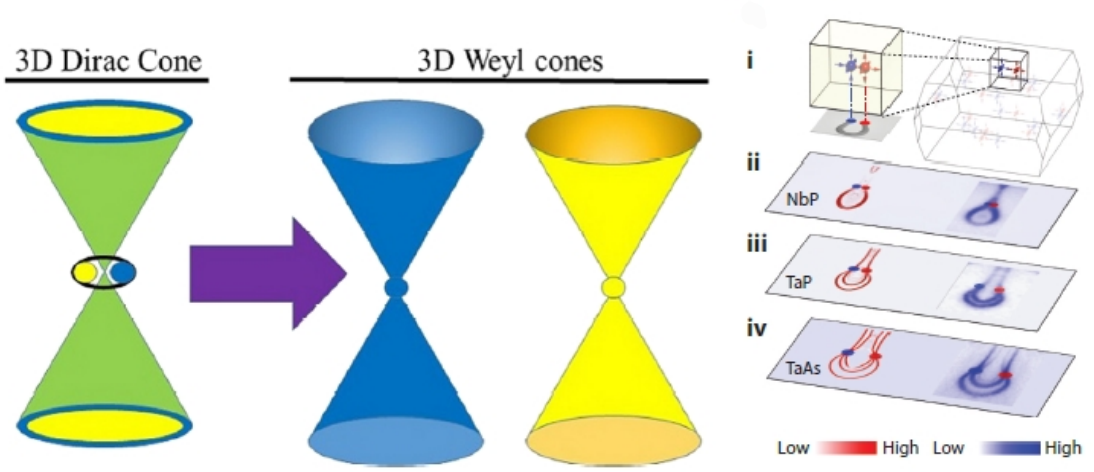

(a) (b)

Figure 1.11: a): Transformation from a 3D Dirac cone, exhibiting both chiralities, to two chiral 3D Weyl cones, upon breaking of $\mathcal{T}$ symmetry or inversion symmetry [10]. b): Experimental ARPES maps of the Fermi surface on the right confronted with ab initio calculations on the left. Panel i) is a sketch of the projection of the Weyl nodes on the surface, panels ii) - iii) - iv) refer to NbP, TaP, and TaAs, respectively [11].

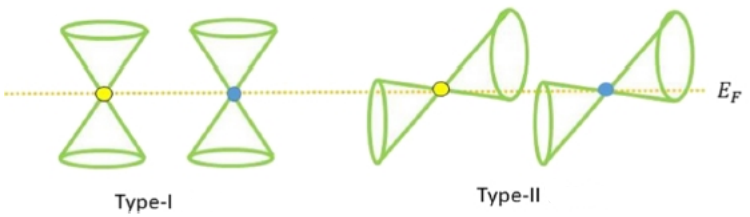

Figure 1.12: Distinction between type I WSM with straight cones and type II WSM with tilted cones generating pocket of holes and electrons [10].

defined as $\boldsymbol{j} = \boldsymbol{J} - \boldsymbol{\nabla} \times \boldsymbol{M(r)}$, with $\boldsymbol{M(r)}$ magnetization density. The Berry curvature link comes up in the magnetization, showing up in the transport current as well. Once this expression is laid out, it is possible to calculate the transverse current j_c arising when a temperature gradient $\boldsymbol{\nabla T}$ is applied (correspondent to the ANE), and the transverse heat current j_q arising when an electric field E is applied (AEE). These expressions are:

$$\boldsymbol{j_c} = -\frac{\boldsymbol{\nabla T}}{T} \times \frac{e}{\hbar} \int [d\boldsymbol{k}] \boldsymbol{\Omega} \big[(\epsilon - \mu) f + k_b T \, log(1 + e^{-\beta(\epsilon - \mu)} \big], \tag{1.11}$$

$$\boldsymbol{j_q} = \boldsymbol{E} \times \frac{e}{\hbar} \int [d\boldsymbol{k}] \boldsymbol{\Omega} \big[(\epsilon - \mu) f + k_b T \, log(1 + e^{-\beta(\epsilon - \mu)} \big], \tag{1.12}$$

where $\boldsymbol{\Omega}$ is the Berry curvature, f is the Fermi-Dirac distribution, ϵ the Fermi energy, μ the chemical potential and $\beta = \frac{1}{k_b T}$. It is therefore evident that both the Nernst and Ettingshausen coefficient are directly proportional to the Berry curvature. The last piece of the puzzle consists in understanding that the gap closings at the Weyl points are actually sources of Berry curvature. The Weyl point, indeed, behaves more precisely as a monopole for the Berry curvature, which, as stated above, behaves like a magnetic field in the k-space. It is as if the Weyl point represented a magnetic charge, which render the magnetic field (Berry curvature) undefined at that location. Being $\boldsymbol{\Omega}$ singular, the two thermomagnetic effects are expected to reach giant values, fueled by the Berry curvature singularity. This has been experimentally proved for the ANE, whereas it still lacks experimental confirmation for the AEE, which is the main point of the present work.

1.3 Magnetic domains

The purpose of this section is to give a general overview about magnetic domains, since they will be the object of the MFM study. In particular, the way domains, and domain walls, form and the energy balance that lies within it will be reviewed, together with the typical motion when following the hysteresis curve. The approach of the whole section is inspired from the domain theory, which operates at a mesoscopic scale ($1 - 1000\ \mu m$) and combines discrete, uniformly magnetized domains with the results of micromagnetism, which on the other hand analyzes the internal structure of domains walls at a smaller level.

The starting point of the discussion will be the classical theory of ferromagnetism, developed by Weiss in 1907, who hypothesised the existence of a molecular field H_m to explain the large spontaneous magnetization of ferromagnets even at low field. This molecular field was indeed supposed to be directly proportional to the magnetization M: however, by simple estimations based on the Curie temperature, the value of H_m results to be as high as $10^9 A/m$, which would suggest ferromagnets being permanently saturated under all conditions [14]. Therefore, the idea proposed by Weiss himself, was to divide the material in magnetic domains, which are regions in which the degree of alignment is dictated by the molecular field, but the orientation can vary from domain to domain. In this way, when averaging the magnetization over all the domains, the end result can turn out to be very different from the spontaneous magnetization, even close to zero.

1.3.1 Domain walls

Before delving into the mechanism that favour domain formation at all, it is instructive to understand the boundaries between domains, namely domain walls. In these regions, indeed, the magnetization rotates more or less smoothly from one orientation to the other depending on the dominant energetic terms. In general, forming a domain wall comes with

an energetic cost, and this will be relevant to explain domain formations. In this subsection, the two main energetic terms involved in the domain walls balance, the exchange interaction and the anisotropy energies, will be introduced, aiming at giving an estimation of the energy cost associated to the formation of a domain wall.

- ***Exchange interaction***. The exchange interaction is the one responsible for the long-range alignment of the magnetic moment in a ferromagnet. It has been quantitatively defined in the Heisenberg model, which is the quantum counterpart of the Weiss model for ferromagnetism, through the Heisenberg Hamiltonian [13]:

$$\hat{H}_H = -\sum_{ij} J_{ij} \boldsymbol{S_i} \cdot \boldsymbol{S_j}. \tag{1.13}$$

  This constitutes the summation over all atoms of the lattice of the scalar product between the i^{th} spin $\boldsymbol{S_i}$ and the j^{th} spin S_j multiplied by the exchange integral J_{ij} evaluated for atom i and j. The exchange integral can be written for two electrons in the states α and β, localized on two ions in positions r_1 and r_2, respectively, as:

$$J = \int \psi_a^*(\boldsymbol{r_1})\psi_b^*(\boldsymbol{r_2})\hat{H}\psi_a(\boldsymbol{r_2})\psi_b(\boldsymbol{r_1})d\boldsymbol{r_1}d\boldsymbol{r_2}, \tag{1.14}$$

  where $\hat{H}$ is the Hamiltonian describing the interaction between the two electrons and the two ions [12]. The origin of this interaction is therefore an electrostatic interaction that indeed tends to favour the spin alignment if $J > 0$, which is the case in Ni, Co and Fe, the magnetic elements.

- ***Magnetocrystalline anisotropy***. This type of anisotropy results from the spin orbit interaction between the electrons responsible of magnetism (for example, the 3d electrons in transition metals), which are affected by the lower symmetry of the crystal in which they reside [32]. The consequence of this interaction is the creation of easy axis, which require a lower field (and fewer energy) to magnetize the sample along that direction, and hard axis for which more energy is required, as already mentioned in section 1.1. Only the cases of uniaxial anisotropy and cubic anisotropy will be discussed since, as displayed in Table 1.1, they are the only cases of interest for CMG.

  - *Uniaxial anisotropy*: this is the case in which only one privileged direction controls the anisotropy energy. Taking for instance the z axis as reference, the expression of the energy density E/V will take the form:

$$E/V = K_1 sin^2\theta, \tag{1.15}$$

    where K_1 is the anisotropy constant, θ the angle between the magnetization and the reference axis, and the series is truncated at the first term sin^2. If K_1 is positive, this will give rise to easy axis anisotropy, the easy axis being the reference one, otherwise to an easy plane anisotropy, the plane being the one perpendicular to the axis, with a continuous degeneracy of equivalent orientations.
  - *Cubic anisotropy*: this corresponds to the case in which the anisotropy energy has cubic symmetry, with three privileged directions, for example the axis x, y, and z. Stopping the series at the first term, the energy density results to be:

$$E/V = K_1(m_x^2 m_y^2 + m_x^2 m_z^2 + m_y^2 m_z^2), \tag{1.16}$$

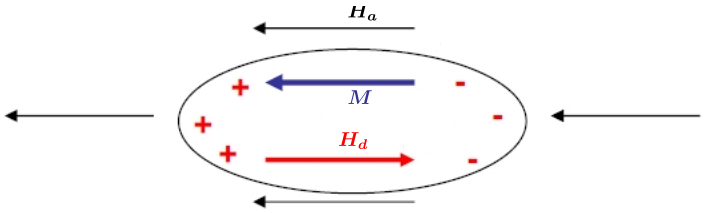

Figure 1.13: Sketch of the different fields in action when an external field $\boldsymbol{H_a}$ is applied to a magnetic material.

with m_i the projection of the magnetization along the i axis. If $K_1 > 0$, there will be six equivalent minima of energy correspondent to the $< 100 >$ axis, whereas the maxima are along the $< 111 >$ directions. If K_1 is negative, the minima and maxima swap.

- ***Shape anisotropy***. As the name suggests, the shape anisotropy is inherently connected to the shape of the sample. In particular, the shape of the sample affects the form of the demagnetizing tensor $\bar{N}$, which in turn, affects the demagnetizing field. Looking at Figure 1.13, indeed, when a sample is magnetized by an external field $\boldsymbol{H_a}$, a demagnetizing field $\boldsymbol{H_d}$ appears, and the internal field of the sample $\boldsymbol{H_i}$ takes the form:

$$\boldsymbol{H_i} = \boldsymbol{H_a} + \boldsymbol{H_d} = \boldsymbol{H_a} - \bar{N}\boldsymbol{M}, \tag{1.17}$$

  where $\boldsymbol{M}$ is the magnetization. For a thin film, which is the only case of interest in this work, the $\bar{N}$ tensor is diagonal, with $N_x = N_y = 0$, and $N_Z = 1$. This means that the demagnetizing field acts only if the sample is magnetized OOP, reducing the effective magnetization of the sample, and introducing an anisotropic term.

It is now easy to see why these different terms are in competition in the domain walls: the exchange interaction will favour thick walls, so that the orientation of the different magnetic moments during the rotation will be as aligned as possible. The magnetocrystalline anisotropy, on the other hand, will favour thin walls, to avoid the orientation of the moments along hard axis. The shape anisotropy in this estimation will be ignored since only in-plane rotations of the magnetization will be considered, so its contribution will be null. These opposite trends are clearly evident in the expression of the wall energy per unit area σ_{NW}, considering uniaxial anisotropy:

$$\sigma_{NW} = JS^2\frac{\pi^2}{Na^2} + \frac{NK_1a}{2}. \tag{1.18}$$

The only quantities which have not been already introduced are a, lattice parameter and N, which is the number of lattice sites encompassed by the thickness of the wall [12]. As stated above, the exchange contribution is minimized for $N \to \infty$, whereas the anisotropic one for $N \to 0$. An optimum can be found, which yields the expression $\sigma_{NW} = \pi S\sqrt{\frac{2JK_1}{a}}$, and is the energy cost per unit area associated with a domain wall.

1.3.2 Domains formation

There is however still one energetic term missing, which becomes relevant when one tries to understand why domains form at all. This is the magnetostatic energy, which is equal to:

$$E_m = \frac{\mu_0}{2}\int_V \boldsymbol{H_m}\cdot\boldsymbol{H_m}dV. \tag{1.19}$$

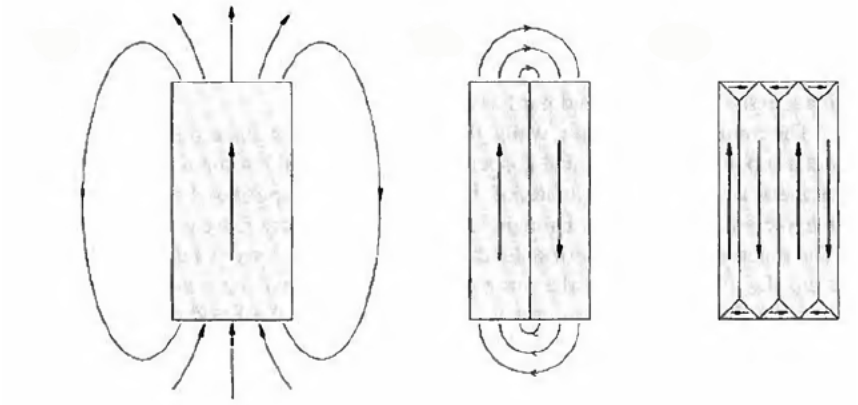

Figure 1.14: Single-domain sample (left), double-domains sample (center) and multi domain sample with closure domains (right), with the magnetostatic field going out of the sample, and the magnetization inside the domains [12].

The integral of the scalar product between the magnetostatic field and itself is taken over all the space. To minimize this integral, the field has to be minimized over all space. Observing Figure 1.14, it is easy to understand that one way to achieve this is by introducing domains, so regions of the sample with different magnetization: this strongly reduces the magnetostatic field which goes out of the sample. If closure domains are introduced, meaning domains at the edge of the sample with magnetization perpendicular to the one in the center, the field coming out of the sample can even be brought to zero. This corresponds to the principle of pole avoidance: since $\boldsymbol{\nabla} \cdot \boldsymbol{H_m} = -\boldsymbol{\nabla} \cdot \boldsymbol{M}$, having a non-zero divergence of the magnetization is like having magnetic poles in the sample, which generate field lines and increase the magnetostatic energy. However, as showed above, the formation of domains, which naturally reduces the magnetostatic energy, comes with an energetic cost associated to the generation of the walls, expressed by Equation 1.18. The formation of domains results therefore as a balance between the cost of generating domain walls, which already accounts for the exchange interaction and the anisotropy, and the minimization of the magnetostatic energy.

1.3.3 Domains movement

The last element to investigate is how the domains move when the external field is swept from negative saturation field to positive. A typical curve of first magnetization, which corresponds to the sample being magnetized for the first time, is displayed in Figure 1.15. Starting from zero field, the domains in this case are oriented along the easy axes of the material: as the field begins to increase (segment OA), the domain walls move reversibly in order to expand the domain whose magnetization is closer to the direction of the applied field. The movement is reversible up to the coercive field H_c: when the field gets larger than this value (segment AB), the walls movement are irreversible, and indeed the hysteresis curve is composed of tiny steps. This constitutes the Barkhausen Effect (inset of Figure 1.15), and each step corresponds to a single domain whose magnetization has been reversed. As the field is yet increased, the anisotropy becomes outweighed and the domains oriented favourably begin to rotate in the direction of the applied field, reversibly and simultaneously to the wall movement. At saturation only one domain is left, and its magnetization is parallel to the applied field. When the field is then reduced, the rotation region (segment CD) coincides with the other branch of the hysteresis curve (it is not the

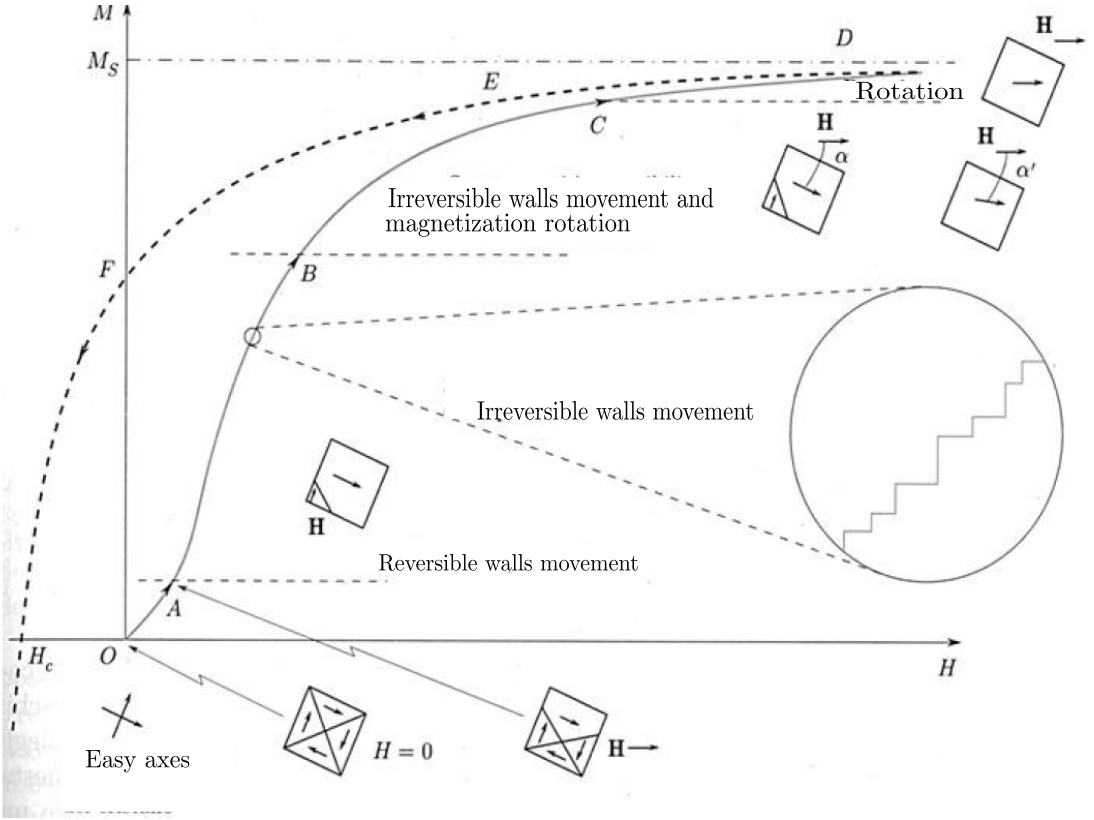

Figure 1.15: Curve of first magnetization and relative domain walls movement. In the inset the representation of the Barkhausen Effect. In dotted black the other branch of the hysteresis curve, produced when the field is lowered [13].

case in the picture, since the one showed is a first magnetization curve), since the rotation is reversible: when the walls begin to move irreversibly the two curves separate, giving rise to the hysteresis [12].

The peculiar characteristics of each material (dimensions, disorder, presence of impurities) determine how it will deviate from the ideal behaviour presented in Figure 1.15. The first aspect to be discussed are the possible magnetization reversal modes, which manifest themselves in the Barkhausen Effect. The principal reversal modes are two: coherent rotation and curling, sketched in Figure 1.16These are two possible solutions to linearized equations derived from micromagnetism, and the occurrence of one or the other can be expressed through energy considerations. If a sample coherently rotates, indeed, the exchange interaction is minimized, since all moments are aligned, but the magnetostatic energy increases, since a deviation Δm develops. On the other hand, curling minimizes the latter, but the exchange energy increases. It turns out that for small samples ($R_c/l_{ex} < 1$, with R_c characteristic dimension and $l_{ex} = \sqrt{\frac{2A}{\mu_0 M_s^2}}$ exchange length, with A exchange stiffness constant) it is convenient to rotate, whereas for larger samples, curling is favoured. For some particular cases, the reversal field which signals the onset of these phenomena coincide with the coercive field, which could be therefore affected by the dimensions and shape of the sample [14].

Another important coercitivity mechanism is domain wall pinning, which is strongly affected by the degree of disorder in the system. Indeed, in this case, the coercive field H_c varies from sample to sample simply because the domain walls are pinned by impurities

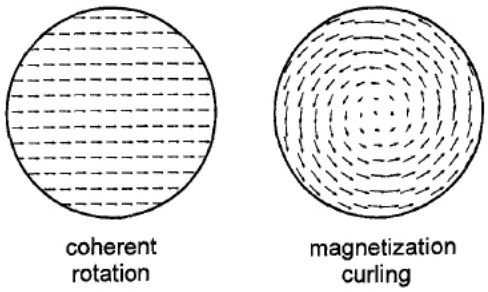

Figure 1.16: Sketch of the two possible modes of magnetization reversal [14].

such as grain boundaries, residual stresses, magnetic impurities, and cannot move. The stronger the pinning energy, which reflects the interaction between the wall and the single defects E_p, the larger the field needed to free the wall, and the larger the coercive field. In this case, different pinning regimes can be identified, depending on he behaviour of the wall when pinned and subject to an external magnetic field. The coercive field goes like $H_c \propto (\rho E_p)^\alpha$, with ρ defects volume density: α takes on the value 1/2, 2/3, or 1 if the wall stays rigid, bows in one dimension, or in two dimensions, respectively. The enhanced bowing, indeed, increases the magnetic charge density at the wall surface, increasing the magnetostatic energy, and the efficiency of the pinning. Within this picture, finally, the coercive field is defined as the critical field for which, after a series of random Barkhausen jumps, the average position of the wall significantly increases [14].

1.4 Ettingshausen Effect

This last section will be devoted to the Ettingshausen Effect (EE), which has been investigated in the present work, employing SThM. The first part will concern a review of the theory of the effect, starting from a general approach developed by Sommerfield [33] based on statistical theory for metals. In the second part, a short overview about the applications of the EE, in particular Ettingshausen cooling, will be provided, introducing the relevant parameters.

1.4.1 Theory of the effect

From a phenomenological standpoint, the temperature gradient developing upon the injection of a current along x and the application of a magnetic field along z can be understood as follows [15]. Let us imagine a distribution of quasi-continuous energy levels, each of which associated to a scattering time $\tau(\epsilon)$. This scattering time, when an electric field E_x is applied, determines the drift velocity as $v(\epsilon) = E_x e\tau(\epsilon)/m$. In the presence of a magnetic field, in the transient stage, a Hall field E_y will develop, exerting a force $F(\epsilon)$ on the carriers, which includes also the Lorentz term:

$$F(\epsilon) = eHv(\epsilon) + eE_y = \frac{e^2 H E_x \tau(\epsilon)}{m} + eE_y. \tag{1.20}$$

At the steady state, the Hall field E_y will be null, and for a certain energy $\bar{\epsilon}$, $F(\bar{\epsilon}) = 0$. However, as $\tau(\epsilon)$ decreases with energy, the most energetic electrons, which would be the fastest and hottest ones, will experience a force toward the negative y, the less energetic will deflect toward the other side (Figure 1.17). In this way a cold and a hot side develop.

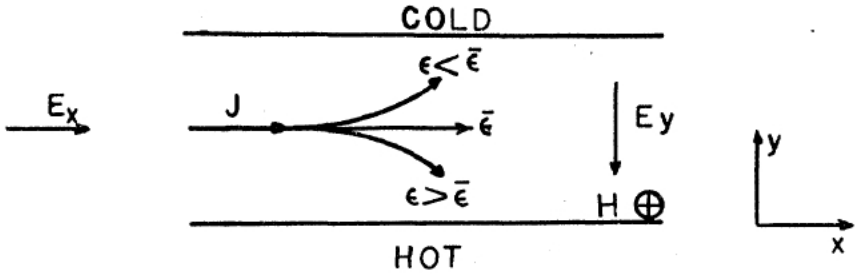

Figure 1.17: Sketch representing the EE. The carriers with energy $\epsilon > \bar{\epsilon}$ will be deflected toward negative y due to the Hall effect; the ones with lower energy in the opposite direction [15].

Moving on to a more quantitative discussion, the starting point of the reasoning developed by Sommerfield in [33] is a metallic plate lying in the xy direction, with a homogeneous magnetic field H perpendicular to the film plane, and current I_x flowing in the x direction, and the electrons considered as free. The presence of the Lorentz force will modify the distribution function f_0, adding an x and y component represented by two functions $\chi_1(\boldsymbol{v})$ and $\chi_2(\boldsymbol{v})$ proportional to the electrons velocity v, in the following way:

$$f = f_0 + v_y\chi_1(v) + v_x\chi_2(v), \tag{1.21}$$

with f_0 Fermi-Dirac (FD) distribution. The Boltzmann transport equation in these conditions takes the form:

$$\Big(\frac{e}{m}E_x + \frac{e}{m}Hv_x\Big)\frac{\partial f}{\partial v_y} + v_y\frac{\partial f}{\partial x} + \Big(\frac{e}{m}E_y - \frac{e}{m}Hv_y\Big) + \\ + v_x\frac{\partial f}{\partial y} = -\frac{v}{l}\Big(v_y\chi_1 + v_x\chi_2\Big), \tag{1.22}$$

with e and m electron charge and mass, l electron mean free path, and E electric field. The quantity of interest in this case is the heat flow along y, W_y, which is given from:

$$W_y = \frac{m}{2}\Big(\frac{m^3}{h}\Big)\int v_x v^2 f dv_x dv_y dv_z \tag{1.23}$$

In order to proceed and simplify the calculations, some boundary conditions have to be set: since the objective is to develop a temperature gradient along y, the heat flow has to be set to zero: $W_y = 0$. About the x direction, there will certainly be a heat flow along with the current, but, supposing a large thermal conductivity in metals, one can consider fast thermalization and $\partial T/\partial x = 0$. The electric current along y will also be set to zero, whereas there is one flowing along x: $I_x \neq 0$, $I_y = 0$. With these boundary conditions, and defining the Ettingshausen coefficient P_{EE} as in Equation 1.2, one gets:

$$P_{EE} = \frac{e^2}{m^2\sigma}\frac{K_1K_6 - K_2K_5}{K_2K_8' - K_6K_4'} = \frac{e^2}{m^2\sigma}\frac{lT}{\bar{v}^3}. \tag{1.24}$$

In this equation the K_i quantities are different integrals involving the velocity v, the FD distribution f_0, electron mean free path l and mobility μ, K_i' are their derivatives. Furthermore, σ is the electrical conductivity, T is the temperature and $\bar{v}$ is the velocity of the whole gas of electrons: indeed, one of the main assumption is that all the electrons have

the same velocity. This semiclassical approach therefore yields a coefficient which does not depend on the magnetic field, but is intrinsically positive, a consequence of having assumed only electrons as charge carriers, Other strong approximations regard the behaviour of the electron mean free path l, taken as independent of the velocity, and the very same assumption of free electrons.

A similar development has been carried out for semiconductors [15]. Starting again from the Boltzmann equation Equation 1.22, with the distribution function modified according to Equation 1.21, and the same boundary conditions, one considers both electrons and holes as charge carriers, assuming a small bandgap between valence and conduction band. Expressing the electron mean free path in terms of the scattering times τ_n and τ_p also the electron and hole densities n and p, and their mobilities μ_n and μ_p enter the calculations. In the end, it is possible to express the P_{EE} coefficient as a function of the energy bandgap E_g, the mobilities and densities of electrons and holes. Even though in CMG both charge carriers are indeed present, the energy gap at the Weyl points is rigorously null, since the two bands touch themselves. Neither of the two approaches are therefore suitable to describe theoretically the phenomenon in semimetals.

1.4.2 Ettingshausen cooling

The main application of the EE, just as for the Peltier effect, its thermoelectric counterpart, is cooling devices. In particular, the EE could be relevant in creating cryogenic coolers, operating at low temperatures [16]. Just as for thermoelectric phenomena, also for EE cooling a figure of merit can be defined, which takes the following form [34]:

$$Z_{EE}T = \frac{P_{EE}^2 \sigma_{xx}}{\kappa} \frac{1}{T}, \tag{1.25}$$

where σ_{xx} is the longitudinal electrical conductivity, and k the thermal conductivity. Beside the obvious requirement of having a large Ettingshausen coefficient, also a good electrical conduction and a poor thermal conduction would be beneficial: in this way, indeed, less voltage would be required to have a large current, and less power to have a large temperature difference, respectively. Materials with a large number of of electron-hole pairs available are to be preferred: if both carriers are available, indeed, the mechanism depicted in Figure 1.17 would benefit from the double contribution of electron and holes.

With respect to conventional thermoelectric coolers, some advantages in exploiting the EE can be identified [16].

- ***Single material devices***. The thermoelectric coolers are designed as two pillars of different materials, which are n and p-doped. An EE cooler could be realized employing just one material, making a possible optimization easier.

- ***Cooling power***. The feature of employing a transverse temperature gradient with respect to the direction of current injection opens up the possibility to optimize the device realizing two different cross-sections: a small one in the direction of the electric current, to increase easily the current density, and a large one in the temperature gradient direction, to maximise the difference of temperature between the two sides. This possibility is not available in thermoelectric coolers, where the heat and electric current flow in the same direction.

- ***Infinite-stage cascade***. By shaping the device in an appropriate way (Figure 1.18a, one could realize an ideal infinite-stage cascade cooler. Practically, the shape would

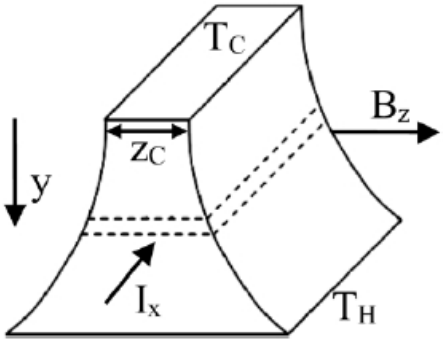

(a)

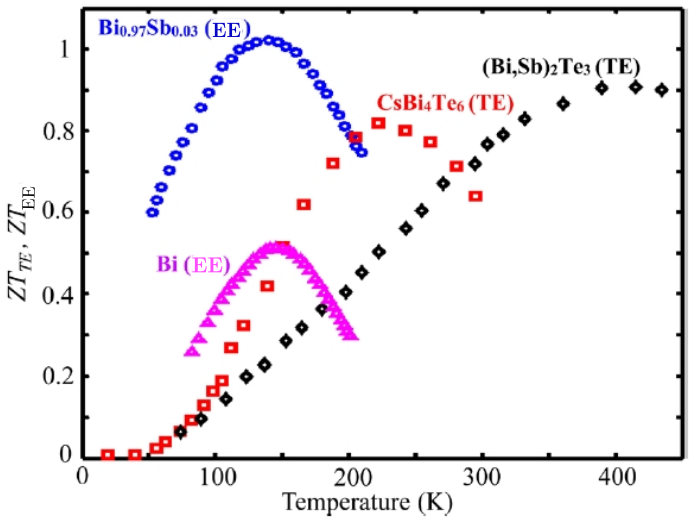

(b)

Figure 1.18: a): Sketch of an infinite-stage EE cooler. T_C and T_H represent the cold and hot side, respectively, I_x the injected current, B_z the applied field, and z_C width at the cold side. b): Plot of the figure of merit ZT against temperature for different materials: the black and red curve refer to thermoelectric coolers, the blue and purple one to EE devices [16].

be exponential along y, with the hot side wider than the cold one. Even with a simple trapezoidal shape, a significant improve in cooling has been proved [35].

The advantage of using EE coolers at lower temperatures in place of thermoelectric coolers is well displayed in Figure 1.18b, which highlights how factors of merit of circa 1 have been obtained in BiSb alloys for temperatures of around 150 K. One of the relevant disadvantages could reside in the need of employing a magnetic field, but, as explained in section 1.1, when employing AEE in magnetic materials, this requirement disappears.

Chapter 2

Experimental techniques

This chapter will be devoted to the introduction of the experimental techniques used in this work, namely Magnetic Force Microscopy (MFM) and Scanning Thermal Microscopy (SThM). These two techniques have been employed to investigate the magnetic structure of the samples and the Ettingshausen Effect, respectively. Since they both descend from the Atomic Force Microscopy (AFM) technique, a first introduction will be provided on this technique, adapting then the general theory to the cases of MFM and SThM. For each technique a theoretical review will be provided, describing the working principle, and the way the signal is detected, and the setup used in the experiments will be explained. Finally, the three (plus one) samples analysed in the experimental work will be presented, along with a magnetic characterization carried out by collaborators from Katholieke Universiteit Leuven (KUL).

2.1 AFM

The first distinction that has to be made is between contact and non-contact techniques: in the contact the tip is in physical contact with the surface, and the vertical deflection of the cantilever induced by the tip-sample interaction causes a shift of the laser reflection on the photodiode. As displayed in Figure 2.1a. which indeed pictures a typical setup for contact-AFM (c-AFM), one can see that a laser is shined on the cantilever, and its reflection is focused on a four-quadrants photodiode. Before the experiment starts, the calibration procedure consists in making sure that the reflection is exactly at the intersection of the four quadrants, so that, successively, every cantilever deflection can be correctly read as a shift of the laser reflection from the center. The AFM is used to obtain topographic maps of the sample, whether in contact or non-contact mode: in the former case this is done by injecting in the feedback loop the deflection signal and minimizing the difference between this and the set point value, chosen before the experiment. The vertical displacement of the tip is therefore modified to keep the cantilever deflection constant, and then reported as a function of the lateral displacement, building the topography map [17]. Possible versions of c-AFM are Lateral Force Microscopy [36], in which the torsion of the tip is recorded, or Force spectroscopy [37]: in this case the feedback is switched off, and the tip approaches and indents the surface in a precise point, measuring the vertical deflection. The type of c-AFM of interest for this work is SThM.

Contact AFM, however, leads to quick wearing and damage of the tip, and can also damage soft samples, due to a surface pressure larger than the yield modulus of the material [17]. For this reason, Non-Contact AFM (NC-AFM) has been developed, based on the fact that the resonance frequency of an harmonic oscillator changes when submitted to a force field.

In Figure 2.1b, the typical setup is showed: the main difference with the picture above is that in this case the cantilever is made to vibrate at a frequency equal or close to its resonance frequency. A four-quadrants photodiode is again used, and again a feedback loop is employed to maintain the vibration amplitude constant to obtain topographic maps. In this case, however, the amplitude and the phase shift, obtained with a lock-in amplifier (LIA), contain also information concerning the force field between tip and sample. For MFM, for example, the tip is coated with a ferromagnetic alloy, and the phase is sensible to the different orientation of the magnetization within the sample. Depending on whether the chosen frequency is above or below the resonance one, one works in non-contact mode, or intermittent-contact (or tapping) mode. MFM will be operated in tapping mode.

Since the basis of the technique resides on the fact that the resonance frequency of an harmonic oscillator shifts when a force field is introduced, it is possible to write the equation of motion of a damped harmonic oscillator, driven by a driving force f [17]:

$$\ddot{d} + \gamma\dot{d} + \omega_0^2 d = \frac{f}{m} cos(\omega t). \tag{2.1}$$

In this equation d is the cantilever vertical deflection, $\gamma = b/m$, with b damping coefficient and m effective mass, $\omega_0^2 = k/m$ free resonance frequency of the cantilever, with k spring constant, and ω the driving frequency. As known, the solution of this equation has the form $d(t) = A(\omega)cos(\omega t + \phi(\omega))$, with $A(\omega)$ vibration amplitude and $\phi(\omega)$ phase shift between the cantilever vibration and the force. Plugging this back in the equation, one easily obtains:

$$A(\omega) = \frac{f/m}{\left[(\omega^2 - \omega_0^2)^2 + \gamma^2\omega^2\right]^{1/2}}, \tag{2.2}$$

$$\phi(\omega) = arctan\Big(\frac{\gamma\omega}{\omega^2 - \omega_0^2}\Big) \tag{2.3}$$

However, in this development there is one missing term: the tip-sample force F_{ts}, which is exactly the quantity through which one wishes to retain information about the sample. The exact nature of this force will depend on the particular technique: this can be a magnetic force (MFM), or an attractive van der Waals force. Whatever the expression of the force, one can carry out a rough approximation, and treat this interaction as harmonic, developing the term F_{ts} in series:

$$F_{ts} = F_0 + |\frac{\partial F_{ts}}{\partial z}|_{d_0}(d - d_0), \tag{2.4}$$

with d_0 being the vertical deflection of the cantilever at rest. Now Equation 2.4 has to be added to the right-hand side of Equation 2.1, obtaining:

$$\ddot{d} + \gamma\dot{d} + \omega_0^2 d = \frac{f}{m} cos(\omega t) + \frac{F_0}{m} - \frac{1}{m}\frac{\partial F_{ts}}{\partial z} d_0. \tag{2.5}$$

In this equation the new term is ω_e, which is the effective resonance frequency, which indeed keeps into account the effect of the force field, and defined indeed as:

$$\omega_e = \sqrt{\frac{k_e}{m}} = \sqrt{\frac{k - \frac{\partial F_{ts}}{\partial z}}{m}}. \tag{2.6}$$

It becomes therefore evident what is the effect of the tip-sample interaction: an attractive force will give a positive derivative, therefore the resonance frequency will decrease, and

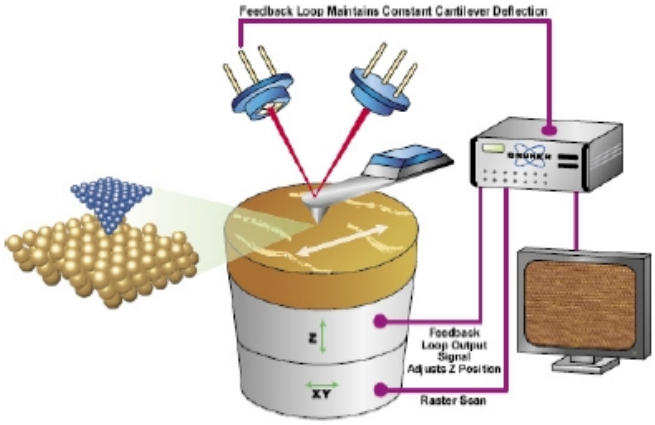

(a)

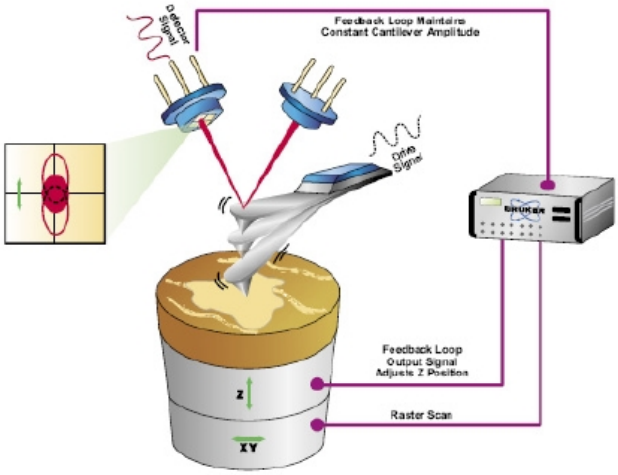

(b)

Figure 2.1: Sketch of the typical setups employed in a) contact-AFM and b) non-contact AFM [17].

vice versa for a repulsive force, as sketched in Figure 2.2a. Replacing ω_0 with ω_e in the denominator of Equation 2.3, one obtains the expression of the phase when the tip-sample interaction is included. Then, defining the quality factor as $Q = \frac{\omega_0}{\gamma}$, employing the fact that $\omega \approx \omega_0$ and developing the arctangent in series [17]:

$$\phi(\omega) \approx \pm\frac{\pi}{2} - \frac{Q}{k}\frac{\partial F_{ts}}{\partial z}, \tag{2.7}$$

$$\Delta\phi \approx -\frac{Q}{k}\frac{\partial F_{ts}}{\partial z}. \tag{2.8}$$

Equation 2.8, with $\Delta\phi$ defined as the difference between the free phase and the one when the force field starts interacting, is the key equation for NC-AFM, since it is the one that justifies the recurrence to phase maps to characterize the sample. The shift of the resonance frequency is instead employed in the feedback loop. In Tapping mode, for example, the tip-sample force will be repulsive, since the tip will enter the repulsive regime of the potential curve (Figure 2.2c) when tapping the surface. As pictured in Figure 2.2b, this means that the resonance frequency will increase ($\Delta\omega$ in the picture): choosing a drive frequency (dotted vertical line) lower than the free resonance one, the passage from the black curve to the red one will provoke an amplitude drop ΔA in the cantilever oscillation. It is this quantity that is kept constant by the feedback loop adjusting the tip-sample distance: this corresponds to keeping the gradient of the interaction force constant.

2.2 MFM

The setup usually employed to perform MFM is pretty much the same as the one displayed in Figure 2.1b: the cantilever is made to oscillate at a frequency slightly lower than its resonance (usually, a 5 % amplitude difference is picked), the signal is obtained from the photodiode response, and the amplitude drop ΔA is kept constant. In this case, however, the tip is coated with a ferromagnetic alloy, therefore the tip sample force F_{ts} discussed in the previous section will be of magnetic nature. Assuming that the technique is sensible only to the magnetic interaction, or at least that one can decouple the magnetic and the attractive vdW interaction (it will be explained below how), one can write the expression of the magnetic potential U_{mag} as $U_{mag} = -\boldsymbol{m_t} \cdot \boldsymbol{H}$, where m_t is the tip magnetic moment, and $\boldsymbol{H}$ is the stray field coming from the sample. In this case, the tip is treated as a single constant magnetic dipole, which can be magnetized along the i direction. The force will be the gradient of the magnetic potential, therefore [38]:

$$\boldsymbol{F_{ts}} = -\boldsymbol{m_t} \cdot \boldsymbol{\nabla H}, \tag{2.9}$$

$$\Delta\phi \approx -\frac{Q}{k} m_i \frac{\partial^2 H_i}{\partial z^2}. \tag{2.10}$$

The meaning of these two equations is that, as long as the magnetic properties of tip and sample are unaffected by their mutual interaction, MFM is sensible to the second derivative along z of the component of the surface field in the direction of the tip magnetization. The direction of magnetization of the tip therefore selects the component of the field the technique will be sensible to. The most delicate point is indeed understanding whether the stray field from the sample will affect the tip magnetization and vice versa. For this reason, tips with large coercive field are often used: also the value of the saturation magnetization is indeed a compromise between having a larger signal (which requires high magnetization, Equation 2.10) and having small stray fields, which means instead low values of m_t. If

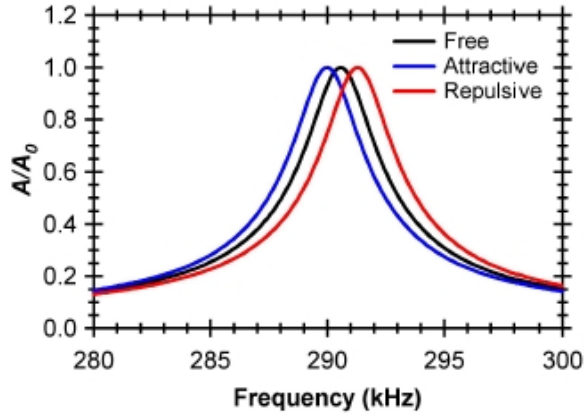

(a)

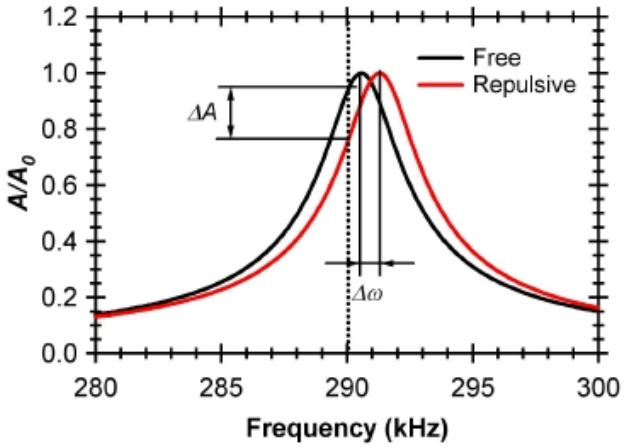

(b)

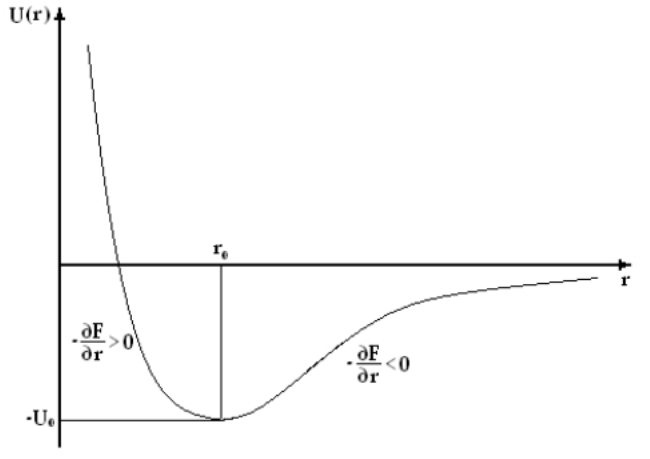

(c)

Figure 2.2: a): Amplitude of cantilever deflection A normalized to A_0 amplitude at resonance against the frequency, in the case of free oscillation (no force, black), attractive interaction (blue) or repulsive interaction (red). b): Amplitude of cantilever deflection A normalized to A_0 amplitude at resonance against the frequency, in the case of free oscillation and repulsive interaction. The vertical dotted line is the drive frequency, $\Delta\omega$ is the shift in resonance frequency, ΔA the amplitude decrease [17]. c): Sketch of the Lennard-Jones potential used to describe the tip-surface interaction: r_0 is approximately 4 Å [18].

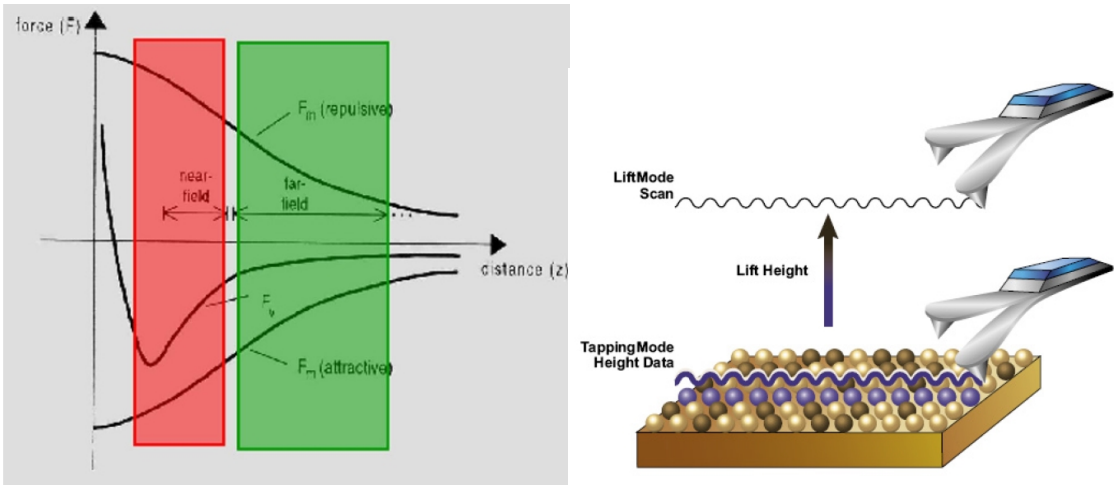

(a) (b)

Figure 2.3: a): Magnetic (first and third curve, respectively repulsive and attractive) and vdW (middle curve) force against the distance from the sample. In red the near-field regime, in green the far-field one. b): Sketch of the lift mode: a first scan is performed, then the tip is lifted and a second one is carried out [17].

indeed the magnetization is large enough to produce a field larger than the sample coercive field, the magnetic state of the sample will be changed by the tip.

However, the force term described in Equation 2.9 is not the only one in action when the tip taps the surface: beside the magnetic interaction, there will be the usual tip-sample interaction described by the Lennard-Jones potential of Figure 2.2c, repulsive at short distance and attractive at long distance. This will give rise to a total force term of the form $F_{tot} = F_{mag} + F_{vdW}$, with F_{mag} from Equation 2.9, and F_{vdW} the gradient of the Lennard-Jones potential. In Figure 2.3a the two force terms are sketched: the magnetic force (attractive or repulsive) and the vdW force. It is evident that the magnetic force is the dominant term at all distances, but the relevant quantity is the force gradient, and not the force by itself. Analyzing how this varies, one can identify a "near-field regime" (red region) in which the vdW gradient $\partial F_{vdW}/\partial z$ is larger than the magnetic force gradient $\partial F_{mag}/\partial z$, and a "far-field regime" where also the magnetic force gradient dominates. This implies that, depending on which regime is the dominant one, the phase map will display topographic or magnetic information.

To fix this issue and decouple the topographic information from the magnetic one, the "lift mode" is adopted, showed in Figure 2.3b. A first pass is performed, with the feedback on, acquiring the phase map, which is associated to the topography profile. Then, the feedback is switched off, the tip is lifted by an amount Δz lift height, and a second scan is performed, following the topographic profile recorded before, so that a constant tip-sample height is maintained. This time the phase contains the magnetic information, so that two phase maps are produced: one reflects the topography of the sample, and the other its magnetic properties. The only requirement for the lift height Δz is to ensure that the vdW force gradient is negligible with respect to the magnetic one: also in this case, one has to find the correct trade-off. Indeed, lowering the lift height allows to enhance the signal, increasing the magnetic force, but more and more topographic artefacts will appear in the map, since the influence of the vdW force gradient will be no longer negligible.

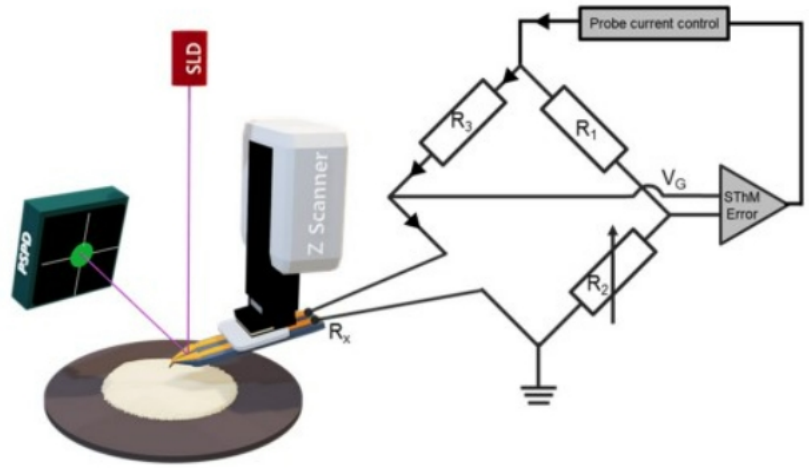

Figure 2.4: Sketch of a SThM setup: the probe is controlled by a Z piezo scanner and a laser is shined on the cantilever to record its deflection. A current is injected in the probe through a Wheatstone bridge, which is also used for the readout [19].

2.3 SThM

2.3.1 Working principle and setup

Scanning Thermal Microscopy (SThM) is one of the main techniques employed either to investigate thermal properties of the sample such as thermal conductivity k or Seebeck coefficient S or to obtain temperature maps of the sample, with the possibility to mark possible hot spots on the sample surface. This technique descends from the AFM and therefore shares many common features: the main differences reside in the type of probe, and the measurement schemes, employed to read the signal coming from the probe. There are different modes of employment for SThM: the focus here will be on the ones used in the present work. The typical setup is showed in Figure 2.4: the topography image is obtained again from the cantilever deflection, read on the photodiode. Being SThM a contact-mode AFM, the tip and sample are in permanent contact: their distance is however controlled by the feedback loop, acting to keep the cantilever deflection constant, as mentioned in section 2.1. The Wheatstone bridge depicted in Figure 2.4 serves $\rightarrow$ $input the current into the probe to heat it up, and to read the signal which is affected by the heat dissipation into the s$
The probe therefore in this case has a different function with respect to MFM and AFM: it can act as a heat source or as a temperature sensor, depending on whether the SThM is operated in active or passive mode, respectively. This is the main classification for SThM setup: in the active mode, the probe acts as a heat source, modifying the state of the sample and, depending on how the heat dissipates within it, the temperature of the probe changes and it is possible to extract quantities such as the local thermal conductivity. In the passive mode, the probe acts just as a temperature sensor, without modifying the state of the sample: again, its temperature will change depending on the one of the sample in this case, and this will lead to a signal variation. In this work, the SThM will be used in the passive mode, to detect temperature differences induced by the EE. There are many different kinds of probes which can carry out these functions: the ones used in this work are thermoresistive probes made of Pd (Figure 2.5), which change its resistance when the temperature is changed, according to the following equation[20]:

$$R(T) = R_0(1 + TCR(T - T_0)). \tag{2.11}$$

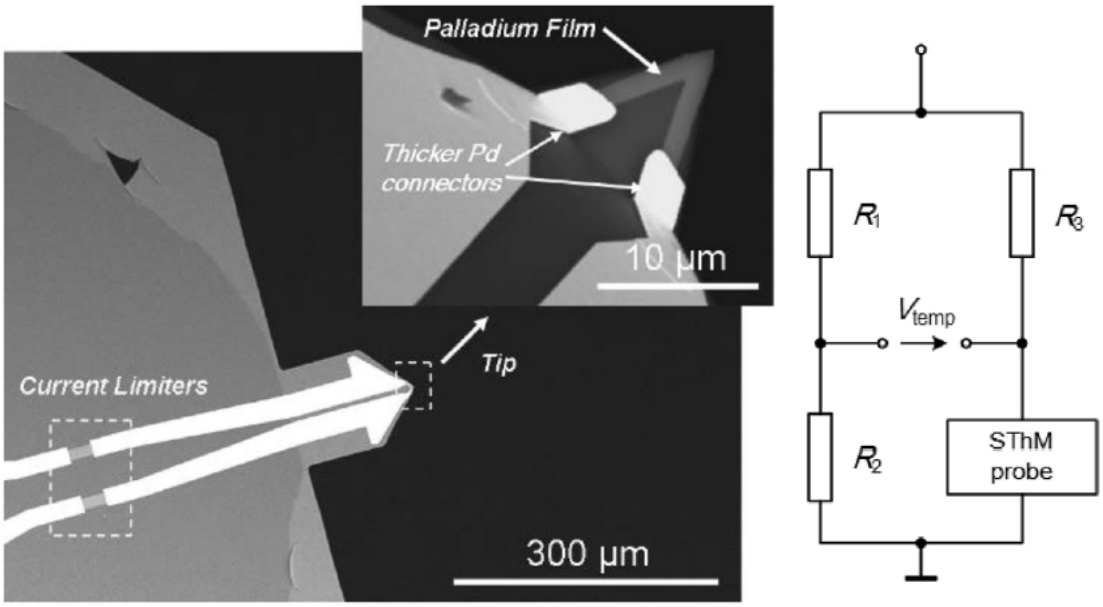

(a) (b)

Figure 2.5: a): SEM image of a thermoresistive Pd probe: the current flows in the brighter strips, on which two current limiters are deposited. The inset shows a close-up on the tip. b): Sketch of the Wheatstone bridge used in the SThM setups [20].

In this equation, TCR is the temperature coefficient of resistivity, which corresponds to the derivative of resistance against temperature, and R_0 is the resistance at the temperature T_0. T is the temperature of the tip, which is affected by the temperature of the sample in the passive mode, or by the heat dissipation in the sample in the active mode: by monitoring the variation of $R(T)$, and therefore of the signal, with respect to the lateral displacement, maps of the sample temperature can be built. Another important step is however the passage from the tip temperature to the sample temperature, taking into account the heat dissipation from tip to sample and the different thermal resistances involved. This aspect will be discussed later. Both in the active and passive mode, a current has to flow through the probe: in the passive mode, it is to measure the electrical resistance, whereas in the active mode, Joule heating is employed to generate heat. DC, AC, or a combination can be used: the latter option provides however a larger signal-to-noise ratio [39].

To measure the change in electrical resistance caused by the increase of temperature coming from the sample, Wheatstone bridges are the measurement devices usually employed in SThM setups. As sketched in Figure 2.5b, the SThM probe is indeed one of the four arms of the bridge so that, when its resistance changes, a voltage V_{temp} is detected:

$$V_{temp} = V_{cc}\Big(\frac{R_{SThM}}{R_{SThM}+R_3} - \frac{R_2}{R_2+R_1}\Big), \tag{2.12}$$

where V_{cc} is the input voltage provided to the bridge. Different versions of the scheme depicted in Figure 2.5b can be realized, inserting for example two operational amplifiers at the ends of R_2 and R_{SThM} to enhance the measurement sensitivity [40]. The bridge used in the SThM setup employed for the experiments is like the one depicted in the picture, with the addition of three capacitances in parallel to the resistors R_1, R_2, and R_3, since the voltage used has also an AC component.

2.3.2 Heat transfer

As specified above, however, the temperature of the tip never reflects the temperature of the sample, due to heat transfer mechanisms taking place between tip and sample. The focus of this brief overview will be about passive SThM in contact mode, since this is the mode employed in this work. In Figure 2.6b the main mechanisms responsible of heat transfer in contact SThM are showed: these are radiation losses, solid-solid conduction through the point contact, conduction through the water meniscus and air conduction. To each of these mechanisms, a thermal resistance can be associated: this is defined as $R^{th} = \frac{\Delta T}{Q}$ in $[\frac{K}{W}]$, where ΔT is the temperature difference between two points, and Q the heat flux flowing between them. The meaning is the same as the electrical resistance: the larger R^{th}, the more difficult the heat flow between two points kept at a fixed difference of temperature. Just like in an electrical network, all these resistances are in parallel, acting between the tip and the sample. One can therefore define a total tip-sample thermal resistance R_c^{th} as [20]:

$$\frac{1}{R_c^{th}} = \frac{1}{R_{ss}^{th}} + \frac{1}{R_{air}^{th}} + \frac{1}{R_w^{th}} + \frac{1}{R_{rad}^{th}}, \tag{2.13}$$

where the subscripts refer to the four heat transfer mechanisms introduced above, and they are assumed to be independent of one another. This is actually one of the main challenges of SThM, since each of these terms is not easy to model and depends on many parameters. In Figure 2.6a the distribution of temperatures and heat flows is showed when SThM is operated in passive mode. Moving from the higher sample temperature T_s to the lower tip temperature T_{tip}, an heat flow Q_{s-t} can be identified, and the thermal resistance R_c^{th} appears. Part of this heat flows into the cantilever (Q_{cant}) which is at ambient temperature T_a, and part (Q_{p-a}) is directly dissipated into the environment. Also an heat flow Q_{gap} flowing from the sample to the ambient in the gap can be identified.

The four mechanisms will now be considered in greater detail. Starting from the air conduction, this is relevant if the measurement is not carried out in vacuum environment. In contact mode, since the tip-sample distance is smaller than the air mean free path [20], ballistic regime has to be considered and the Fourier's law describing heat conduction cannot be used. As proposed in [41], an effective air thermal conductivity in 1D can be considered, normalized with respect to the position in the gap. The water meniscus instead forms in humid air or atmospheric condition. A thermal resistance expression dependent on the meniscus thermal conductivity and a shape factor has been proposed [42], but it has been showed that relative humidity, and the presence of hydrophobic and hydrophilic surfaces also play an important role. In contact mode, however, most of the heat is transported through the solid-solid conduction between tip and sample. A possible estimation could be $R_{ss}^{th} = \frac{R_b^{th}}{\pi b_c^2}$, where R_b^{th} is a thermal boundary resistance with units $[K/Wm^2]$, and b_c is the mechanical contact radius, defined as in Figure 2.6b. This expression however assumed an ideal mechanical contact between tip and sample, without any asperities, or liquid condensation. In reality, this is never the case, as the non-contacted regions are filled with liquid due to capillary condensation, and the smaller contact points between asperities act as parallel heat transfer paths. In a more quantitative way, when the diameter of the heat exchange area is smaller than the wavelength of the thermal energy carriers, the expression proposed above is no longer valid [20]. As for radiative transfer, when the distance between the two objects is smaller than Wien's wavelength (which is 10 μm at ambient temperature), Planck's law is no longer valid, and a different regime, called Near-Field Radiative Heat Transfer (NFRHT) dominates. An expression for the thermal resistance in NFRHT has not been developed yet, but studies concur on the relevance of

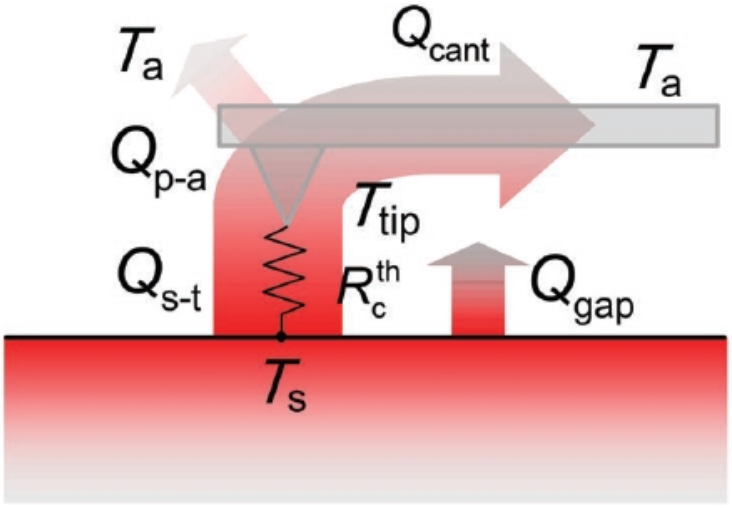

(a)

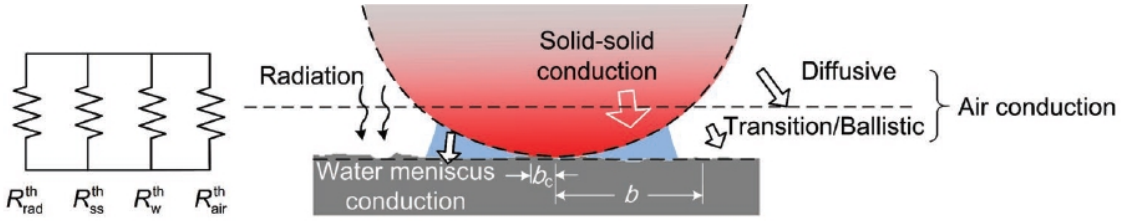

(b)

Figure 2.6: a): Schematics of the heat flow from the sample to the cantilever in passive mode with the sample, tip and ambient temperature T_s, T_{tip} and T_a respectively, the heat flows Q_i and the tip-sample contact resistance R_c^{th}. b): Schematics of the four heat transfer mechanisms between tip and sample in contact mode: on the left a sketch of the associated thermal resistances network [20].

parameters like the tip-sample distance and the tip radius of curvature [43].

The intrinsic sensitivity of these heat transfer mechanisms to the tip-sample distance are the cause for one of the main limitations of SThM, namely the topographic artifacts. Indeed, surface asperities and roughness naturally increase the heat flow from the sample to the tip, resulting in artificial hot-spots (in passive SThM) which are actually just topographic asperities. It also shares the downsides common to all contact SThM, namely the wearing down of the tip, and the impossibility to image soft materials like biological cells.

2.4 Samples employed

This section will be devoted to introducing the samples used in the present work, together with an overview of their properties thanks to the characterization carried out by collaborators at KUL. All the samples have been provided by the group of Simon Granville from the Victoria University in Welington, New Zealand.

The samples provided by Granville's group consisted of a thin film of 50-nm thick CMG grown on MgO(001). They provided two type of samples: an uncapped set of films, with the CMG exposed to air, another one capped, with a 2-nm thick layer of Tantalum, acting as capping layer, preventing the oxidation. An initial characterization of the uncapped samples at KUL confirmed indeed that at least a first surface layer of 10 nm of these samples were completely oxidised. For the EE experiments however, it is convenient to have a Hall bar, since this gives the possibility of changing the path of the injected current, and of maximising the effect by reducing the width of the sample. For this reason, the two types of thin films have been sent to collaborators at imec, for patterning the Hall bars and the deposition of gold contacts.

After this process, therefore, three type of samples were available: the Hall bars with and without capping layer, and the thin film with the capping layer. A preliminary experiment has been conducted on a different type of sample (Sample 4): this will be introduced and the experiment described in Appendix A. All of the uncapped films indeed have been sent to imec for patterning, so, for the uncapped set of samples, only Hall bars were available. In the following, these samples will be labelled as follows:

- ***Sample 1***. This is the Hall bar realized with the uncapped samples (Figure 2.7a for a picture of the film, and Figure 2.7b for an optical microscope image of the bar). The dimensions of the Hall bars are: 1 mm length, 10 μm width of the channel, and 5 μm width of the transverse arms.
- ***Sample 2***. This the Hall bar realized with the capped samples. The dimensions are the same as the ones for Sample 1.
- ***Sample 3***. This is the capped thin film (Figure 2.7c). Dimensions of the film are 1 cm x 1 cm.

MFM has been performed on Sample 1, 2, and 3, whereas the EE has been investigated only on Sample 1 and 2, since, as explained above, the thin film configuration is not suitable for this kind of experiment.

2.4.1 Characterization

The capped and uncapped CMG films have been characterized at KUL by collaborators with a VSM (Vibrating Sample Magnetometer) to retrieve the $M - B$ hysteresis curves

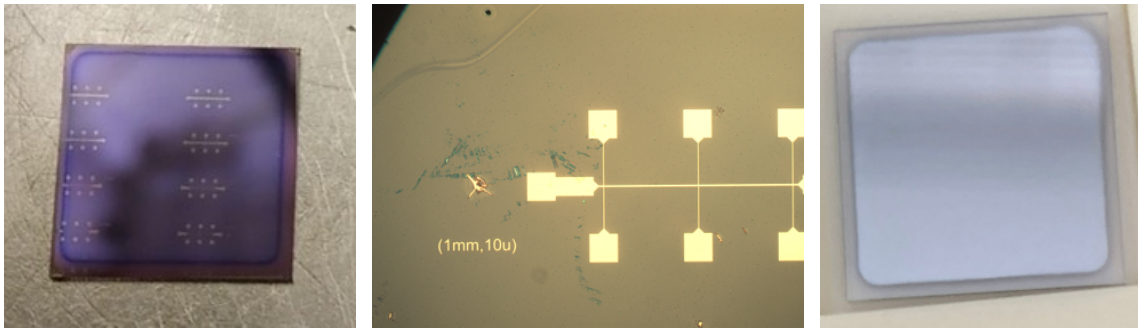

(a) (b) (c)

Figure 2.7: a): Picture of the film on which the Hall bars (Sample 1) have been patterned, from collaborators at imec. b): Optical microscope image of Sample 1, with the dimensions of the channel, from collaborators at imec. c): Picture of Sample 3.

of the samples in the OOP direction. The results are showed in Figure 2.8: the curves are rather similar to the ones present in literature, with a very small hysteresis, a small coercive field (30 and 8 mT for uncapped and capped samples, respectively), and a large saturating field. These quantities are summarised in Table 2.1. Obviously, the reference curves for Sample 1 constitute the first row of Figure 2.8, whereas the magnetic characterization of Sample 2 and 3 has to be confronted with the curves of the second row. The magnetization difference between the two hysterestic states (the two branches of the curve visible in Figure 2.8b and 2.8d) results to be particularly small, and equal to 25 emu/cm^3 for uncapped CMG and 15 emu/cm^3 for the capped samples, which is anyway above the magnetic resolution of common MFM setups [44]. However, the magnetization values should be interpreted with a 10 % relative error, coming from uncertainty about the sample volume. This uncertainty is also the likely cause of the maximum magnetization of Figure 2.8d being larger than the saturation magnetization of Figure 2.8c. The hysteresis cycles close both around 300 mT: from this point on, the magnetization in the sample is uniform, and it increases until saturation. The saturation occurs for a field higher than 1 T, confirming that, with the setup at our disposal, which will be described in the next chapter, it will not be possible to saturate the samples.

The capped CMG hysteresis cycle in Figure 2.8d shows a much irregular trend with respect to the one of the uncapped sample: this is due to an issue of sample misalignment in the VSM which generates this erratic trend. Also, the virgin curve of magnetization in the same graph does not exactly start from zero magnetization: this is due to a correction performed on the data to correct for trapped field lines in the superconducting coils which generate the magnetic field in the VSM.

Structural characterization has been carried out by the same collaborators at KUL, confirming: i) the oxidation of all the elements in the uncapped sample for a depth of 10 nm at least, ii) the oxidation of the Ta capping layer, in the first surface layers of the capping coating, forming Ta_2O_5, iii) the Heusler structure in the material and iv) the $L2_1$ ordering.

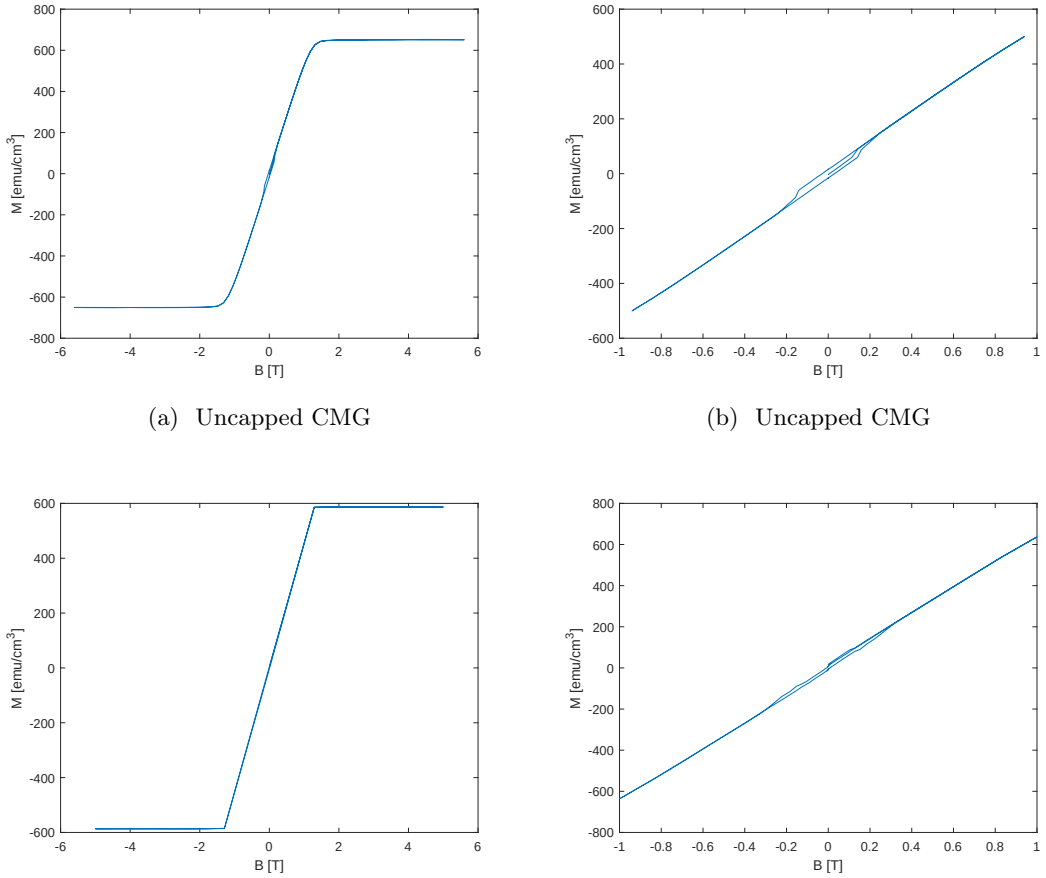

(a) Uncapped CMG

(b) Uncapped CMG

(c) Capped CMG

(d) Capped CMG

Figure 2.8: Hysteresis curves for OOP magnetic field obtained from collaborators at KUL, reproduced with permission, for (a-b) uncapped CMG and (c-d) capped CMG. b) and d) are a zoom-in on the hysteresis cycle.

	Uncapped CMG	**Capped CMG**
$\boldsymbol{B_c[mT]}$	30	8
$\boldsymbol{B_s[T]}$	1.5	1.3

Table 2.1: Coercive field B_c and saturation field B_s for capped and uncapped CMG, from the experimental hysteresis curves.

Chapter 3

Experimental results

In this chapter, the experimental results gathered to characterize the magnetic structure of CMG and to investigate the presence of the EE will be presented. The first section will concern MFM and the introduction of the phase maps which contain the information about magnetic domains: first the experimental setup employed will be presented, and then the results obtained for each sample. The same structure will be followed for the thermomagnetic characterization, namely the investigation of the EE. As explained above, however, this experiment has been performed only with Hall bars, therefore only with Sample 1 and 2. Finally, the last section will be devoted to the discussion of the results, also in view of the characterization performed at KUL.

3.1 Magnetic characterization

3.1.1 Experiment setup

The goal of this experiment was to observe the magnetic domain walls in CMG and their change, as the applied external magnetic field was varied. Also, having three different samples at disposal, the aim was to understand whether the different geometry (Hall bars *vs* thin film) or the presence of the capping layer affected in any way the magnetic structure.

The magnet at our disposal were two electromagnets, which generate an out-of-plane field. Since, as discussed in section 1.1, the field needed to saturate CMG in the OOP direction is roughly 1 T, the bigger magnet was picked, whose maximum field was however 700 mT. The thickness of the PCB on which the sample was mounted was circa 2 mm, and the sample was centered on the electromagnet: the calibration curve of the magnet at a distance of 2 mm from the surface on the electromagnet and centered on top of it is represented in Figure 3.1c. This calibration curve has been then confirmed by measurement of the magnetic field with different applied currents with a gaussmeter. The orientation of the magnetic field was checked beforehand, finding that for positive current the magnetic field points downward (as showed in Figure 3.1a), and this will be considered as a positive magnetic field in the following, with the orientation switching by reversing the current. The setup is sketched in Figure 3.1a, whereas Figure 3.1b shows a picture of the actual setup. The sample sits on the electromagnet, and it is magnetized before starting the experiment applying a negative current of -20 A correspondent to a magnetic field of -700 mT (step 1 in Figure 3.2). Therefore the sample is initially magnetized with $\boldsymbol{M}$ pointing upward, as in the sketch. Then the field is brought to zero (step 2) and the tip is magnetized in the direction of positive field, so downward. The tips used in the experiment had a coercitivity of circa 30 mT [45], and have been magnetized by inserting them into the gap of a U-

shaped magnet, with the appropriate orientation. It is important to magnetize the tips in the same direction as the field that will be applied in the experiment, so that one does not risk reversing the tip magnetization unexpectedly while performing the MFM scan. It is now possible to start scanning, and then progressively increasing the field, up to the maximum positive field of 700 mT (step 3). It has to be remarked that the electromagnet heats up quickly when subject to currents larger than 10 A, and it is indeed provided with a water-cooling system. Despite the cooling, the heating may anyway affect the scans at high magnetic field.

The procedure followed is summarized in Figure 3.2, with the steps described above numbered from 0 to 3. Since at the moment of the experiment the experimental hysteresis curves of the samples were not available yet, the working hypothesis was that the samples behaved as the hysteresis curve showed in Figure 3.2. As it can be noted, the magnetization field of the sample (-700 mT) is smaller than the actual saturation field, therefore one can assume that not all the domains were initially aligned in the sample direction. How domains behave when an external magnetic field is swept from negative to positive has been described in section 1.3: based on that analysis, the expectations are to observe domains with different orientations for field close to the coercive field (reported in Table 2.1 with the experimental values), and rotation of the magnetization in the field direction for higher fields. As explained in section 2.2, and from Equation 2.10, MFM is sensible to the second derivative of the component of the field in the direction of the tip magnetization: what this means is that, in this experiment, the technique will only be sensible to magnetic domain walls for domains magnetized OOP. The domains with IP magnetization, which is the easy plane for CMG, and should be the majority at zero field, will not give any signal.

3.1.2 Sample 1

The procedure followed for the measurements on Sample 1 is the one described above. In this case, since the coercive field is reported to be around 30 mT, the first analysis was conducted on this range of fields, in particular from 0 to 120 mT, and then back to zero again. In each case, the topography image has been recorded as well (an example is given in Figure 3.4a), and the scan has been performed always on the same area, comprising the whole channel in all its width. In order to include all the channel, indeed, these maps have dimensions 35 μm x 11.6 μm. The scanned area is in between the second and third arm, as highlighted in Figure 3.3, since this was a rather clean area, which is important to minimize the topographic artifacts in the magnetic phase maps. A scratch was however present and this has been used as alignment mark for the different maps. About the scanning procedure, first the topographic image is optimized by tuning the integral I and proportional gain P, as well as the setpoint amplitude A_{sp}. The first two act on the gain of the feedback, to reduce the error signal, the latter fixes the setpoint oscillation amplitude of the cantilever. In this case, these parameters have been tuned at $I = P = 4$, and $A_{sp} = 400\ mV$: the oscillation is in V, but can be easily converted in nm by acquiring an amplitude-displacement curve plotting the output of the photodiode in V against the tip displacement in nm. The slope of the curve is the conversion factor. After the optimization, the lift mode is enabled, and magnetic phase maps are acquired. Some parameters are however changed with respect to the topographic mode, such as the drive frequency, which is modified to a value slightly smaller than the resonance one, as discussed in section 2.2. During all the scans, the lift height has been kept at $h = 80\ nm$. Two sets of measurements will be discussed: a first one from 0 to 120 mT, and a second one from 120 to 700 mT.

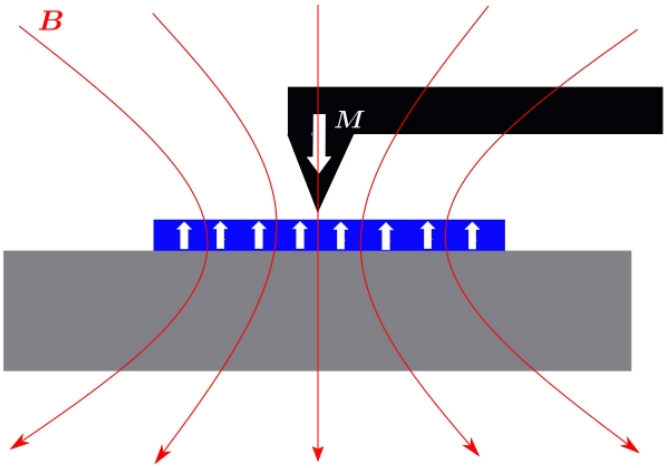

(a)

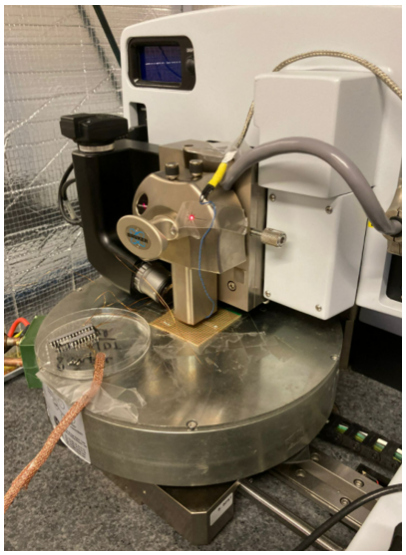

(b)

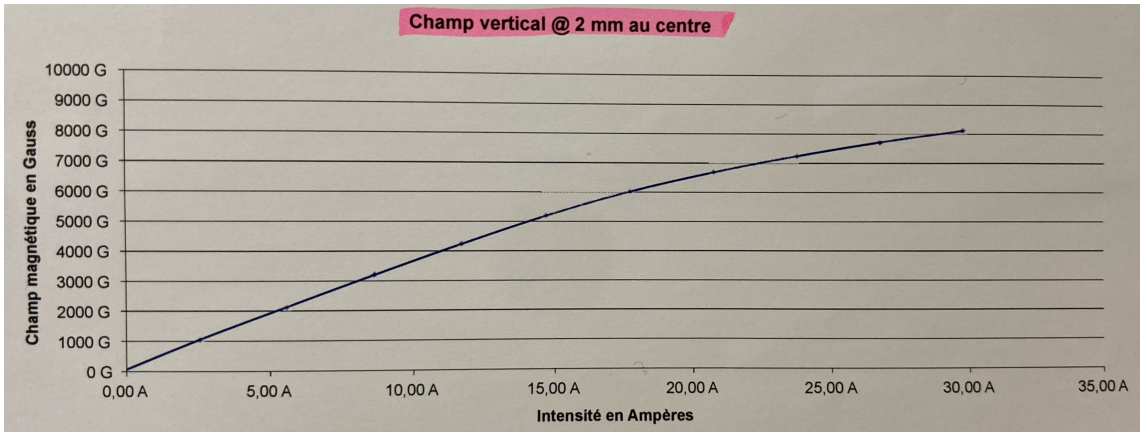

(c)

Figure 3.1: Sketch (a), with the electromagnet, the sample and the tip from bottom to top, and picture (b) of the setup employed for the MFM experiments. c): Calibration curve B-I of the employed electromagnet at a distance of 2 mm from the surface and centered on top of the electromagnet.

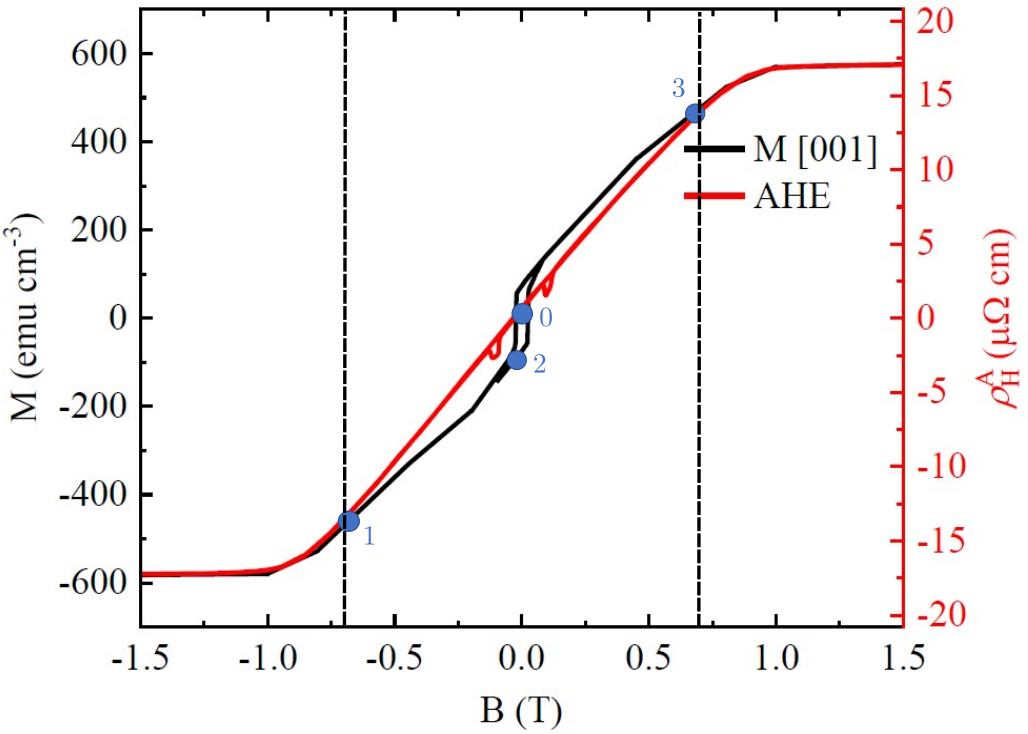

Figure 3.2: M-B hysteresis curve of CMG in the OOP direction, with the magnetization in black and the AHE signal in red. The dotted lines represent the minimum and maximum field available in the experiment ($\pm$ 700 mT), whereas the blue dot are the different steps of the experiment procedure. Adapted from [21].

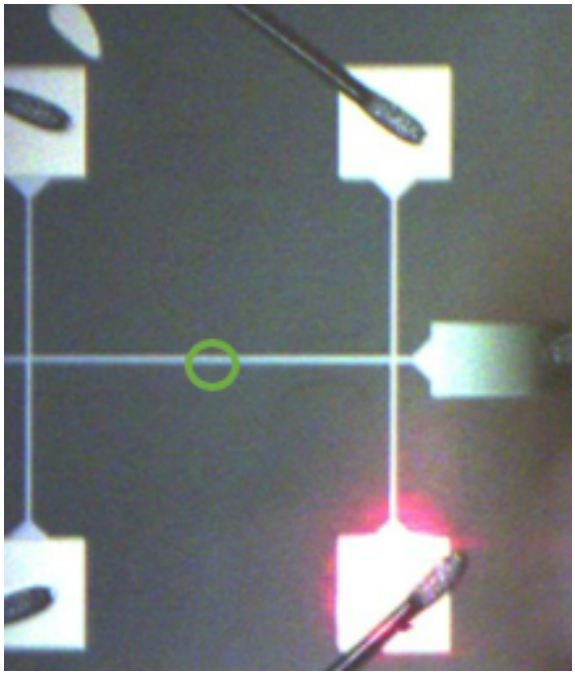

Figure 3.3: Picture of Sample 1, the green circle highlights the scanned region.

The results for the first set are showed in Figure 3.4: the field has been increased from 0 to 50 mT at steps of 8 mT, then to 120 mT, and back to zero again, to observe the effect of the hysteresis. Already at zero field, a structure made of intersecting transversal lines is evident: it is worth recalling that i) the only domain giving a signal will be the OOP oriented ones, ii) the sample was not magnetized at saturation at the beginning and iii) the easy plane is the film plane. Putting these three inputs together, it is hard to understand the origin of these structures: since the easy plane is the film plane, indeed, any domain relaxing at zero field should orient its magnetization in plane, according to shape anisotropy, and therefore give no signal. Increasing the field to 8 mT, Figure 3.4c shows a very clear square domain structure, with some of the line feature from Figure 3.4b already changed. The magnetic structure keeps then on changing as the field is increased to 16 and 25 mT (Figure 3.4d and 3.4e): in particular, most of the transversal lines going from bottom left to top right disappear, generating a rectangular domain structure. For higher fields, (B = 33 mT and 42 mT) this structure does not change much, as most of the transversal top left - bottom right lines are retained in the maps. At $B = 50mT$ (Figure 3.4h) and $120mT$ (Figure 3.4i) also these features disappear, however, with the last map showing no contrast at all. In these two maps, furthermore, a topographic artifact can be spotted: indeed, the scratch used as alignment mark is present, signaling a cross-talk between topographic and magnetic information. Most likely for these two measurements the lift height was not large enough. Going back to zero field (Figure 3.4j) the effect of the hysteresis is clearly visible: this map is clearly different from the second one.

The second set of measurements will now be discussed: in this case the starting point was directly B = 120 mT, with the field increased to the maximum value of 700 mT. The aspect ratio of these maps is different from the first ones: also in this case, however, all the channel is well visible in the maps. Also in this case in Figure 3.5a a scratch is visible in the bottom region of the channel, which has been used as alignment mark. Some shifts are evident in the maps with higher fields, and this is probably due to vibrations caused by the water cooling system. It is immediately evident that the magnetic structure is rather different from the one at low field: even at 120 mT in this case, some contrast is visible, with black dots clearly visible. This kind of features remains pretty much fixed during all the scans, whereas the rest of the map changes, developing an enhanced contrast for larger fields.

The absence of contrast in the $B = 120$ mT map can have two different interpretations: i) all the domains are already magnetized in the OOP direction, therefore there is just one big domain, or ii) in switching from an upward (↑) magnetization state to a downward (↓) magnetization state, the domains assume the easy plane orientation, and larger fields are needed to totally reverse their magnetization. If hypothesis i) were true, then one would need to explain the contrast obtained in the maps presented in Figure 3.5, for fields larger than 120 mT. On the other hand, hypothesis ii) clashes with the experimental evidence that at zero field the domains relax in the easy axis direction, meaning IP. As it will be discussed in section 3.3, the peculiar structure of these domains defies one of the three inputs defined above, leading to visualizing IP domains even if the tip is magnetized OOP.

3.1.3 Sample 2

For Sample 2, the small field regime (0-50 mT) was investigated to analyse a possible presence of the square domain structure. The parameters employed to optimize the topography map are the same as for Sample 1, and also in this case the lift height was set at $h = 80\,nm$. The correct magnetization of the tip is confirmed by the evolution of the

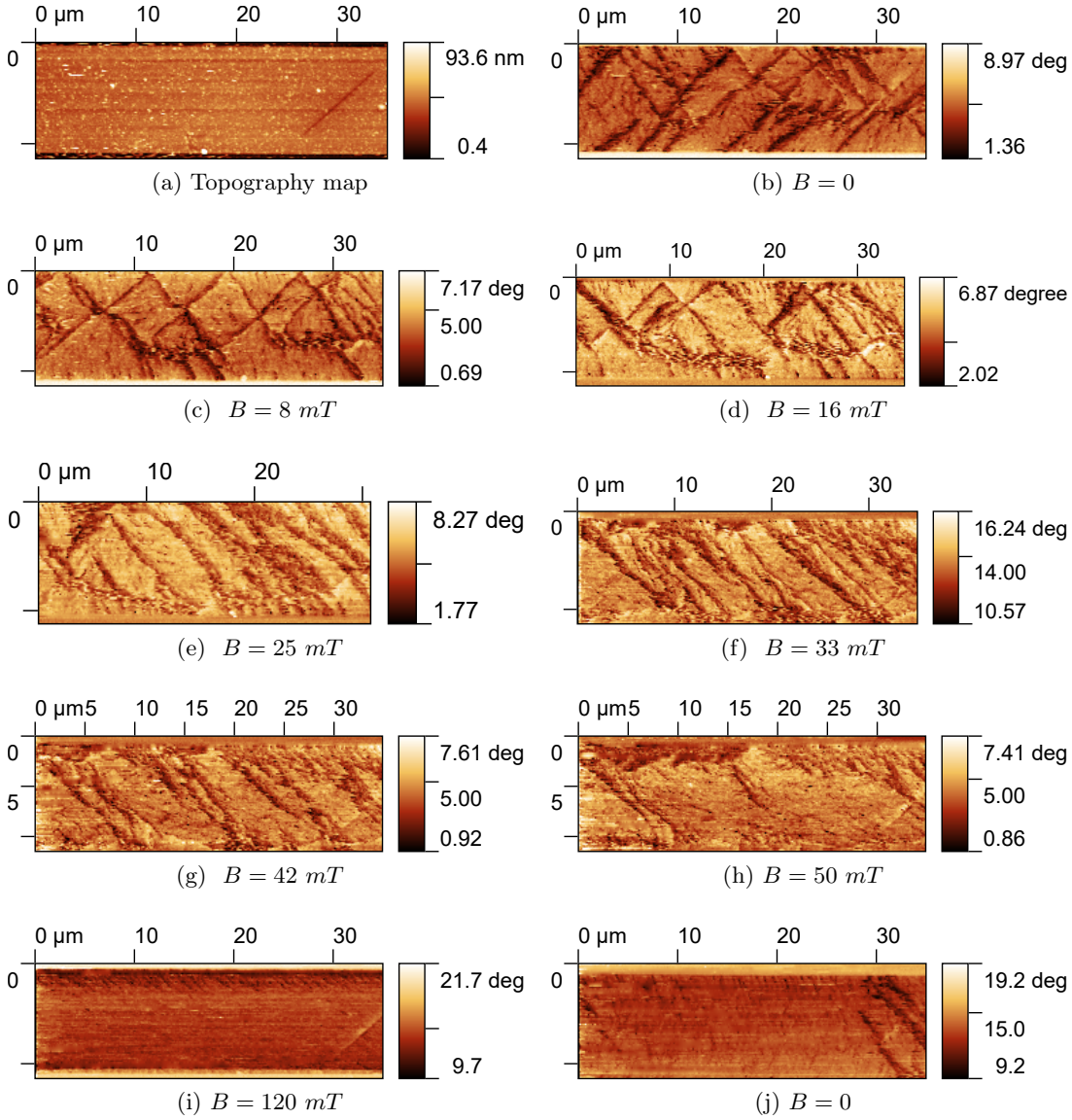

(a) Topography map (b) $B = 0$

(c) $B = 8\ mT$ (d) $B = 16\ mT$

(e) $B = 25\ mT$ (f) $B = 33\ mT$

(g) $B = 42\ mT$ (h) $B = 50\ mT$

(i) $B = 120\ mT$ (j) $B = 0$

Figure 3.4: Experimental results obtained for the magnetic characterization of Sample 1. a): Topography map of the scanned region. Magnetic phase maps of the sample with the field increasing from 0 to 50 mT at steps of 8 mT (b-h), then to 120 mT (i) and finally back to zero (j).

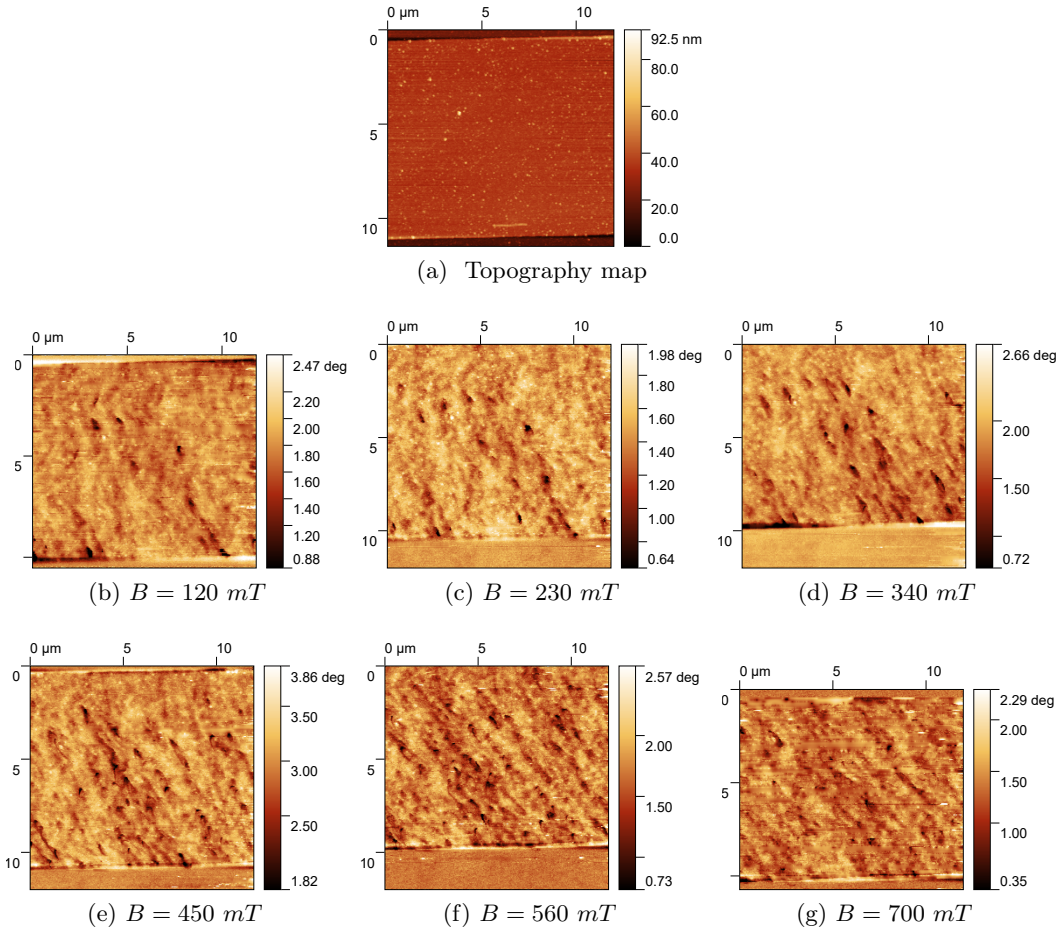

(a) Topography map

(b) $B = 120\ mT$ (c) $B = 230\ mT$ (d) $B = 340\ mT$

(e) $B = 450\ mT$ (f) $B = 560\ mT$ (g) $B = 700\ mT$

Figure 3.5: Experimental results for the magnetic characterization of Sample 1. a): Topography map of the scanned region. Magnetic phase maps of the sample with the field increasing from 120 to 700 mT at steps of 110 mT (b-g).

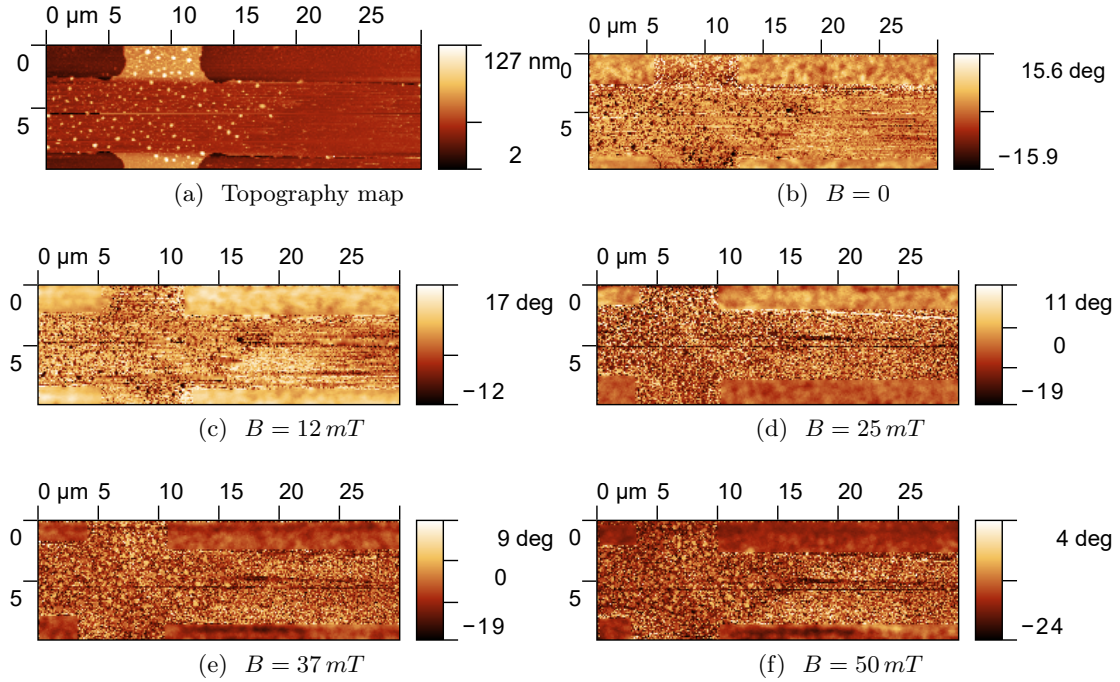

(a) Topography map (b) $B = 0$

(c) $B = 12\,mT$ (d) $B = 25\,mT$

(e) $B = 37\,mT$ (f) $B = 50\,mT$

Figure 3.6: Experimental results for the magnetic characterization of Sample 2. a): Topography map of the scanned region. Magnetic phase maps of the sample with the field increasing from 0 to 50 mT at steps of 12 mT (b-f). In these maps, a mean value filter on the region outside the channel has been performed.

resonance frequency with the field: as B is increased, the resonance frequency increases as well, signaling a repulsive interaction, and meaning that indeed the tip is magnetized in the direction of the field.

In Figure 3.6 the results obtained for the magnetic characterization of Sample 2 are showed, starting from a topography map provided for reference, together with the phase maps at increasing field. In this case, the scanned region is at the intersection of the channel with the central arm, as it is clear in Figure 3.6a: the region results however to be quite dirty, with many spots on the surface which could affect the quality of the magnetic maps. All the magnetic phase maps recorded were rather noisy, either inside and outside the channel: for this reason, a mean value filter has been applied in the region outside the channel, identified thanks to a mask built from the topography map. In this way, the possible magnetic features inside the channel can be more clearly identified. However, no clear pattern can be identified in the magnetic maps: the magnetization of the sample seems to be very uniform. The only discernible feature identifiable is the border of the channel, visible for example in Figure 3.6d, confirming that at least a discontinuity in the signal is present when moving from the magnetic sample to the non-magnetic substrate. As a possible cause for the poor resolution of the images, the demagnetization of the tip can be ruled out, since it has been re-magnetized in between each scan, to ensure that indeed the setup was performing properly. Some intrinsic noise coming from the setup could have contributed to bury the magnetic features in noise.

3.1.4 Sample 3

The same experiment was repeated for Sample 3, the capped film, to investigate the origin of the square domain structure. Also in this case the topography image was first optimized, tuning the parameters to the same values as the ones used for Sample 1. Different regions of the film have been analysed, in order to look for the cleanest one and minimize the effect of topographic artifacts on the magnetic phase maps.

The regime of small field (0-50 mT) was first analysed, to try and observe the square domain structure, then the field was increased up to the maximum value. Already looking at Figure 3.7b, there is no defined structure: some of the features observed, indeed, like the dark stripe in the top region, are probably topographic features, since they compare also in Figure 3.7a. Increasing the field to 50 mT the situation does not change significantly: some of the spots disappear but, overall, the background remains noisy and no clear structure can be identified, pointing toward a uniform magnetization in the sample. Moreover, some ripples in the maps can be spotted (like in the topographic map or in Figure 3.8d): looking at the time evolution of the signal while performing the scan, it probably is 50 Hz noise picked up by the signal from some electrical connection. For small fields, however, there is no sign of the structure observed on Sample 1. There could be two possible causes of the noisy background observed in Figure 3.7b - 3.7f: the first could be a demagnetization of the tip over time, which however did not occur during the consecutive scans of Sample 1, which lasted the same amount of time as these; another possible issue could be that the tip, while scanning over the sample, picked up some dirt which reduced its sensitivity. The sample was indeed quite dirty, and, after performing some tip ramps, the quality of the maps indeed improved. Performing a ramp corresponds to turning off the feedback, fixing the tip in one single point, and approaching the surface: the contact with the surface could indeed contribute to cleaning the tip from possible dirt accumulated over time. The background of the maps in Figure 3.7 is however very similar to the maps of Figure 3.6 for Sample 2. One can then start assuming a link between the magnetic structure in Sample 2 and 3 with the capping layer, which is significantly different from the one of Sample 1, without the Ta coating.

Increasing again the field (Figure 3.8), the elongated features already evident in some of the previous maps increase in number: similar features are also present in the topography map, showed in Figure 3.8a, which suggests the hypothesis that these are topographic artifacts. In these maps, furthermore, a large residue was present in the center of the scanned area, which pops up even in the magnetic phase maps. Increasing indeed the field from 100 to 700 mT does not significantly change the maps, as if the magnetic information were masked by the topographic one. In Figure 3.8e the map for $B = 700\ mT$ shows a different aspect ratio with respect to the other ones: this is due to the heating of the magnet which forced us to stop the scan. As mentioned in the introduction, in fact, the magnet, when supplied with maximum current, heats up noticeably, despite the water cooling system. This heat is transferred to the cantilever which expands due to thermal expansion: this expansion acts on the behaviour of the piezoelectric scanner, which retracts as if the surface was sloped. After a while, the piezoelectric reaches its retraction end of range, and the scan has to stop. This is why the maps obtained at maximum magnetic field are rarely completed. One way to avoid this would be to wait for the thermalization of the whole magnet and probe system, but, given the dimensions of the magnet, this solution is quite time-consuming (after one hour, the temperature kept increasing).

To look into the hypothesis that the features observed in the magnetic map come indeed from surface characteristics of the sample rather than from magnetic information, the Pear-

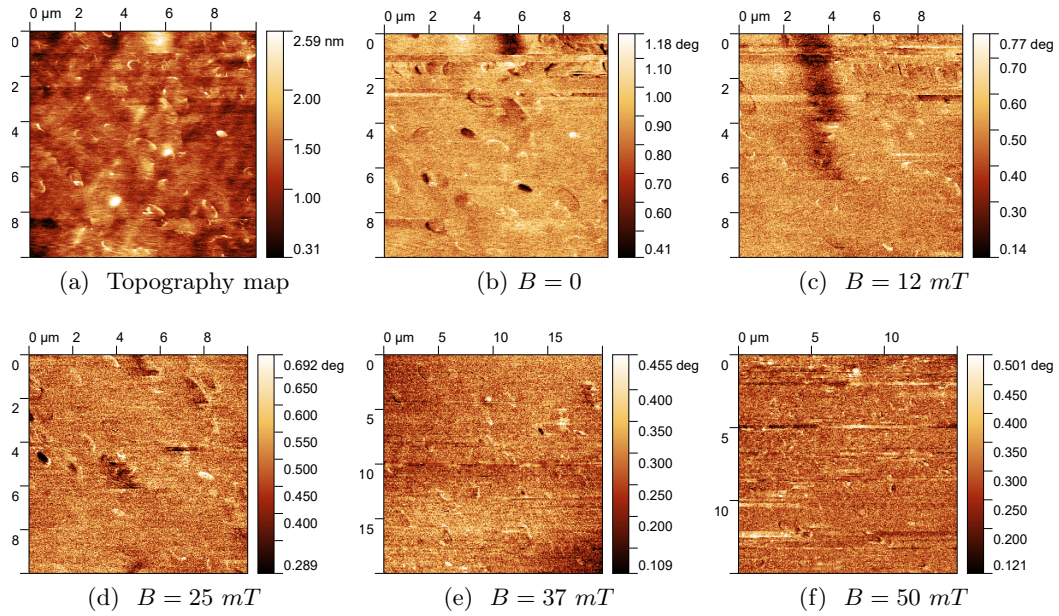

(a) Topography map (b) $B = 0$ (c) $B = 12\ mT$

(d) $B = 25\ mT$ (e) $B = 37\ mT$ (f) $B = 50\ mT$

Figure 3.7: Experimental results obtained for the magnetic characterization of Sample 3. a): Topography map of the scanned region. (b-f): Magnetic phase maps for increasing magnetic field from 0 to 50 mT at steps of 12 mT.

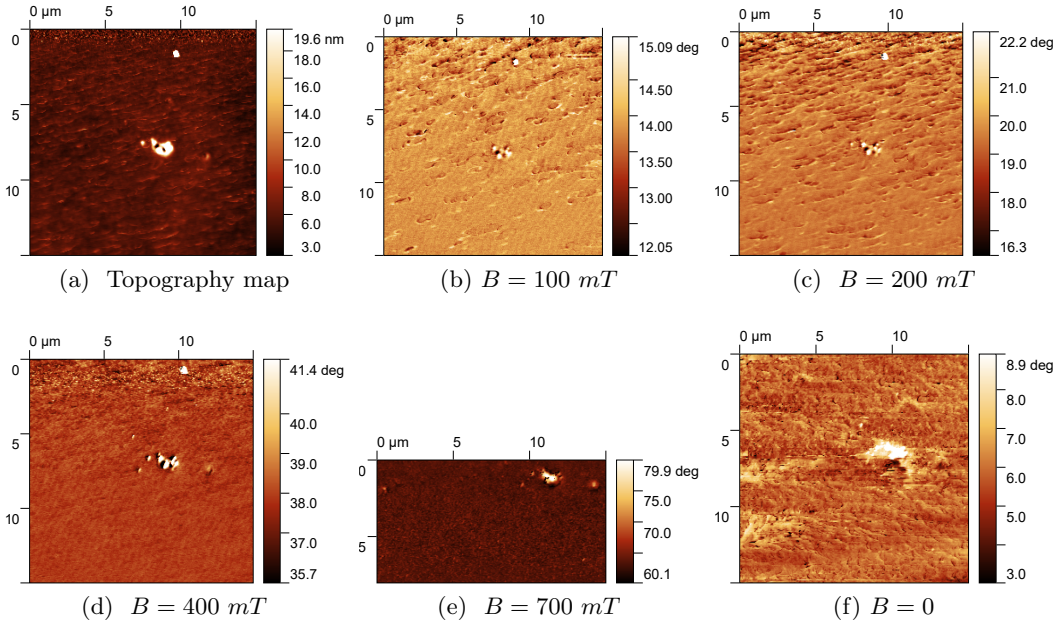

(a) Topography map (b) $B = 100\ mT$ (c) $B = 200\ mT$

(d) $B = 400\ mT$ (e) $B = 700\ mT$ (f) $B = 0$

Figure 3.8: Experimental results obtained for the magnetic characterization of Sample 3. a): Topography map of the scanned region. (b-f): Magnetic phase maps for higher magnetic fields, from 100 to 700 mT, and then back to 0.

Map	Pearson coefficient	**Map**	Pearson coefficient
$\boldsymbol{B = 0}$	0.075	$\boldsymbol{B = 100\ mT}$	0.31
$\boldsymbol{B = 12\ mT}$	-0.15	$\boldsymbol{B = 200\ mT}$	0.32
$\boldsymbol{B = 25\ mT}$	0.05	$\boldsymbol{B = 400\ mT}$	0.33
$\boldsymbol{B = 37\ mT}$	0.22	$\boldsymbol{B = 700\ mT}$	0.37
$\boldsymbol{B = 50\ mT}$	0.01	$\boldsymbol{B = 0}$	0.45

Table 3.1: Pearson coefficient calculated for all the magnetic maps for Sample 3.

son coefficient between the magnetic and topographic map has been calculated (Table 3.1) for each one showed in Figure 3.7 and 3.8. The Pearson coefficient expresses the degree of linear correlation between two sets of data: this is limited between -1 and 1, with -1 being complete anti-correlation, 1 being complete correlation, and 0 no correlation at all. Therefore a coefficient close to zero would imply that indeed the features observed in the maps stem from magnetic information (or, at least, they do not reflect topographic features), whereas a value close to 1 would mean strong correlation between the two maps. What jumps to the eye is that the low field maps are much more uncorrelated to the correspondent topographic maps than the high field ones. On one hand, this can indeed signify that the elongated features observed in Figure 3.8 are not magnetic, but another element has to be considered. Indeed, the big residue in the center, which is clearly a topographic artifact, appears in all the magnetic maps and this could be partly responsible of the larger value of the Pearson coefficient. To explain however such a difference between the Pearson number at low and high field, it is likely that the black spots visible in Figure 3.8 are indeed of topographic origin.

3.2 Thermomagnetic characterization

3.2.1 Experiment setup

As described in the previous chapters, the goal of this experiment is to observe the EE and detect the temperature difference which it induces by employing SThM. Due to limitations in our setup, the first option available was to use the same electromagnet used for MFM, generating an OOP magnetic field: this means that, by injecting an electric current along x, the Hall bar channel direction, the symmetry of the effect dictates that a temperature difference should develop along y, so across the width of the bar. The working hypothesis are that: i) this temperature difference is larger than the temperature resolution of the SThM setup, ii) it is possible to scan and detect this temperature difference before it thermalizes. The setup is sketched in Figure 3.9a and a picture of the real one is provided in Figure 3.9b. and 3.9c. The main idea is scanning the whole channel, including all the width, like it has been done for the MFM, and demodulating the SThM signal coming from the bridge. Indeed, since an electric current runs in the device, the Joule effect will be present as well, most likely masking the EE. The key element here, as described in [46], is to apply an AC current oscillating at f_{bias} through the device: the Joule heating will be proportional to I^2, therefore its spectral component will be at $2f_{bias}$, the EE instead will have a spectral component at f_{bias}, since it is linearly proportional to the current. Using a lock-in, therefore, the first harmonic at f_{bias} of the SThM signal is plotted in the maps: the amplitude of the first harmonic will be proportional to the module of the temperature difference, its phase to the sign [47].

The setup is arranged as follows: the signal for the probe, which consists of an AC peak-to-

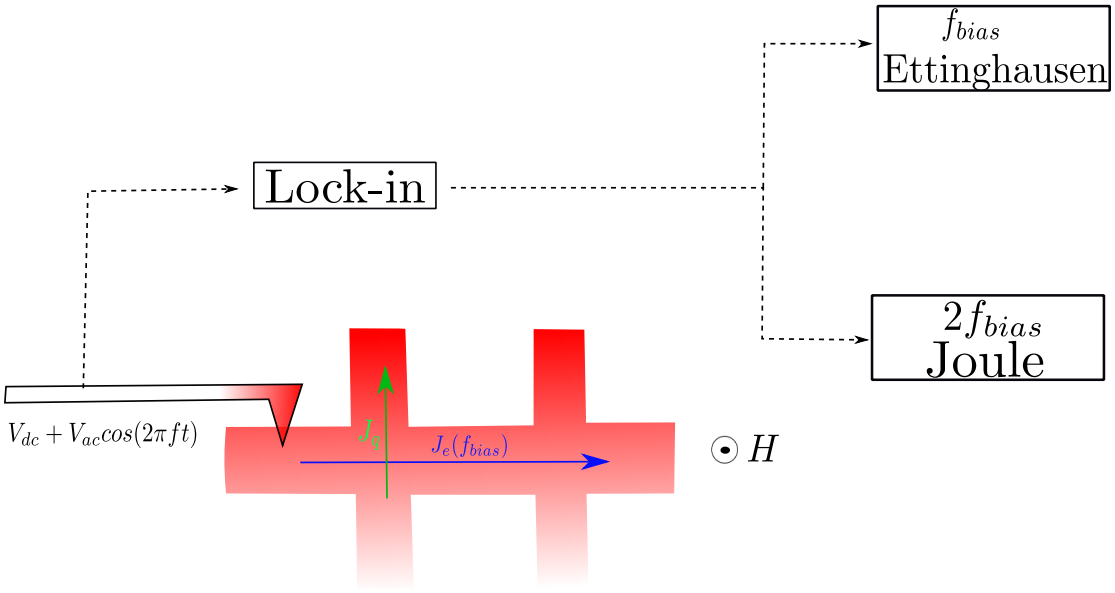

(a)

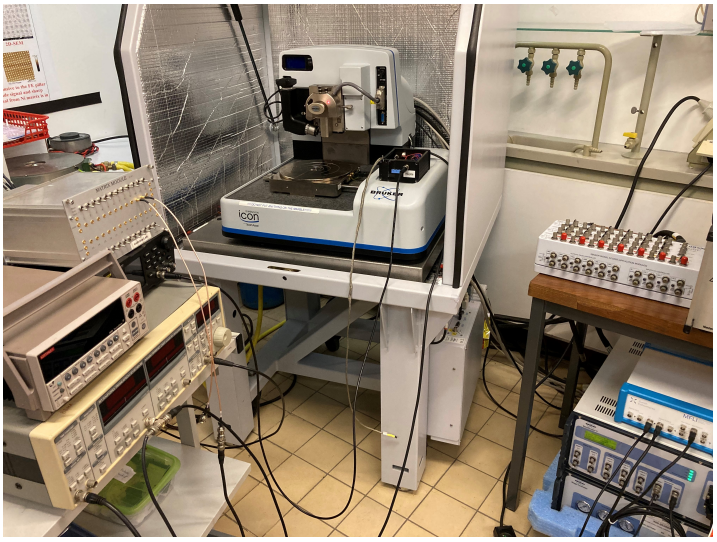

(b)

(c)

Figure 3.9: a): Sketch of the setup used for the thermomagnetic characterization. $J_e(f_{bias})$ is the electrical current, J_q is the heat current developing, H the magnetic field. b):Pictures of the setup used, with matrix module, power supply, function generator and preamplifier (left), the electromagnet with the sample and the microscope (center) and the lock-in with the microscope controller on the bottom right. c): Picture of the Wheatstone bridge employed.

peak component $V_{AC} = 4V$ oscillating at 91 kHz, and a DC component $V_{DC} = 1V$ is fed to the input of the Wheatstone bridge by the signal generator (black box in Figure 3.9b). The output of the bridge is first connected to the preamplifier (grey tool below the others in Figure 3.9b) to be able to instantly read the SThM signal. Moreover, the preamplifier performs a first low-pass filtering of the signal. Its output goes to the lock-in amplifier (LIA), which demodulates the signal. The current into the device is regulated and injected through the matrix module: its connection to the sample holder is the thick wire displayed in Figure 3.1b. The matrix module allows to select between which pins the current flows: after having associated each pin of the PCB to the ones of the matrix module, it is possible to select the two at the end of the channel. The current can be inputted either through the power supply on top of the preamplifier, or through the LIA itself, connecting the selected pins in the matrix modules to the tool of choice: in the experiments, this last option has been preferred due to the easiness of operation of the LIA parameters. Then, the LIA is connected to the module of the AFM in order to plot in the customised software used for the scans the amplitude and phase of the first harmonic demodulated by the LIA.

In this experiment, critical parameters are the ones linked to the thermal time constants of the sample and of the tip. There are two important assumptions to verify: i) whether or not the device reaches steady state at each excitation cycle (this corresponds to the DC component of the temperature in the sample being independent of the current frequency) and ii) that there is enough time for the tip to thermalize to the temperature of the sample. The first one of these hypothesis is linked to the thermal time constant of the sample τ_s with respect to f_{bias}, the second one to the thermal time constant of the probe τ_t with respect to the scan speed. The temperature of the sample T_s can indeed be separated in three components, as explained above, with $\omega = 2\pi f_{bias}$ [48]:

$$T_s = T_{s,DC} + T_{s,1f}\, sin(\omega t) + T_{s,2f}\, sin(2\omega t), \tag{3.1}$$

where $T_{s,DC}$ derives from room temperature and a Joule heating component, $T_{s,1f}$ stems from the EE and $T_{s,2f}$ from the Joule heating entirely. The DC component can be expressed as [49]:

$$T_{s,DC} = T_{s,2f}\sqrt{1 + (2\omega\tau_s)^2} + T_{RT}, \tag{3.2}$$

where T_{RT} is room temperature. This equation expresses how the DC component of the temperature, which is the room temperature on which a Joule heating is superposed, varies with the current frequency ω. If the inverse of the frequency is much larger than the sample thermal constant ($\omega\tau_s << 1$), then the DC component is independent of the frequency. The sample thermal time constant in the transverse direction has been simulated (the results will be showed in chapter 4), and the simulation yielded $\tau_s = 1.72\ \mu s$. The bias frequency was therefore chosen as $f_{bias} = 17\ Hz$ to satisfy the requirement defined above and have a DC temperature component independent of the current frequency. This concerns the first hypothesis: in each cycle of excitation, the device is able to reach steady state.

About the second hypothesis, once it has been assured that the sample achieves steady state at each excitation cycle, one has to check that also the the tip does, for each point that is scanned during the line scan. There was no information available on the website of the manufacturer [50], but it has been reported for other thermoresistive Pd probes a time constant between 200 and 400 μs [20]. Taking $\tau_t = 400\ \mu s$ to have a conservative estimation, this means that one has to wait a time equal to $5\tau_t = 2\ ms$ to make sure that the tip reaches steady state: its temperature will not be the same as the one of the sample due to the heat transfer mechanisms discussed in section 2.3. For these thermomagnetic scans, the number of points per line has been set to 512, to have higher resolution. This

means that each line should take at least 1.024 s, which corresponds to a scan rate $SR = 1$ Hz. Therefore the minimum scan rate used in these scans has been 0.1 Hz.

Due to the lack of literature about EE in CMG, there were no references to understand what is the current required to observe the effect. Larger current would obviously yield larger temperature differences, due to the linear proportionality, but, on the other hand, they could damage the sample. Looking at other studies about EE in different materials (iron carbon alloys [51], and FePt [52]), the densities of current employed to analyse the effect vary from $6 * 10^5 A/m^2$ to $2 * 10^9 A/m^2$. With the cross section of our sample this translates in current ranging from tenths of μA to mA: indeed, this is the range of current that has been employed. Actually, using the LIA to supply the power, the voltage is set, and not the current: measuring the resistance of the channel ($R_{channel} = 13.6\,k\Omega$), this corresponds to a voltage varying from 1 V to 17 V. About the magnetic field, scans at large field have been performed in order to maximize the amplitude of the effect. On the other hand, the EE should be sensible to the magnetic structure of the sample, since regions with different magnetization orientation give temperature differences in different directions. Just as the Nernst thermovoltage follows the hysteresis curve (Figure 1.6a) the amplitude and phase maps of Sample 1 should provide a structure resembling the square domain structure observed in the MFM maps. For this reason, also scans at low field have been performed.

3.2.2 Sample 1

The results obtained for Sample 1 are showed in Figure 3.10 and 3.11b. For this sample, as explained above, the investigation was focused on small fields, so 10 and 20 mT, and a current of 700 μA (correspondent to 10 V), to look for square structure which resembled the one observed in the magnetic maps. For these maps, the scan direction has been changed, so that the channel appears horizontally instead of vertically like in the MFM maps. The scanned area is in between the second and third arm (Figure 3.3) like it has been done for MFM. The reason why most of the maps obtained in the thermomagnetic characterization are narrow strips resides in the aforementioned problem of the heating from the magnet together with the slow scan rate adopted for these experiments. At a scan rate of 0.1 Hz or lower, indeed, a map of 512 lines with 512 samples per line takes from 2 to 5 hours: oftentimes, the piezoelectric scanner reached its full extension way before that. In Figure 3.10a the topographic map of the area is displayed: in this case the tip has been shifted in the middle of the scan to check whether the lines observed in the amplitude maps followed as well. In all the maps a green mask is superposed: this corresponds to the channel borders, to have a reference of the channel. Figure 3.10b and 3.10c show the amplitude and phase images of the SThM demodulated at the first harmonic, so at f_{bias}: in the amplitude map a line pattern can be spotted close to the right border, which follows the shift of the channel. Unluckily, since SThM is particularly sensible to surface asperities and differences in thickness, it is hard to understand whether this line signal stems from the EE, or it is just SThM signal due to different thickness between sample and substrate. The phase signal, on the other hand, which should indicate the sign of the temperature difference is noisy and no patterns can be identified. In Figure 3.10d the map of the amplitude at the second harmonic is also showed, which is proportional to the Joule heating in the sample. In this case the auxiliary outputs of the LIA have been employed, allowing to demodulate a signal at different frequencies, using different channels. In this map, the only strong signal comes again from the right border of the channel, whereas little heating seems to be going on inside the channel. Nevertheless the shape of this pattern

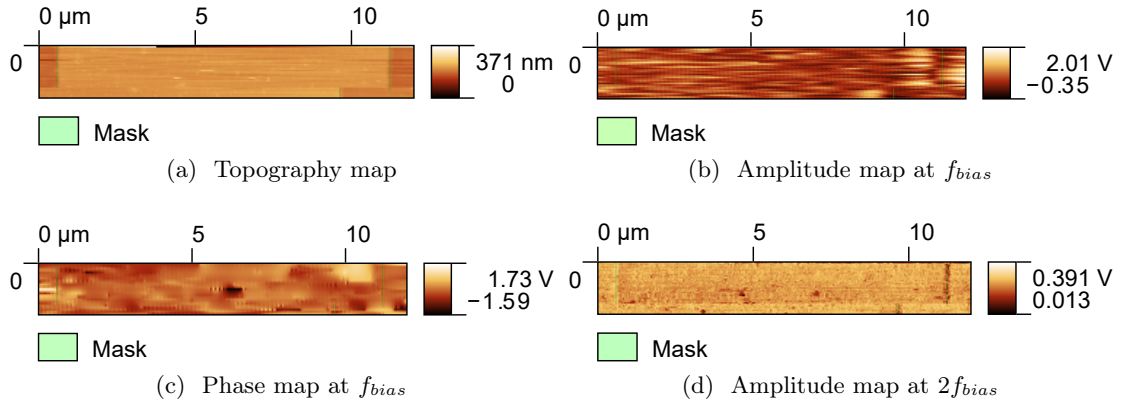

(a) Topography map (b) Amplitude map at f_{bias}

(c) Phase map at f_{bias} (d) Amplitude map at $2f_{bias}$

Figure 3.10: Thermomagnetic characterization of Sample 1 at $B = 10\ mT$, and $I = 700\ \mu A$: the topography, amplitude and phase at the first harmonic and amplitude at the second harmonic are showed, together with a green mask which represents the channel borders.

seems rather different from the one observed in the amplitude map, which is in addition not completely aligned to the right border.

The same experiment has been repeated keeping the current constant and raising the field to 20 mT. In this case the lines close to the border in Figure 3.11b are even clearer: the upper part of the map looks different due to a change of setting while scanning. On the contrary, also in this case the phase map is very noisy, and it is impossible to retrieve any information out of it. In the lateral friction map, instead, one can see that most of the Joule heating occurs inside the channel, with no lines close to its border. It is therefore possible to exclude that the lines observed in Figure 3.11b are correlated to Joule heating. To examine the possible correlation between amplitude maps at the first harmonic and topography maps, the Pearson coefficient has been computed for both the data sets, between these two types of maps: in both cases, however, the value was in between 0 and 0.1, suggesting no linear relation between the two maps.

3.2.3 Sample 2

For Sample 2, since no square domain structure has been observed at low field, the thermomagnetic characterization has been carried out directly at high fields, in order to maximize the amplitude of the EE. Also the current injected in the sample has been progressively increased: Figure 3.12, 3.13, and 3.14 show the maps obtained with $B = 350\,mT$ and 700 mT and the current being 70 μA, 420 μA and 1.24 mA, respectively. Just like for Sample 1, the topography maps, the phase and amplitude for the first harmonic, and the amplitude for the second harmonic (proportional to the Joule heating) are displayed, together with a green mask which represented the borders of the channel.

The main problem encountered for the characterization of Sample 2 was the heating of the magnet, which significantly affected the maximum time available to perform the scans before the piezoelectric scanner reached full retraction. Indeed the width of the maps is severely reduced, and it is possible only to examine a small part of the channel. In Figure 3.12 the maps obtained at $B = 350\,mT$ and $I = 70\,\mu A$ are showed: the results are similar to the ones obtained for Sample 1, meaning that line patterns in correspondence of the channel borders are visible in the amplitude map taken at the first harmonic, and

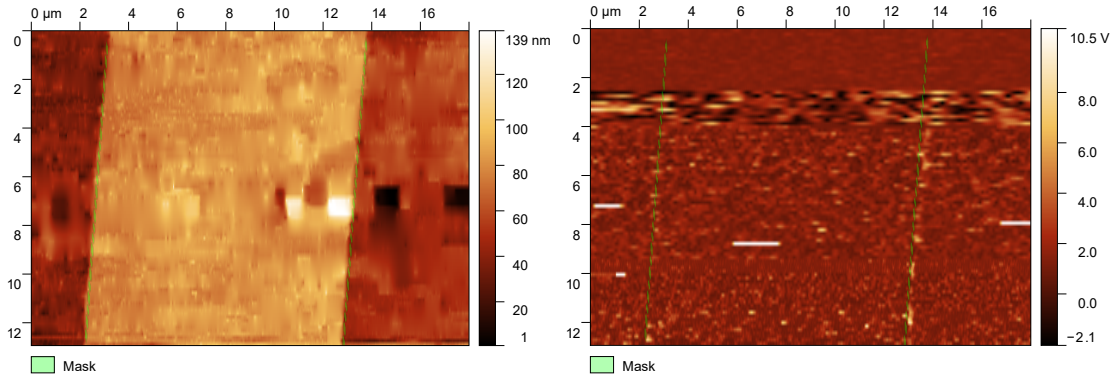

(a) Topography map

(b) Amplitude map at f_{bias}

(c) Phase map at f_{bias}

(d) Amplitude map at $2f_{bias}$

Figure 3.11: Thermomagnetic characterization of Sample 1 at $B = 20\ mT$, and $I = 700\ \mu A$: the topography, amplitude and phase at the first harmonic and amplitude at the second harmonic are showed, together with a green mask which represents the channel borders.

(a) Topography map

(b) Amplitude map at f_{bias}

(c) Phase map at f_{bias}

(d) Amplitude map at $2f_{bias}$

Figure 3.12: Thermomagnetic characterization of Sample 2 at $B = 350\ mT$, and $I = 70\ \mu A$: the topography, amplitude and phase at the first harmonic and amplitude at the second harmonic are showed, together with a green mask which represents the channel borders.

again the phase map provides little to no information at all. Looking at the amplitude map at $2f_{bias}$ it is possible to spot a larger intensity close to the borders, and a homogeneous heating occurring within the channel. The increase of the current to 420 μA did not significantly change the maps (Figure 3.13), with the main features discussed in Figure 3.12 present as well for larger current.

Raising the field and the current to the maximum values ($B = 700\,mT$, $I = 1.24\,mA$) the main discernible changes are in the amplitude map for first and second harmonic. In Figure 3.14b, indeed, as opposed to what was expected, the line signal coming from the border weakened considerably, either in size and in value. The phase map remains very noisy, whereas the second harmonic amplitude shows no line pattern close to the border, but heating occurring mostly within the channel, with a much higher intensity than in the previous cases, consistently with the larger current adopted. As for Sample 1, possible linear correlations have been investigated by computing the Pearson coefficient between the amplitude map at the first harmonic, and both the topography and the second harmonic amplitude map: in all cases, the value was smaller than 0.1, excluding any linear correlations.

3.3 Discussion

The discussion of the magnetic maps presented in section 3.1 strongly relies on the magnetic characterization data performed by collaborators at KUL. The initial declared goal was to observe how domains changed during the hysteresis curve, and, after the MFM scans on Sample 1, to look into the origin of the square domain structure.

Starting from the analysis of the square structure, it was already pointed out in section 3.1 how the appearance of these feature clashed with all the experimental evidences available: a clear signal is present at zero field, when the domains should relax in the IP direction, the one that will give no signal in the magnetic maps. However, by looking closely at the maps

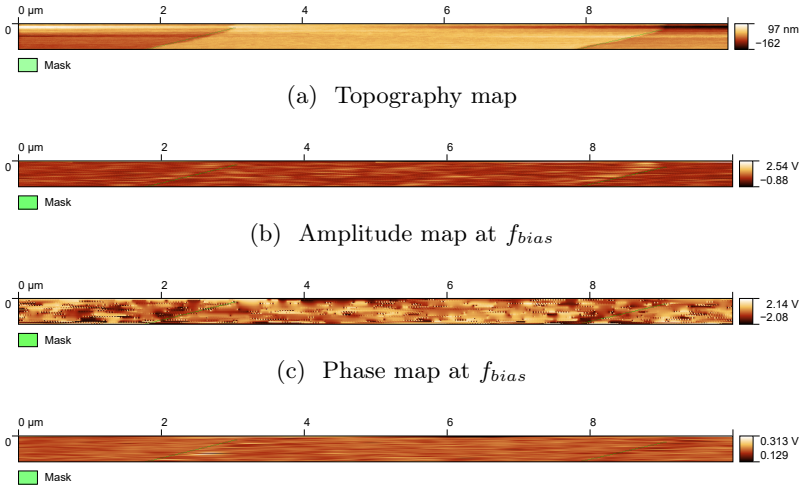

(a) Topography map

(b) Amplitude map at f_{bias}

(c) Phase map at f_{bias}

(d) Amplitude map at $2f_{bias}$

Figure 3.13: Thermomagnetic characterization of Sample 2 at $B = 350\ mT$, and $I = 420\ \mu A$: the topography, amplitude and phase at the first harmonic and amplitude at the second harmonic are showed, together with a green mask which represents the channel borders.

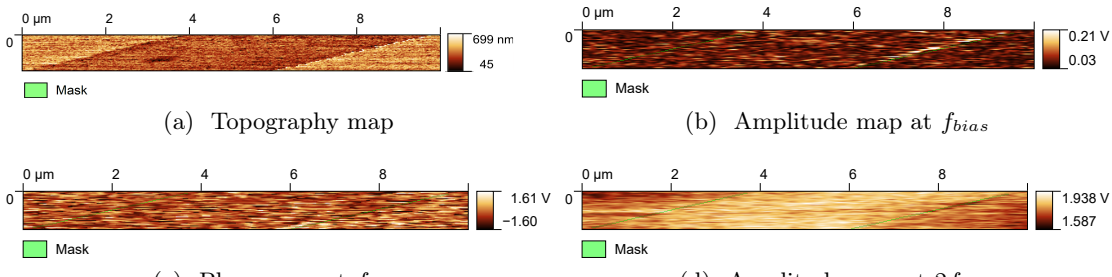

(a) Topography map

(b) Amplitude map at f_{bias}

(c) Phase map at f_{bias}

(d) Amplitude map at $2f_{bias}$

Figure 3.14: Thermomagnetic characterization of Sample 2 at $B = 700\ mT$, and $I = 1.24\ mA$: the topography, amplitude and phase at the first harmonic and amplitude at the second harmonic are showed, together with a green mask which represents the channel borders.

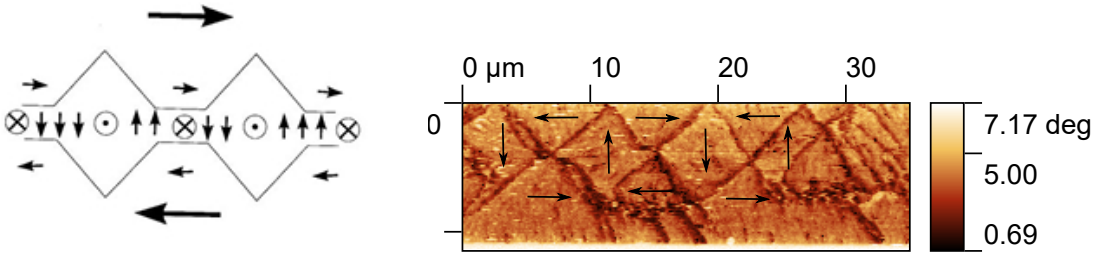

(a) (b)

Figure 3.15: a): Sketch of a cross-tie domain wall, with the black arrows being the magnetization, the circles are Bloch lines [22]. b): Magnetic phase map for Sample 1 at $B = 8\,mT$, with the possible magnetization direction of domains in black.

of Figure 3.4, one can recognize the structure of cross-tie domains (Figure 3.15a): these are particular domain wall which form in thin magnetic films with in-plane anisotropy, like CMG. Thin magnetic films are defined as the ones whose thickness is smaller than the width of the films: the width of the walls can be estimated in the order of 500 nm, ten times larger than the thickness of the film, defining the CMG films as magnetically thin. A cross-tie wall is formed by replacing 180° Neel walls with 90 ° walls, which provide a smaller energy for a thin magnetic film with in-plane anisotropy and magnetic field perpendicular to the easy axis [53]. Within this context, the possible magnetization direction of the domains observed in Figure 3.4c could be the one depicted in Figure 3.15b: in this way, one would also have closure domains close to the border which, as explained in section 1.3, reduce the magnetostatic energy.

However, these domains are magnetized IP: the tip is magnetized OOP, and for what has been said up to now, there should be no signal. This is indeed true for the most common domain structures, since they give a 2D stray field which remains IP if the magnetization is IP. Cross-tie domains are more complicated than this, and constitute the exception to this rule: in thin films, cross-tie domains create a three-dimensional stray field, meaning that, even if the magnetization is IP, the stray field above the sample can still be OOP [53]. This is the mechanism through which these IP oriented domains can be detected via a OOP magnetised tip. One can now reason about the behaviour of these domain walls when the magnetic field is increased: looking at Figure 3.16a one can see that, among the IP orientation, the [100] direction is harder with respect to the [110]. In addition, observing the evolution of the features in the maps it is clear that, with respect to the structure of Figure 3.15b, the walls in the direction bottom left - top right disappear, and, among the domains that survive, there is a class of domains expanding, and another shrinking. This is particularly clear in Figure 3.4g, where one can see a group of domains reduced to transversal stripes and sandwiched in between the adjacent two. The domains expanding could therefore be the ones oriented in the easiest of the IP directions, so [110], which implies a 45° rotation with respect to the initial orientations, whereas the shrunk ones could be oriented in the [100] direction. This is represented in Figure 3.16b. Then, as the field keeps increasing, the domains will all orient in the [110] direction, with these ones growing more and more until there is no longer contrast (Figure 3.4i). If for fields lower than 120 mT the domains have been oriented in the easiest of the IP directions, then, as the field raises, they will tilt toward the direction of the applied field. In the maps of Figure 3.5, indeed contrast can still be observed, and this will indeed correspond to the [110] oriented domains rotating toward the OOP orientation, more and more as the field

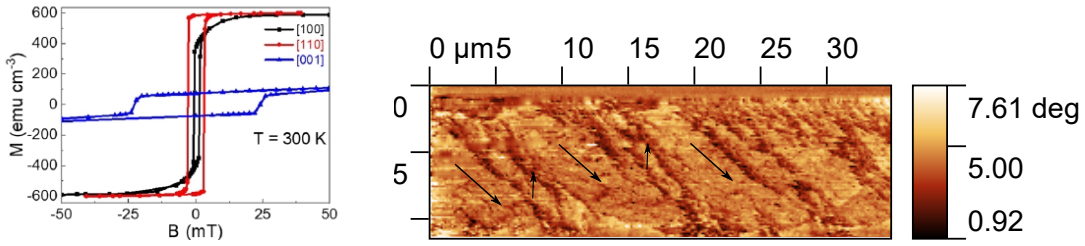

(a) (b)

Figure 3.16: a): Hysteresis curve in the IP direction (black and red curve) and OOP direction (blue one) [21]. b): Magnetic phase map for Sample 1 at $B = 42\,mT$, with possible magnetization orientations in black.

increases.

One point has still to be discussed: why this structure appears only in Sample 1, and not in Sample 2 and 3. First of all, from the structural characterization performed, it is possible to exclude that the patterns followed the grain boundaries, since the grain size has been estimated in the ballpark of nm by KUL collaborators, whereas the size of the pattern is in the μm range. It is clear that this is a mechanism involving either the oxide layer formed on Sample 1, which could have affected the magnetic structure, or the capping layer of Sample 2 and 3, which similarly could have destroyed this domain structure. The main hypothesis are indeed two. The first one concerns the oxidation layer of Sample 1: the oxide may have promoted this kind of domain formation by generating, at the interface sample - oxide, regions of slightly different composition, which have different magnetizations and magnetic properties [25]. It has been showed, indeed, how these off-stochiometric compounds display magnetic properties significantly different from stochiometric CMG. Another possible explanation could involve the deposition method employed for the Ta capping layer, which is magnetron sputtering deposition. It has been showed ([54, 55]) that this deposition method and the parameters employed during the deposition can affect the magnetic properties and structure of the film deposited. The deposition of the Ta atoms by sputtering could also affect the magnetic structure of the sample underneath, destroying the domains observed in Sample 1.

For what concerns the thermomagnetic characterization and the EE, the results obtained do not significantly point in one direction or the other. As explained above, in the amplitude maps at f_{bias} displayed there is a consistent line pattern showing up at the borders of the channel, which is consistent with what is expected (at high fields), meaning a gradient of temperature developing across the width of the channel. On the other hand, oftentimes this pattern is present on just one side of the channel, whereas the amplitude signal should be symmetric, since it represents the module of the temperature difference developed. In addition, in all the experiments discussed in section 3.2 the phase maps are always very noisy and no pattern can be identified, when one instead would expect a signal which is odd with respect to the y coordinate in the channel and proportional to the sign of ΔT. This large noise in the phase maps is probably due to intrinsic noise of the setup, which, as for the magnetic features, masks the observable features. For Sample 2, since no square magnetic structure was observed, the expectation was indeed to observe this type of line pattern.

Moving to Sample 1, instead, as mentioned in the beginning, was to observe something resembling the square structure, since the initial hypothesis was that these were OOP

domains. After a more detailed analysis, these turned out to be cross-tie IP domains: this means that the direction of the temperature gradient is not the expected one (along y). Indeed, assuming as the domain orientations the ones drawn in Figure 3.15b, then the closure domains will give no temperature difference, since $\boldsymbol{M} \parallel \boldsymbol{I}$, so the cross product is null. For the central domains, however, the two quantities are perpendicular, therefore a temperature gradient should develop along z, in the OOP direction, and it should also change sign from square to square. Unfortunately, no brighter signal is observed in the center of the channel in the amplitude maps of Figure 3.10b and 3.11b.

What could help in interpreting the maps would be estimating the amplitude of the EE: a very possible hypothesis, indeed, is that the effect is just too weak to be detected by SThM, meaning that the temperature difference is smaller than the temperature resolution of the technique. In this case, the signal picked up in the maps would come just from the difference in thickness when the tip moves over the sample to the substrate. From literature on different materials, ([6, 51, 52]), indeed, the magnitude of the effect seems to be in the range of the mK: depending on the probe used, this is close to the resolution limit of many SThM setups ([20]). This point will be further detailed in chapter 4.

In all the maps presented in the previous section, the amplitude at the first and second harmonic have been presented in V. Clearly, to be able to draw any quantitative conclusion or analysis, they have to be converted in temperature units: however, given the quality of the data and the uncertainty about the origin of the features, it was decided to keep the data in V to focus on qualitative conclusions. The calibration process to convert them in temperature units will however be explained. The first step consists in relating the power applied to the probe to the excess temperature generated: this is done by applying different powers to the probe, and checking how the resistance varies, as displayed in Figure 3.17a. Then, by knowing the relation between resistance and temperature (Figure 3.17b), it is possible to relate applied power to probe temperature T_{probe}. As detailed in section 2.3, however, this is the probe temperature, which will be different from the one of the sample: the two are related by the following equation [56]:

$$T_{sample} = T_{probe} \frac{\Delta V_{AC}}{\Delta V_{AC} - \Delta V_{DC}}, \tag{3.3}$$

where ΔV_{AC} will be the voltage recorded at the first or second harmonic for the EE or Joule heating, respectively, and ΔV_{DC} the DC component of the SThM signal (not showed in the maps), which corresponds to the DC component of the sample temperature identified in Equation 3.1.

Another point to remark is that, unlike for the magnetic characterization, the presence of the capping layer does not affect the results obtained: this means that the oxidation of Sample 1 does not play a role in the EE or in its measurement. What can furthermore be done to gain more insight in the origin of the line patterns is to examine how they vary when the magnetic field and current are changed. As discussed in section 1.4, the amplitude of the effect is directly proportional to the magnetization and electric current, therefore the amplitude voltage signal at the first harmonic should reflect this relationship. This analysis is reported in Table 3.2: in this case, for each line pattern identified in the amplitude map at f_{bias}, the profile of the signal along that line has been extracted and then the average computed. It is also useful to remember that, in this range of the hysteresis, the relationship between magnetization and field is monotonic, so if the latter increases, the former does as well. If the line patterns were present in the same map at both borders, the average between them has been considered. Looking at Sample 1, the signal indeed increases when the field is doubled and the current stays constant: the increase does not

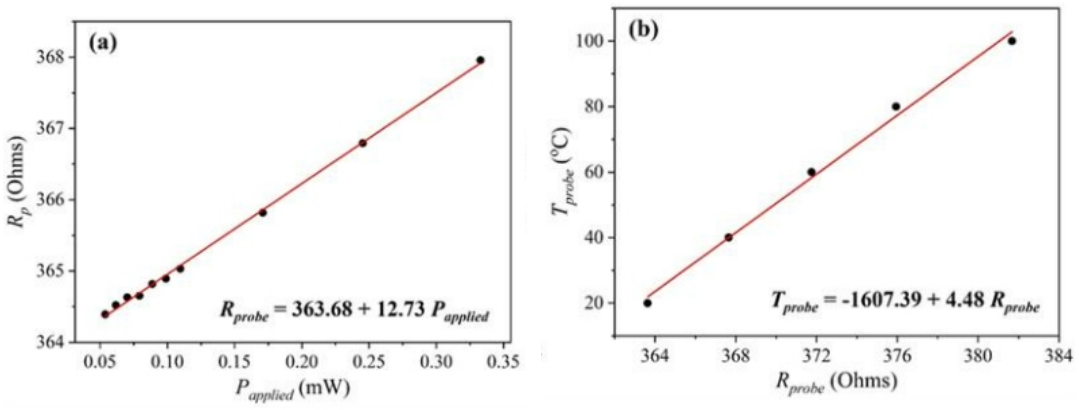

(a) (b)

Figure 3.17: a): Curve probe resistance against applied power and linear fit. b): Curve probe temperature against probe resistance and linear fit. Both curves have been obtained by a collaborator on a different SThM setup and reproduced with permission.

Sample 1		**Sample 2**	
Magnetic field and current	Average signal $[V]$	Magnetic field and current	Average signal $[V]$
$\boldsymbol{B = 10\,mT}$ $\boldsymbol{I = 700\,\mu A}$	1.059	$\boldsymbol{B = 350\,mT}$ $\boldsymbol{I = 70\,\mu A}$	0.775
$\boldsymbol{B = 20\,mT}$ $\boldsymbol{I = 700\,\mu A}$	2.939	$\boldsymbol{B = 350\,mT}$ $\boldsymbol{I = 420\,\mu A}$	1.094
		$\boldsymbol{B = 700\,mT}$ $\boldsymbol{I = 1.24\,mA}$	0.14

Table 3.2: Average signal along the line patterns in the amplitude map at f_{bias}, for the different maps recorded for Sample 1 and 2.

mirror the increase in field, but this is expected considering that the relevant quantity is the magnetization, which is not linear with the magnetic field. For Sample 2 as well the signal increases when the current is raised, and the field is kept constant at 350 mT. The most concerning feature of the whole table however involves the measurement taken at the maximum field and current, which yields the smallest average signal of the set. Even assuming that the magnetization is already saturated at 350 mT, which has been proved wrong, the signal should anyway increase thanks to the larger current flowing, and this is clearly not the case.

Chapter 4

Simulations

In this chapter the COMSOL simulations performed concerning the setup of the experiments will be presented. Three simulations have been performed: the first one regarded the magnetic field created by the magnetic tip of the MFM when its magnetization is saturated; the second one was designed to calculate the thermal time constant of the sample to investigate its thermal behaviour when excited with an electric current; in the third one an attempt was made to estimate the amplitude of the EE with respect to Joule heating in the sample. Within this context, the first and third simulation were performed to help in the interpretation of the experimental data, the second one to obtain an experimental parameter relevant for the frequency of the electric current. In all the simulations performed, the version 5.0 of COMSOL has been used.

4.1 Magnetic field induced by the tip

In this simulation the main goal was to obtain the magnetic field produced by the magnetic tip when magnetized at saturation, at a distance equal to the lift height. The purpose is indeed to exclude the possibility of the tip magnetically writing on the sample, meaning changing the magnetic structure of CMG thanks to its magnetic field, given also the reported small value for the coercive field of CMG. This hypothesis was concerning in particular for Sample 1, which, as discussed, displayed indeed line features in the magnetic maps.

The simulations was arranged as follows: the tip has been built as a truncated cone, with an half sphere at its end whose radius is the tip radius r. The whole structure has been coated with a magnetic coating of thickness t: a picture of the modeled geometry is provided in Figure 4.1. Also an air box of 1 x 1 x 1 mm^3 has been included. All the data regarding the dimensions of the tip are summarised in Table 4.1, and taken from the website of the manufacturer [45]. The only data unavailable for the tips employed in the experiment was the thickness of the magnetic coating t: for this reason, this parameter has been swept in the simulation, based on data available for probes provided by different manufacturers [57, 58]. The core of the probe has been modeled as Silicon, whereas the magnetic coating as CoCr.

The physics employed has been "Magnetic Field, No Current", active only on the magnetic coating domain: this physics comes along with three default boundary conditions. The first one is "Magnetic Insulation", which sets at zero the tangential component of the magnetic field on the selected boundaries. This condition has been enabled on the internal and external boundaries of the magnetic coating domain. The second one is "Initial Values", which allows to set a non-zero initial value of the magnetic scalar potential in the domains

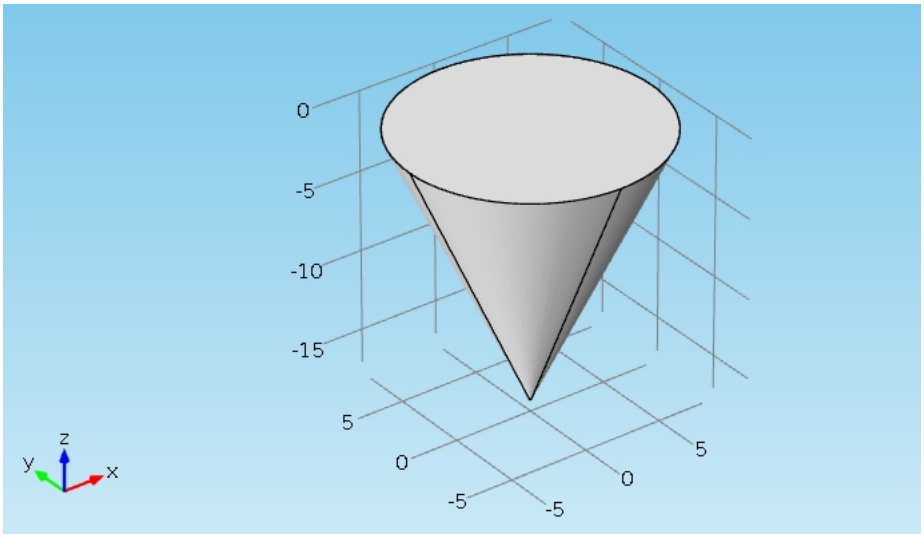

Figure 4.1: Picture of the geometry modeled in the tip magnetic field simulation. The external surface showed in the picture is the magnetic coating.

of choice: in this case, it has been kept to zero for all the domains involved. The last condition is "Magnetic Flux Conservation", which defines the pressure, temperature and the constitutive relation for the material, defining either the relative permeability, the BH curve, or the magnetization of the material. In this case, the temperature and pressure have been kept at ambient values (293 K, 1 atm), whereas the magnetization of the magnetic coating has been fixed, as a uniform magnetization M parallel to $-z$. The module of this magnetization has been obtained as $M = \frac{m}{V}$, where V is the volume of the magnetic coating, obtained from the values of Table 4.1. This corresponds to $M = 11.699\, A/m$.

The geometry has been meshed with a finer mesh, made of 297205 elements, mostly tetrahedral and triangular. The study conducted was stationary, sweeping the magnetic coating thickness t from 20 to 60 nm, at steps of 10 nm. The study computes the magnetic field in all the space: since the quantity of interest was the field induced by the tip on the sample, the field has been computed along a line parallel to the axis of the tip. In Figure 4.2 the magnetic field has been plotted for all the coating thicknesses adopted against the distance from the tip along the vertical direction. The selected range of distances spanned across the range of lift heights used in the experiment: as it can be seen, for all the thicknesses, the magnetic field is extremely low, in the range of tenths of mT. At a distance of 80 nm, which has been the lift height used in most of the experiments, the field ranges between 1 and 2 μT, with the largest values associated to the largest thicknesses. It is therefore possible to exclude that the tip had any influence on the magnetic structure of the sample, so that a possible tip origin for the features of Sample 1 can be ruled out.

4.2 Transverse thermal time constant

This simulation, like the one described in section 4.3, concerns the second part of the experiments, the thermomagnetic characterization. In particular, the goal of this simulation is to retrieve the thermal time constant of the Hall bar, to set the frequency of the electric current, so that at each cycle, the sample is able to reach steady state. The thermal time constant is defined as the time the object (the Hall bar, in this case) takes to reach 63.2 % of its final temperature difference. In this case, however, since the temperature difference

Parameter	Symbol	Value
Tip height	h	17 μm
Half-cone angle	θ	25°
End radius	r	30 nm
Thickness of magnetic coating	t	20 - 60 nm
Magnetic moment	m	10^{-16} Am^2

Table 4.1: Parameters employed in the tip magnetic field simulation. The magnetic coating thickness has been swept from 20 to 60 nm at steps of 10 nm.

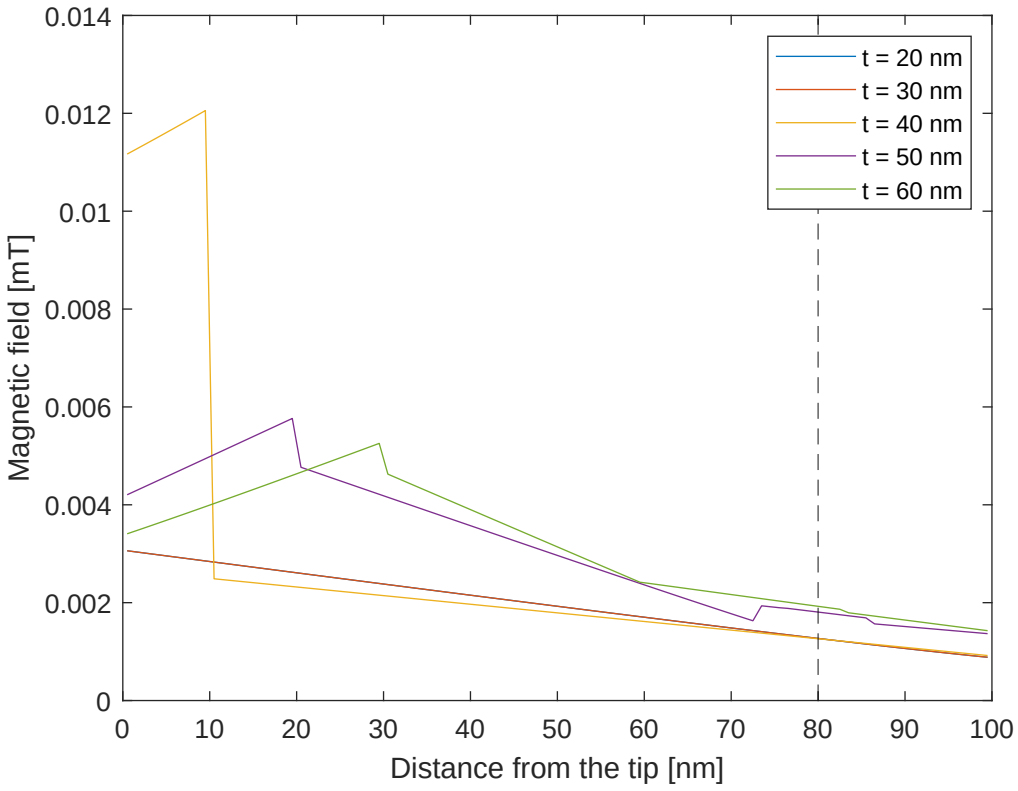

Figure 4.2: Magnetic field against distance from the tip along its axis, for different magnetic coating thicknesses. In dotted black the lift height used for most of the experiments.

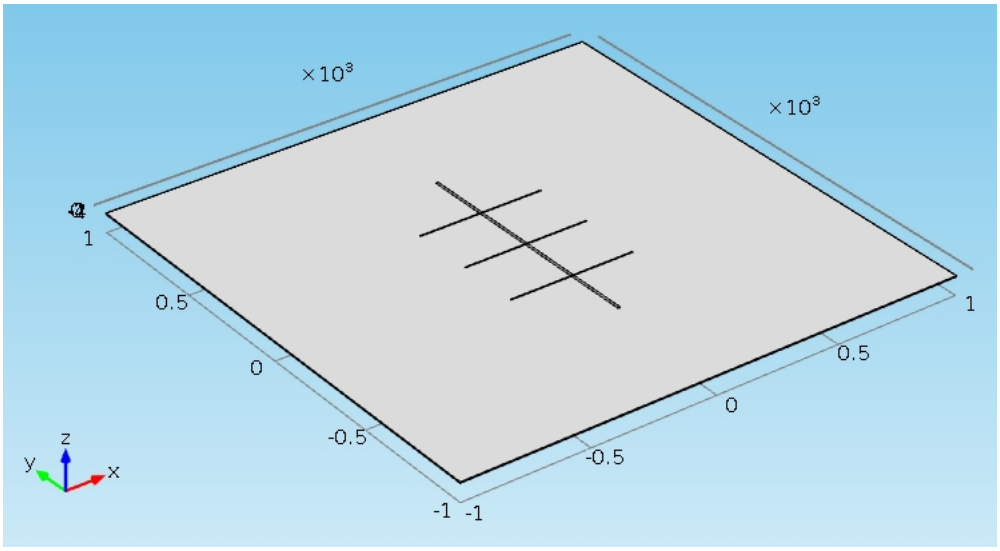

Figure 4.3: Picture of the geometry modeled in the thermal time constant simulation.

Parameter	Symbol	Value
Channel length	l_{chan}	1 mm
Channel width	w_{chan}	10 μm
Sample thickness	t_{CMG}	50 nm
Arms length	l_{arms}	500 μm
Film side length	l_{sub}	2 mm
Substrate thickness	t_{sub}	5 μm
Channel resistance	R_{chan}	13.6 $k\Omega$
CMG thermal conductivity	k_{CMG}	20 W/mK
CMG heat capacity at constant pressure	$C_{p_{CMG}}$	1090 J/kgK
CMG density	ρ_{CMG}	8390 kg/m^3

Table 4.2: Parameters employed in the thermal time constant simulation.

of interest will develop across the width of the bar, the simulations focuses on the time it takes for the sample to thermalize from one side of the channel to the other, from which the name transverse thermal time constant.

The geometry of the sample and the substrate has been modeled as showed in Figure 4.3: the dimensions of the Hall bar are the same as the real device, but the ones of the film have been scaled down by a factor 5, to reduce the computation time. This scaling down does not prevent however from considering the substrate as bulk, and does not affect the results of the simulation. All the dimensions are listed in Table 4.2. The material chosen for the substrate has been MgO, along the $< 100 >$ axis, which is already present in COMSOL. On the other hand, CMG does not belong to the material library of COMSOL, therefore its properties had to be inserted by hand. Since this simulation concerns heat transfer, the only parameters COMSOL required to solve the problem were thermal conductivity, density and heat capacity at constant pressure. These parameters have been taken from [23], and are listed in Table 4.2.

The physics adopted for this simulation has been "Heat Transfer in Solids", with all the domains included in this module: this one, like the magnetic field one, includes three domain conditions which have not been changed. The first one is "Heat Transfer in Solids":

its purpose is to set temperature, pressure, density, thermal conductivity, and heat capacity at constant pressure for the domains involved, so that one can select different properties within the same material. For this simulation, external temperature and pressure have been kept at ambient conditions, and the quantities aforementioned have been taken from the list of properties in the material tree. The second condition is "Initial Values", which allows to set an initial temperature different from the ambient one for one of the domains involved. The initial temperature has been kept at 293.15 C°. The last default condition is thermal insulation: this means, that, across the selected boundaries, there is no heat flux, so there are indeed thermally insulated. This condition has been applied in all the exterior boundaries: the only boundaries for which it has been disabled were the ones between the sample and substrate, to allow heat dissipation from the sample toward the substrate.

Beside these default conditions, two more have been added to correctly describe the problem: the first one is a temperature boundary condition which fixes the temperature at a desired value during all the simulation. In particular, the back side of the film has been kept at ambient temperature: this acts effectively as a heat sink and has been done to ensure a correct thermalization of the sample. Without any mechanism of heat dissipation toward the ambient or toward an heat sink, in presence of a heat source, the temperature of the device will only increase linearly with time. The second condition added is a boundary heat source: this has been applied on the boundaries on one side of the channel, so that the temperature has been then recorded on the opposite side to understand how long it takes for thermalization. The heat source has been calculated as $Q = R_{chan}I^2$, with I electric current injected in the sample during the experiments, which corresponds to the Joule heating generated: the value of the heat source however only affects the final temperature reached, not the time constant. The smallest and largest currents used (70 μA and 1.24 mA) give rise to input heat sources of 67 μW and 21 mW, respectively. Indeed, the different currents used in the experiments have been used to vary the input heat, but the thermal time constant has remained the same.

Since the dimensions of the bar in the simulation are much smaller than the ones of the film, two different mesh types have been used: for the bar, a mesh swept has been performed, from the top face toward the bottom face. The rest of the geometry has been meshed with a free tetrahedral mesh: in this way the bar can be more refined due to its smaller features, whereas the film can be modeled with a coarser structure. Since the behaviour of temperature with time was the quantity of interest, a time-dependent study has been performed: after some trial and error, the correct time range to observe thermalization was identified to be 6 μs. As specified above, the temperature of the other side of the channel has been recorded, and the time trend is depicted in Figure 4.4a: the temperature increase stabilizes after circa 4 μs. The temperature decrease in the beginning of the simulation is due to instabilities at the beginning of the simulations, when the program has to compute the solution for $t = 0$. In the graph the horizontal line marks an increase of 63.2 % is marked: the time it takes to achieve this temperature increase is the thermal time constant (vertical dotted line), which results to be $\tau = 1.72\,\mu s$. Also the spatial distribution of the temperature within the channel has been reported in Figure 4.4b, for $t = 4\,\mu s$: in this case, the temperature increase has almost stabilized, with a minimum close to the opposite border. The maximum temperature remains the one where heat has been injected: a parabolic trend can be identified, with the opposite end that stabilizes at a lower temperature, setting a finite temperature difference after the transient behaviour.

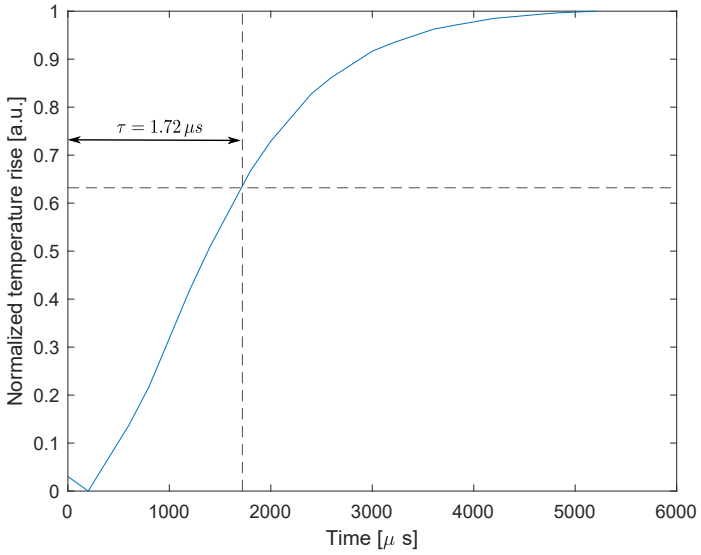

(a)

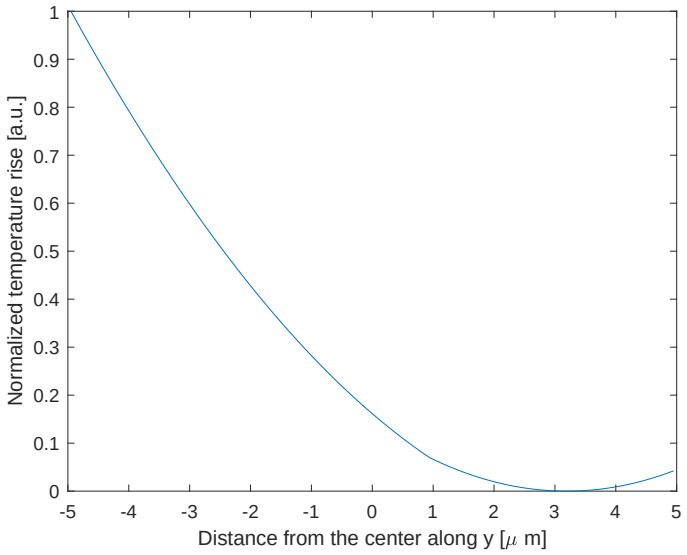

(b)

Figure 4.4: a): Normalized temperature rise at the other end of the against time. The horizontal black dotted line corresponds to an increase of 0.632, the vertical one is the correspondent time. b): Normalized temperature rise against the position in the channel at $t = 4\mu s$. The negative y correspond to the side where heat has been injected, the positive ones to the side where temperature is recorded.

4.3 Amplitude of the heating mechanisms

In this third simulation the goal was to estimate the different heating mechanism involved in the EE experiments: Joule heating and EE, and compare them with the usual resolution of a SThM setup. The AC Joule heating has been simulated in COMSOL, whereas for the EE this was not possible, since this effect has not been included yet in the software. The amplitude of the effect will be therefore estimated via the Bridgman relation [59]:

$$P_{EE} = \frac{TN_{NE}}{k}. \tag{4.1}$$

This relation connects the Ettingshausen coefficient P_{EE} with the Nernst coefficient N_{NE} in $[V/TK]$ through the temperature and thermal conductivity.

The geometry used for the Joule heating simulation is exactly the same as the one employed for the thermal time constant. with the dimensions summarised in Table 4.2, and the geometry showed in Figure 4.3. In this case, however, beside the "Heat Transfer in Solids" module, also the "Electric Current" one has been employed, to model the current injected in the channel, and retrieve the heating due to the Joule effect. The conditions enabled in the heat transfer module are the ones described in section 4.2, except the "Heat Source" which has been disabled since the Joule heating will be calculated by another node. The "Electric Current" module has been enabled only for the domains belonging to the Hall bar, and it comes with three default conditions. The first one is "Current Conservation", which, just as the condition "Heat Transfer in Solids", defines temperature, pressure, conductivity and relative permittivity, which have been taken from the materials' properties. The second condition is "Electric Insulation", which zeroes the electric current flowing into the selected boundary: this has been enabled on the exterior boundaries of the Hall bar. Finally, the last default condition is "Initial Values": this allows to set an initial value of the voltage, which has been however set to zero. The two extra conditions adopted have been "Terminal", which fixes a fixed current or voltage on one boundary, and "Ground", which keeps the selected boundary at 0 V. The terminal has been positioned at the end of the channel, and the ground at the other end, to make sure the current flows within the channel. The four currents used in the experiment have been used as input for this simulation. To join the two modules, the Multiphysics node has been used, and in particular the "Electromagnetic Heat Source" condition, which takes as input the electromagnetic module and the heat transfer module.

The geometry has been meshed in the same way as the time constant simulation, but a frequency-stationary study has been adopted, in order to have an AC current flowing through the sample. For this study, the frequency has been set to 17 Hz, the one used in the experiments. An example of the temperature map obtained is displayed in Figure 4.5: in this case, the data have been plotted along a cross section parallel to the film, and cutting through the bar. The temperature profile is parabolic, with the heating concentrated in the channel, and the arms still at ambient temperature. The results are summarised in the third column of Table 4.3, showing that, as expected, the heating increases with the current injected.

The next point is now to estimate the temperature difference obtained due to the EE thanks to the Bridgman relation (Equation 4.1). The temperature has been considered as 293.15 K due to the negligible effect of the Joule heating, whereas the thermal conductivity has been taken as 20 W/mK. About the Nernst coefficient, many values are reported among literature: from [26], looking at the linear relationship between the Nernst thermopower in $[\mu V/K]$ and the field, the Nernst coefficient can be evaluated as $N_{NE} = 3\,\mu V/TK$.

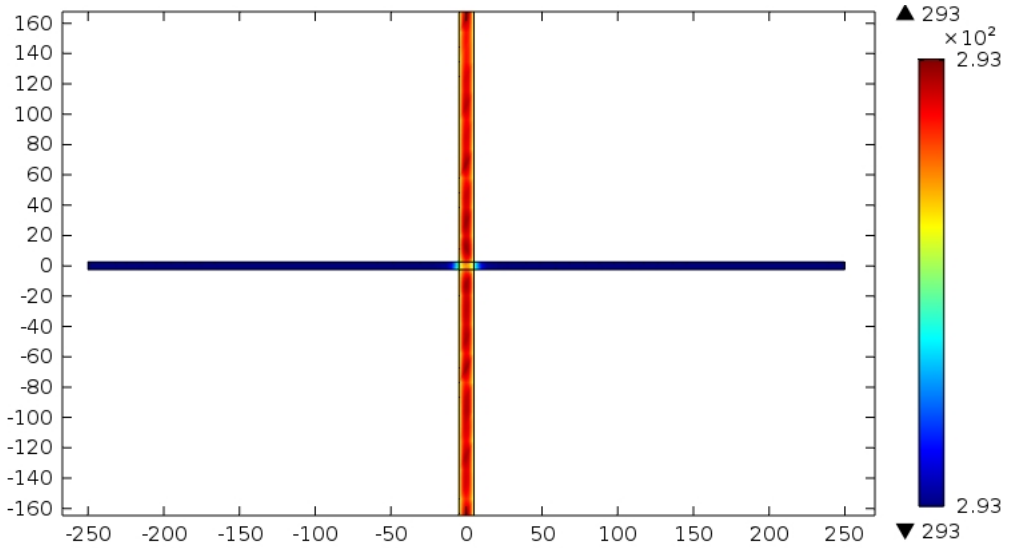

Figure 4.5: Picture of the 2D temperature map induced by Joule heating in the sample, with $I = 1.24\,mA$. The arm visible in the map is the central one.

Joule heating			**EE**	
Electric current I_{el} $[\mu A]$	**Heat source Q $[mW]$**	**Temperature difference ΔT $[mK]$**	**Magnetic field B $[mT]$**	**Temperature difference ΔT $[mK]$**
70	0.067	0.4	350	2.1
420	2.4	14	350	129
700	6.7 6.7	39 39	10 20	6 12
1.24*10^3	21	122	700	762

Table 4.3: Temperature increase owing to the Joule heating with different currents, from the simulation, and from the EE with different currents and magnetic field, computed thanks to the Bridgman relation. Only the combination of electric currents and magnetic fields employed in the experiments have been reported in the table.

This gives an Ettingshausen coefficient of $P_{EE} = 4.39 * 10^{-5}\, Km/TA$. Now, looking at Equation 1.4, one can retrieve the gradient of temperature generated with a certain current density and magnetization, and, multiplying by the width of the channel, the temperature difference ΔT is retrieved. The values of magnetization correspondent to the magnetic fields employed have been retrieved from the experimental hysteresis curves. This gives the values collected in the last column of Table 4.3. A further step that can be taken is to calculate the EE temperature difference for all the combinations of fields and current used in the experiments: this is represented in Figure 4.6, in which the temperature difference is plotted against the current for different fields, together with the Joule-induced temperature difference.

The first remark is that, as expected, the Joule-induced temperature difference shows a different dependence with respect to the EE-induced temperature difference: this is consistent with the Joule heating being proportional to the square of the current, and the EE being linearly proportional to the current density. The significant feature emerging from the plot however is that the Joule heating is larger than the EE-induced temperature difference just for low fields, and for large currents, since the Joule effect scales with the current quicker than the EE. In addition, for large fields, the Bridgman relation predicts a much larger temperature difference for the EE than for the Joule effect, and a ΔT approaching even 1 K for maximum field and current.

The data about the thermal resolution of thermoresistive SThM probes are conflicting, and varying from 100 mK, reported from many manufacturers ([60, 61]) to 500 mK, reported for a Pt/Rh thermoresistive probe [20]. For the probe used in the experiment no data is available. Considering a thermal resolution limit of 100 mK, most of the calculated and simulated temperature differences would actually be below the resolution of the instrument. However, the EE-induced temperature difference calculated from the Bridgman relation at maximum field and current ($\Delta T = 0.52\, K$) will probably be above the resolution limits of standard SThM setups, therefore it should actually be distinguishable in the maps. This analysis, therefore, on one hand, leads to a potential skepticism about the origin of the line features in Sample 1 for low field, since the predicted temperature difference is practically below 10 mK for all currents; on the other hand, it shines light on the maps performed at maximum field and current, which appear to be within the measurable range of typical SThM setups. One could actually deduce that the features observed in the maps of Sample 1 are likely to have a topographic origin, whereas the maps of Figure 3.14 for Sample 2, at $B = 700\, mT$ and $I = 1.24\, mA$ could effectively point toward a possible presence of the EE. In addition, the magnetization with this field is not at saturation, so it could be possible to increase the signal even more by increasing the field and saturating the sample.

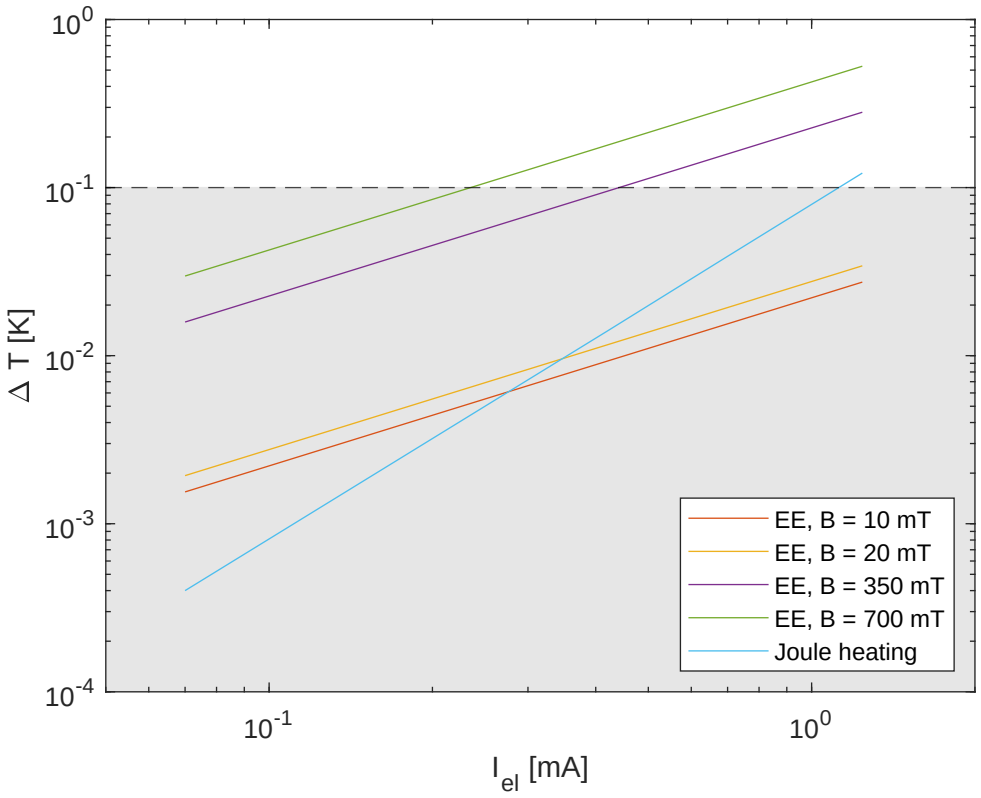

Figure 4.6: Log-log plot of the temperature difference against the injected current due to the Joule heating (from the simulation) and due to the EE, with different fields (from the Bridgman relation). The gray region indicates the data that could be below the resolution limit of SThM.

Conclusions and future work

With the advancement of research in quantum computing, many new qubit platforms are being discovered. However, most of them still require cryogenic temperatures to operate, and therefore sub Kelvin refrigerators. Also other applications like particle detectors, and in particular photon detectors, can only operate at temperatures close to the absolute zero. Nowadays, these refrigerators rely on Helium, which is economically very costly, and requires complex architectures for handling and recycling. This work is located within this context, with the purpose of analysing a new charge-to-heat conversion effect, the Ettingshausen Effect, which could be employed in the aforementioned applications, avoiding the employment of Helium, and boosting cryogenic technology.

Theoretical calculations have proved that the singularity of the Berry phase generates a huge boost for the heat-to-charge conversion coefficients, either the Ettingshausen and Nernst coefficient. In Weyl magnetic semimetals, the Berry phase is singular at the Weyl point, the intersection between the valence and conduction band, which disperse linearly in the vicinity of this point. Up to date, however, no experimental confirmation of this thesis has been reported, and indeed the aim of the present work has been to examine the Ettingshausen Effect in Co_2MnGa, and to correlate it with its magnetic structure.

To this end, three samples have been analysed: one uncapped Hall bar, one Hall bar with a Ta capping layer, and a thin film of Co_2MnGa with the capping layer. The hysteresis curve has been retrieved by collaborators at KUL for the capped and uncapped samples, revealing a small hysteresis cycle, and coercive field in the order of 8 and 30 mT, respectively. The magnetic structure has been probed via MFM, whereas the presence of the Ettingshausen Effect has been investigated via SThM, demodulating the signal to separate it from the Joule heating.

The magnetic structure has been probed by magnetising the samples to negative field, and then increasing it progressively: the uncapped Hall bar has revealed a surprisingly precise square domain structure, present only up to 120 mT, and disappearing when the field was increased. On the other hand, the capped samples, either the bar and the film, did not display any such structure, revealing an uniform magnetization in the magnetic maps. The probed domains in the uncapped Hall bar resulted to be cross-tie in-plane oriented domains, picked up by the tip, even if magnetized out-of-plane, thanks to the three dimensional stray field generated by the domains. The possibility of the tip altering the magnetic structure of the sample has been ruled out thanks to a simulation of the setup employed. The possible mechanisms through which such domains appear only in the oxidised sample could concern either the capping layer of the capped samples, whose sputtering deposition technique could destroy the magnetic structure, or the oxide layer, which could generate composition inhomogeneities, and regions with different magnetic properties.

The Ettingshausen Effect has been investigated in the capped and uncapped Hall bar, since this geometry is optimized to enhance the temperature difference. The experimental

conditions have been varied, probing the sample either at low and high magnetic fields, and also tuning the AC electric current from tenths of μA to the range of mA. In all the experiments, the amplitude maps demodulated at the first harmonic, proportional to the amplitude of the temperature difference, display two line features correspondent to the border of the channel. These features could coincide with the expected effect in the case of the capped bar, whereas one would expect an out-of-plane temperature difference in the center of the channel in the uncapped bar. On the other hand, the phase maps, which should be proportional to the difference of the temperature gradient, are featureless, probably due to large noise coming from the instrument. The amplitude of these features has been confronted with the magnetic field and current applied, finding out that the signal detected does not scale as expected, with the smallest signal associated to the largest current and field.

These data have been supported by a simulation of the Joule heating in the device, and by calculations of the expected amplitude of the Ettingshausen Effect via the Bridgman relation. This confront has revealed that the amplitude of the Ettingshausen Effect, in the range of electric current used, is larger than the Joule effect when the magnetic field is 350 and 700 mT. Moreover, considering the usual resolution of a SThM setup, most of the expected values for the temperature difference generated by the Ettingshausen Effect fall below or across this resolution limit, generating serious doubts about the possibility of SThM to observe this effect with these experimental parameters. Only with maximum field and current, a temperature difference approaching 1 K could be generated, large enough to be detected.

With the present data, there are not enough evidences to conclude that the observed features come from the Ettingshausen Effect, for the aforementioned reasons. Nevertheless, the analysis conducted provides a useful insight on the external parameters to employ to be able to generate a temperature difference large enough to be above the resolution of the experimental setup. In the Appendix, a preliminary experiment focusing on EE with an in-plane magnetic field setup will be discussed. Analysing the results, and the expected amplitude of the effect for this configuration, it has been assessed how the most fruitful strategy to increase the signal is to apply a stronger out-of-plane field, to saturate the sample in this direction. The employment of U-shaped structures, as detailed in the Appendix, could be important as well, to enhance thermal contrast by generating temperature differences along different directions.

Observing the Ettingshausen Effect would fulfill a double objective, which is confirming the effect in Co_2MnGa, and proving it can be observed via SThM. Both goals have not been reported in literature up to date. From there, one could then probe different materials and tailor their topology to boost the heat-to-charge conversion. This would pave the way to the realization of a cryogenic solid state refrigerator.

Bibliography

[1] Zheng Zhu, Tomoya Higo, et al. Magnetic and transport properties of amorphous, B2 and L21 Co_2MnGa thin films. AIP Advances, 10, 2020.

[2] K. Özdoğan, E. Şaşıoğlu, B. Aktaş, and I. Galanakis. Doping and disorder in the Co_2MnAl and Co_2MnGa half-metallic Heusler alloys. Phys. Rev. B, 74, 2006.

[3] K. Sumida, Y. Sayuraba, et al. Spin-polarized Weyl cones and giant anomalous Nernst effect in ferromagnetic Heusler films. Communication Materials, 1, 2020.

[4] Peter Swekis, Aleksandr S. Sukhanov, et al. Magnetic and electronic properties of Weyl Semimetal Co_2MnGa thin films. Nanomaterials, 11, 2021.

[5] Helena Reichlova, Richard Schlitz, et al. Large anomalous Nernst effect in thin films of the Weyl semimetal Co_2MnGa. Applied Physics Letters, 113, 2018.

[6] T. Seki, R. Iguchi, et al. Visualization of anomalous Ettingshausen effect in a ferromagnetic film: Direct evidence of different symmetry from spin Peltier effect. Applied Physics Letters, 112, 2018.

[7] Junfeng Hu, Yao Zhang, et al. Anomalous Nernst effect in Co_2MnGa thin films with perpendicular magnetic anisotropy. Journal of Magnetism and Magnetic Materials, 500, 2020.

[8] Satya N. Guin, Kaustuv Manna, et al. Anomalous Nernst effect beyond the magnetization scaling relation in the ferromagnetic Heusler compound Co_2MnGa. NPG Asia Materials, 11, 2019.

[9] M. Z. Hasan and C. L. Kane. Colloquium: Topological insulators. Rev. Mod. Phys., 82, 2010.

[10] Arnab Kumar Pariari. Atoms to topological electronic materials: a bedtime story for beginners. Indian Journal of Physics, 95, 2021.

[11] Binghai Yan and Claudia Felser. Topological materials: Weyl semimetals. Annual Review of Condensed Matter Physics, 8, 2017.

[12] Stephen Blundell. Magnetism in Condensed Matter. In Oxford University Press. Oxford, 2001.

[13] Lamberto Duò. Lecture notes for the course "Struttura della Materia" at Politecnico di Milano for Bachelor students of Engineering Physics, 2020.

[14] Giorgio Bertotti. Magnetic Hysteresis. In Academic Press, Electromagnetism. San Diego, 1998.

[15] B. V. Paranjape and J. S. Levinger. Theory of the Ettingshausen Effect in Semiconductors. Phys. Rev., 120, 1960.

[16] Amirkoushyar Ziabari, Mona Zebarjadi, Daryoosh Vashaee, and Ali Shakouri. Nanoscale solid-state cooling: a review. Reports on Progress in Physics, 79, 2016.

[17] Bernard Nysten. Lecture notes for the course Surface Analysis at UCLouvain, 2022.

[18] Wikipedia page, Lennard-Jones potential. Accessed: 11-04-2023.

[19] Park Systems website, Scanning Thermal Microscopy. Accessed: 14-04-2023.

[20] Yun Zhang, Wenkai Zhu, et al. A Review on Principles and Applications of Scanning Thermal Microscopy (SThM). Advanced Functional Materials, 30, 2020.

[21] Yao Zhang, Yuefeng Yin, et al. Berry curvature origin of the thickness-dependent anomalous Hall effect in a ferromagnetic Weyl semimetal. npj Quantum Materials, 6, 2021.

[22] M. Löhndorf, A. Wadas, et al. Structure of cross-tie wall in thin Co films resolved by magnetic force microscopy. Applied Physics Letters, 68, 06 1996.

[23] Sakai Akito, Yo Pierre Mizuta, et al. Giant anomalous Nernst effect and quantum-critical scaling in a ferromagnetic semimetal. Nature Physics, 14, 2018.

[24] E. Şaşıoğlu, L. M. Sandratskii, and P. Bruno. Role of conduction electrons in mediating exchange interactions in Mn-based Heusler alloys. Phys. Rev. B, 77, 2008.

[25] G. J. Li, E. K. Liu, et al. Structure, magnetism, and magnetic compensation behavior of $Co_{50-x}Mn_{25}Ga_{25+x}$ and $Co_{50-x}Mn_{25+x}Ga_{25}$ Heusler alloys. Journal of Applied Physics, 113, 2013.

[26] Junfeng Hu, Yao Zhang, et al. Large Anomalous Nernst angle in Co_2MnGa thin film. IEEE Magnetics Letters, 13, 2022.

[27] L. Leiva, S. Granville, et al. Efficient room-temperature magnetization direction detection by means of the enhanced anomalous Nernst effect in a Weyl ferromagnet. Phys. Rev. Mater., 6, 2022.

[28] L. Leiva, S. Granville, et al. Giant spin Hall angle in the Heusler alloy Weyl ferromagnet co_2MnGa. Phys. Rev. B, 103, 2021.

[29] Michael Victor Berry. Quantal phase factors accompanying adiabatic changes. Proceedings of the Royal Society of London. A. Mathematical and Physical Sciences, 392, 1984.

[30] D. J. Thouless, M. Kohmoto, M. P. Nightingale, and M. den Nijs. Quantized Hall conductance in a two-dimensional periodic potential. Phys. Rev. Lett., 49, 1982.

[31] Di Xiao, Yugui Yao, Zhong Fang, and Qian Niu. Berry-Phase effect in anomalous thermoelectric transport. Phys. Rev. Lett., 97, 2006.

[32] Alex Hubert and Rudolf Schafer. Magnetic Domains. In Springer Berlin. Berlin, 1998.

[33] A. Sommerfeld and N. H. Frank. The Statistical theory of thermoelectric, galvano- and thermomagnetic phenomena in metals. Rev. Mod. Phys., 3, 1931.

[34] Asuka Miura, Hossein Sepehri-Amin, et al. Observation of anomalous Ettingshausen effect and large transverse thermoelectric conductivity in permanent magnets. Applied Physics Letters, 115, 2019.

[35] K. Scholz, P. Jandl, et al. Infinite stage Ettingshausen cooling in Bi-Sb alloys. Journal of Applied Physics, 75, 1994.

[36] Park Systems website, Lateral Force Microscopy. Accessed: 10-04-2023.

[37] Daniel J. Müller, Andra C. Dumitru, et al. Atomic Force Microscopy-based Force Spectroscopy and Multiparametric Imaging of Biomolecular and Cellular Systems. Chemical Reviews, 121, 2021.

[38] Romel D. Gomez, Edward R. Burke, and Isaak D. Mayergoyz. Magnetic imaging in the presence of external fields: Technique and applications (invited). Journal of Applied Physics, 79, 1996.

[39] Grzegorz Wielgoszewski, Przemysław Sulecki, et al. A high-resolution measurement system for novel Scanning Thermal Microscopy resistive nanoprobes. Measurement Science and Technology, 22, 08 2011.

[40] G. Wielgoszewski, P. Sulecki, et al. Microfabricated resistive high-sensitivity nanoprobe for scanning thermal microscopy. Journal of Vacuum Science & Technology B, 28, 2010.

[41] Li Shi and Arunava Majumdar. Thermal Transport Mechanisms at Nanoscale Point Contacts. Journal of Heat Transfer, 124, 07 2001.

[42] K. Luo, Z. Shi, J. Lai, and A. Majumdar. Nanofabrication of sensors on cantilever probe tips for scanning multiprobe microscopy. Applied Physics Letters, 68, 1996.

[43] K.L. Nguyen, O. Merchiers, and P.-O. Chapuis. Near-field radiative heat transfer in scanning thermal microscopy computed with the boundary element method. Journal of Quantitative Spectroscopy and Radiative Transfer, 202, 2017.

[44] Magnetic force microscopy contrast formation and field sensitivity. Journal of Magnetism and Magnetic Materials, 551:169073, 2022.

[45] Budget Sensors website, Magnetic Multi75-G probes. Accessed: 16-04-23.

[46] Achim Harzheim, Charalambos Evangeli, et al. Direct mapping of local Seebeck coefficient in 2D material nanostructures via scanning thermal gate microscopy. 2D Materials, 7, aug 2020.

[47] Ken-Ichi Uchida, Shunsuke Daimon, et al. Observation of anisotropic magneto-Peltier effect in nickel. Nature, 558, 2018.

[48] F. Menges, P. Mensch, et al. Temperature mapping of operating nanoscale devices by scanning probe thermometry. Nature Communications, 7, 2016.

[49] Kaustav Banerjee, Guanghua Wu, et al. Investigation of self-heating phenomenon in small geometry vias using scanning Joule expansion microscopy. Annual Proceedings - Reliability Physics (Symposium). IEEE, January 1999.

[50] Bruker website, VITA DM-GLA1 probes. Accessed: 20-04-23.

[51] Ren Nagasawa, Koichi Oyanagi, et al. Anomalous Ettingshausen effect in iron–carbon alloys. Applied Physics Letters, 121, aug 2022.

[52] T. Seki, R. Iguchi, et al. Visualization of anomalous Ettingshausen effect in a ferromagnetic film: Direct evidence of different symmetry from spin Peltier effect. Applied Physics Letters, 112, 04 2018.

[53] Alex Hubert and Rudolf Schafer. Magnetic Domains. In Springer Link. Berlin, 2014.

[54] Prasanna Shah and A. Gavrin. Effect of varying sputtering parameters on the observation of magnetic domains using high-resolution Bitter microscopy technique. Journal of Applied Physics, 99, 04 2006.

[55] Himalay Basumatary, J. Arout Chelvane, et al. Effect of sputtering parameters on the structure, microstructure and magnetic properties of Tb-Fe films. Thin Solid Films, 583, 2015.

[56] Achim Harzheim, Jean Spiece, et al. Geometrically Enhanced Thermoelectric Effects in Graphene Nanoconstrictions. Nano Letters, 18, 2018.

[57] Nanoworld website, MFMR probes. Accessed: 01-05-2023.

[58] NT-MDT website, MFM-High Coercitivity probes. Accessed: 01-05-2023.

[59] P. W. Bridgman. The Connections between the Four Transverse Galvanomagnetic and Thermomagnetic Phenomena. Phys. Rev., 24, Dec 1924.

[60] Oxford Instruments website, KNT-SThM probes. Accessed: 02-05-23.

[61] Kelvin Nanotechnology website, KNT-SThM-2an probes. Accessed: 02-05-23.

Acknowledgments

This year at Gehring Lab has been a rollercoaster: I doubted myself and my capacities many times, on the other hand in many occasions I made myself aware of all the improvements I made, and of the appreciations received. I started in September when I had never stepped foot in an experimental lab, and now I finish this experience, conscious of the knowledge and skills acquired, and of the path to follow. I know I'm ready for this.

For all of this, I would like to thank firstly Pascal Gehring, my supervisor, who guided me not only in the lab but in particular in the path I will begin after the graduation. Thank you for the opportunity you have given me and for the trust deposited in me. Then, I also have to thank Jean, who followed me every step of the way, being my go-to person for every practical or theoretical doubt I had in this year. The long afternoons in Boltzmann waiting for the scans, separated by many coffee breaks, have been a perfect way to know each other better and have a laugh while complaining about the measurements. Finally I also want to thank Mohammadali, with whom I immediately created a nice friendship, by suggesting him nice places in Brussels and by letting him take charge of the experimental aspects I was not able to do yet.

Finally, I would also like to thank the rest of Gehring Lab: Valentin, Alessandra, Haiyan, Yubin, Jeremie, Lei and Michael. I felt immediately integrated into the group, and this helped me transition into the lab life, and every meeting we had outside of the lab is a nice memory. I wish the best to all of you. I would like to thank my Italian supervisors, Daniela Petti and Edoardo Albisetti, for fruitful discussions which helped me in the interpretation of the data.

Ringraziamenti

Questi tre anni sono stati un lungo percorso che mi ha portato, alla fine, in un luogo completamente diverso da dove avevo cominciato, a Settembre 2020. Quasi tutti i punti di riferimento che avevo accumulato nel corso dei tre anni della triennale sono cambiati, e sono dovuto ripartire praticamente da zero in un Paese nuovo, ed una città nuova. I due anni a LLN sono stati agrodolci: ho conosciuto tante persone, alcune delle quali sono ancora una frequentazione assidua, ma sono presto diventato insofferente del tipo di realtà che si vive lì, e a volte la barriera linguistica ha pesato. D'altro canto, ho affrontato difficoltà nuove e le ho superate, cosa che mi rende certo che, qualunque cosa farò dopo questa laurea, e dovunque finirò, ormai ce la posso fare, e ho tutti gli strumenti che mi servono.

In tutto questo percorso, personale prima che accademico, i miei genitori sono sempre stati al mio fianco, in qualunque situazione. Mi hanno sostenuto nei momenti in cui vedevo tutto nero e volevo mollare, e consigliato nei momenti di incertezza, che, soprattutto negli ultimi tempi, non sono pochi. Senza il vostro sostegno, anche economico, non avrei mai potuto fare questa esperienza, che si sta rivelando decisiva per la mia crescita personale e accademica, e non vi ho mai ringraziato abbastanza per questo. So di fare fatica ad esprimere l'affetto che provo nei vostri confronti, quindi approfitterò di queste righe per provare a ripagare l'affetto che mi avete dato in questi anni e per farvi capire che voi ed il vostro sostegno siete importanti per me, anche se ci sentiamo poco, anche se a volte al telefono sono scocciato, anche se non lo do a vedere. Nei momenti bui per me ci siete stati, anche di persona e nonostante la distanza.

Ora tocca a mio fratello Matteo. Mentirei se dicessi che a volte non mi interrogo sulla natura del nostro rapporto. Penso onestamente che la distanza di questi 6 anni abbia influenzato, unita alla mia (nostra) cronica incapacità di mostrare affetto. Anche qui, non ti ho mai dimostrato quanto ci tengo, quanto la tua presenza sia fondamentale per il mio stare bene, non so manco se ce ne sia bisogno in realtà, perchè sono sicuro che per te sia lo stesso. Nel dubbio te lo dico lo stesso. Probabilmente il futuro ci terrà ancora separati, ma spero con tutto il cuore che, ora che anche tu stai vivendo un'esperienza simile alla mia, riusciamo entrambi a rivestire una parte maggiore nella vita quotidiana dell'altro. By the way, non hai idea quanto sia orgoglioso di vederti così libero ed indipendente da quando sei andato a Roma: sei la mia fonte di ispirazione per la mia vita quotidiana.

Un grande rimpianto di questa scelta di vita di non restare a Salerno è il non aver potuto passare tempo a sufficienza con i miei nonni. Nonna Filly, sei stata un supporto costante in tutti questi anni, e la voglia di inorgoglirti mi ha sempre spinto a dare il massimo: spero di continuare a farlo nel futuro, continuando a ricevere le tue dediche nelle bustine, spesso con qualche citazione in latino. Nonna Laura, sei stata una fonte inesauribile di buon umore telefonico, con le tue storie ed i tuoi aneddoti. Salutarti ogni volta, con la consapevolezza di vederci dopo 3-4 mesi, ed il tentativo di alleggerire il tutto, mi rattrista ogni singola volta. Avrei voluto, con tutto il cuore, esserci di più. Il dispiacere più grande però è che tu, nonno e mio omonimo, non ci sarai a vedermi prendere quel titolo che ti illuminava

gli occhi quando ne parlavi. Pensare che non ci sei più è onestamente ancora un dolore grande, al quale ancora non mi sono abituato. Proverò a rendere onore al fatto di essere la quarta generazione di ingegneri, anche se seguire le tue orme non sarà un percorso facile, visto il tuo successo.

Non posso non ringraziare poi Ceci: ci conosciamo da relativamente poco, ma sai già quanto sei diventata importante per me. Forse infatti sarai l'unica alla quale avrò già detto (o meglio, scritto) ciò che sto per scrivere qui. Sei stata un supporto incredibile per me quest'anno, sia per continuare a spingere con lo studio, con tutte i weekend che abbiamo passato insieme in biblioteca, sia nella vita di tutti i giorni. So di poter contare su di te per qualunque cosa mi capiti, piccola o grande che sia, bella o brutta, e lo sai che tu puoi contare su di me. Averti conosciuta è stata la parte migliore della mia esperienza in Belgio.

Ci sono poi delle persone che, nonostante io continui a cambiare città, università, e Paese addirittura, continuano a essere nel mio quotidiano. Wajuni, sapete che sto parlando di voi: Mimmo, Sandro, Luca, Fabio, Fonzo e Manuel (ci sarebbe anche Matteo, ma di lui abbiamo già parlato). Sostanzialmente è grazie a voi se quando torno a Salerno la sento ancora casa mia, e vedere che, dopo ormai tanto tempo che non ci vediamo più nel quotidiano, il nostro rapporto è ancora così forte, mi tranquillizza molto: siete persone importanti per me e non vi voglio perdere. Menzione speciale per Fabiolone che in più di un'occasione è stato il mio confessore personale, nei momenti in cui avevo bisogno di qualcuno con cui sfogare: grazie Fa, non dimentico.

Sono però orgoglioso di poter dire di aver costruito un'altra famiglia, a Milano questa volta. Il Poli per una volta ha fatto anche una cosa buona, creando dei legami che non si sono sciolti nonostante la distanza. Fratm Trimone, Ale, Dep, Luchè, Gio: per quattro anni siete stati la mia quotidianità, e le mie fugaci sortite a Milano (e, per il trimone, i tuoi lunghi soggiorni a Bruxelles) in questi due anni mi hanno restituito le stesse vibes che abbiamo vissuto in triennale, e che hanno reso la mia esperienza a Milano così speciale. Alla prossima avventura tutti insieme. Le stesse cose però le ripeto anche per Leti, Cerru e Sara (Rossa): il legame che ho stretto con voi è speciale, e conservo il ricordo di polpettoni, costumi di Halloween e Cluedo improvvisati (Rossa), un viaggio a Parigi senza saper parlare francese (Cerru) e di un concerto di Liberato che avevo dato ormai per perso (Leti). Ci aspetta ancora una reunion da fare. Ovviamente in questo quadro non posso non menzionare i miei due ex-coinquilini, Riccardo e Michele: con voi ho vissuto una delle fasi più belle della mia vita, e, se sono così affezionato alla casa di via Gasparotto, è per merito vostro. A Milano ho veramente lasciato *nu piezz' 'e cor*, e non sarebbe potuto essere così se non ci foste stati tutti voi.

Anche a Louvain però ho conosciuto tante e tante persone fantastiche. L'avventura non è andata come me l'aspettavo all'inizio, semplicemente perchè immaginavo un tipo di dinamica diversa, più simile a quella di Milano. Il ricambio semestrale però mi ha permesso di ampliare la mia rete di conoscenze in maniera esponenziale, e conoscere persone da tutto il mondo. Ne menzionerò alcune, senza alcuna pretesa di essere esaustivo. Devo cominciare da Gulli, che è stato il mio coinquilino per tre mesi vivendo nel sottoscala di Harry Potter, e ricordandomi come vivere con un amico arrichisca la tua esperienza. A furia di venire a scroccare pranzi e cene a Bruxelles da te, il nostro rapporto si è consolidato anche quest'anno, dandomi un altro punto di riferimento a Bruxelles. Il tatuaggio dei miei ricordi con te sarà sempre presente, come qualcuno di saggio ha una volta scritto. Con Matteo anche non vedo l'ora di sentire nuove storie di ubriacate ad Amsterdam, così come hai fatto per sei mesi a LLN con una costanza invidiabile. Irene e Pablito anche sono stati una parte importante dei miei primi sei mesi in Belgio, aiutandomi a superare il periodo

più tosto, quando ancora vivevo nella camera ad angolo acuto. Grazie a tutti voi per fantastici ricordi di partite di calcetto, sbronze ad Amsterdam, ed amari da me. Vi auguro il meglio.

Questi ringraziamenti, che poi alla fine non sono ringraziamenti, piuttosto un'occasione per rivivere i momenti importanti di questi 3 (+3) anni, con tutte le persone che mi sono state vicino, non hanno nessuna pretesa di essere esaustivi. Le persone che ho conosciuto e con cui ho interagito sono tante, troppe per essere citate qui, e da ognuna di loro prendi e impari qualcosa, per cercare di evolvere verso la versione migliore di te stesso. Posso solo sperare che i prossimi 6 anni siano altrettanto pieni di esperienze, persone, e cambiamento, come lo sono stati gli scorsi sei. Grazie a tutti per tutto ciò che mi avete dato.

UNIVERSITÉ CATHOLIQUE DE LOUVAIN
École polytechnique de Louvain
Rue Archimède, 1 bte L6.11.01, 1348 Louvain-la-Neuve, Belgique | **www.uclouvain.be/epl**